

On the Contribution of autoionizing states
to XUV radiation-induced double ionization
of nitrous oxide (N_2O)

Dissertation
zur Erlangung des Doktorgrades
der Naturwissenschaften
vorgelegt beim Fachbereich Physik
der Johann Wolfgang Goethe-Universität
in Frankfurt am Main

von
Michael Schönwald
aus Ottweiler

Frankfurt (2015)

(D 30)

vom Fachbereich Physik der
Johann Wolfgang Goethe-Universität als Dissertation angenommen.

Dekan: Prof. Dr. Rene Reifarth

1.Gutachter: Prof. Dr. J. Ullrich

2.Gutachter: Prof. Dr. R. Dörner

Tag der Disputation:

Abstract: “On the Contribution of autoionizing states to XUV radiation-induced double ionization of nitrous oxide (N_2O)”

The implementation of pump-probe experiments with ultrashort laser pulses enables the study of dynamical processes in atoms or molecules, which may provide a deeper insight into their physical origin. The application of this method to systems as nitrous oxide, which is not only a simple example for polyatomic molecules but which also plays a crucial role in the greenhouse effect, promises interesting and beneficial findings.

This thesis presents, on the one hand, the technical extension of an existing experimental setup for high-harmonic generation (HHG) and ultra-fast laser physics by an extreme ultraviolet (XUV) spectrometer for the in-situ observation of the harmonic spectrum during ongoing measurements. The present setup enables the production of short laser pulse trains in the XUV spectral range with durations of a few hundred attoseconds ($1 \text{ as} = 10^{-18} \text{ s}$) via HHG and supports to perform XUV-IR pump-probe experiments using the infrared (IR) driving field with durations of a few femtoseconds. Moreover, a reaction microscope is implemented, which enables the coincident detection of several charged particles emerging from an ionization or dissociation process and to reconstruct their full 3-D-momentum vectors. With this technique it is possible to perform time-resolved momentum spectroscopy of few-particle quantum systems. Here, the design and the calibration of the XUV spectrometer is presented as well as a first application to the analysis of experimental data by providing information on the produced photon energies.

On the other hand, the results of an XUV-pump IR-probe measurement on nitrous oxide (N_2O) are discussed. With the broad harmonic spectrum ($\sim 17 - 45 \text{ eV}$) it is possible to address several states of the singly and doubly ionized cation. One reaction channel is the single ionization into a stable state of N_2O^+ . Here, the coincidentally measured photoelectron energies allow the observation of sidebands, which served to estimate the pulse durations of the involved XUV pulse trains as well as of the fundamental IR pulses. Additionally, single ionization of nitrous oxide can lead to a dissociation into a charged and a neutral fragment. The four respective dissociation channels are compared by presenting their branching ratios, kinetic energy release (KER) distributions and their dependencies on the time delay between pump and probe pulse. In the production of the dication, there are two competitive processes: direct double ionization considering photon energies above the double-ionization threshold, and autoionization of singly ionized and excited molecules in the case of photon energies near the double-ionization threshold. In both cases, the ionization leads to a Coulomb explosion into two charged fragments, where the $N - N$ bond or the $N - O$ bond may dissociate. The influence of the IR-probe field on the ionization yield and the KER was investigated for both dissociation channels and compared. In addition, the corresponding photoelectron energy spectra are presented, which show indications for autoionizing states being involved, and their dependence on the delay and the KER of the respective ions is analyzed.

Zusammenfassung: “Über den Beitrag autoionisierender Zustände zu der von XUV-Strahlung induzierten Doppelionisation von Distickstoffmonoxid (N_2O)“

Die Durchführung von Anregungs- und Abfrage-Experimenten mit ultrakurzen Laserimpulsen ermöglicht die eingehende Untersuchung von dynamischen Prozessen in Atomen oder Molekülen und liefert somit tiefere Einblicke in deren physikalischen Ursprung. Die Anwendung dieser Methode auf Systeme wie Distickstoffmonoxid, welches nicht nur eines der einfachsten Vertreter eines Moleküles mit mehr als zwei Kernen ist, sondern auch eine wichtige Rolle bei dem Treibhauseffekt spielt, verspricht dabei interessante und hilfreiche neue Erkenntnisse.

Die vorliegende Arbeit präsentiert zunächst die Erweiterung eines vorhandenen experimentellen Aufbaus zur Erzeugung von harmonischer Strahlung und der Ultrakurzzeit-Laserphysik durch ein Spektrometer für extrem ultraviolettes Licht (XUV), in welchem das Spektrum der erzeugten XUV Strahlung während einer laufenden Messung aufgenommen werden kann. Der gegenwärtige Aufbau erlaubt die Erzeugung von Impulspulsen mit Halbwertsbreiten von wenigen hundert Attosekunden ($1 \text{ as} = 10^{-18} \text{ s}$) und ermöglicht die Durchführung von XUV-IR Anregungs- und Abfrage-Experimenten, in denen auch die ursprünglichen, infraroten (IR) Laserimpulse verwandt werden, deren Halbwertsbreiten im Bereich weniger Femtosekunden liegen. Darüber hinaus wird ein Reaktionsmikroskop genutzt, welches das koinzidente Detektieren mehrerer geladener Teilchen und das Rekonstruieren der dazugehörigen 3-D Impulsvektoren ermöglicht. Damit lässt sich zeitaufgelöste Impulsspektroskopie an einfachen Quantensystemen durchführen. Die Konzeption des XUV Spektrometers wird erklärt, sowie dessen Kalibrierung und erste Anwendung, bei der die gemessene Photonenenergieverteilung die Analyse der Daten unterstützte.

Darüber hinaus werden die Ergebnisse eines XUV-Anregungs-IR-Abfrage-Experimentes in Distickstoffmonoxid (N_2O) präsentiert. Photonen des harmonischen Spektrums ($\sim 17 - 45 \text{ eV}$) können verschiedene Zustände sowohl des einfach als auch des zweifach geladenen Ions erreichen. Wird das Molekül einfach ionisiert, treten in den, koinzident zu N_2O^+ gemessenen, Photoelektronenergieverteilungen sogenannte Seitenbänder auf, durch welche die Impulsdauern der Attosekundenimpulszüge und der IR Impulse bestimmt werden können. Daneben ist es auch möglich, dass das einfach geladene Ion in ein neutrales und ein geladenes Fragment dissoziiert. Das Erzeugungsverhältnis, sowie die Verteilung der freiwerdenden kinetischen Energie, als auch die Abhängigkeit von dem Zeitunterschied zwischen Anregungs- und Abfrageimpuls der vier möglichen Reaktionskanäle werden untereinander verglichen. Abhängig von der betrachteten Photonenenergie kann das Molekül direkt oder durch Autoionisation eines einfach geladenen, aber angeregten Moleküls doppelt ionisieren. Unabhängig von der Art führt die Doppelionisation zu einer Coulomb-Explosion, bei der entweder die $N - N$ Bindung oder die $N - O$ Bindung dissoziiert, so dass zwei geladene Fragmente entstehen. Der Einfluss des Abfrage-Impulses auf beide Kanäle wird untersucht und miteinander verglichen. Zusätzlich werden die zugehörigen Photoelektronenergieverteilungen gezeigt, die Anzeichen für die Involvierung autoionisierender Zustände aufweisen und welche wiederum eine Abhängigkeit vom Zeitabstand zwischen beiden Impulsen und von der kinetischen Energie der erzeugten Ionen zeigen.

Contents

I	Introduction	1
II	Fundamentals	5
1	Ultrashort Laser Pulses	6
1.1	Generation via Mode Locking	6
1.2	Propagation Effects	12
2	Atoms in IR Laser Fields	17
2.1	Multi-Photon Ionization	18
2.2	Tunnel Ionization	19
3	High-Harmonic Generation	22
3.1	Three-Step Model	23
3.2	Quantum-Mechanical Model	30
3.3	Phase Matching	31
3.4	Attosecond Pulse Trains	36
3.5	Sidebands	37
4	Molecules	40
4.1	General Description	40
4.2	Molecules in XUV Light Fields	43
4.3	XUV-IR Pump-Probe Experiments	46
III	Experimental Setup	49
5	The Laser System	50
5.1	The Titanium:Sapphire Laser	50
5.2	Pulse Compression	52
6	The HHG Setup & Beamline	54
6.1	The Vacuum System	54
6.2	Beamline	58

6.3	Characterization of the High Harmonics	61
7	Reaction Microscope	65
7.1	Design	65
7.2	Calculation of Momenta	72
7.3	Acceptance	78
7.4	Resolution	80
IV	The XUV Spectrometer	83
8	Design of an XUV Spectrometer	84
8.1	Overview	84
8.2	Spectrometer	86
8.3	Detection System	88
8.4	Subconstruction	89
9	Combining the Spectrometer and the ReMi Technique	90
9.1	Operating the Spectrometer	90
9.2	Combining the Vacua	92
9.3	Experimental Benefits	94
10	Calibration of the Spectrometer	96
10.1	Geometrical Calibration	96
10.2	Improving the Calibration with the ReMi	97
10.3	Outlook	99
V	Experimental Results	101
11	Overview	103
12	Single Ionization of N_2O^+	106
12.1	N_2O^+ in Coincidence with an Electron	106
12.2	Dissociation into a Charged and a Neutral Fragment	108
13	Double Ionization of N_2O	114
13.1	KER	116
13.2	Delay Dependent Effects	117
13.3	Electron Energies	122
VI	Conclusion	133
	Bibliography	139

I Introduction

The temporally resolved study of a dynamical process can provide deep insight into its fundamental mode of operation or its physical origin. A long time before the invention of techniques to study ultrafast processes in atoms or molecules, people were interested in macroscopic dynamics, using photography for the observation. The first attempt was the so-called chronophotography, in which several time-delayed pictures of a motion (such as flying insects or walking humans) were recorded and juxtaposed. One of the most famous examples is a series of pictures of a horse in motion taken by Eadweard Muybridge 1878, which shows a galloping horse and proves that at certain times all feet of the animal are off the ground (see figure 0.1). This technique was extended to motion-pictures and nowadays high-speed cameras, which enable the inspection of fast macroscopic processes and supports e.g. the controlling of industrial productions or the analysis of crash tests. Very recent developments in the high-speed technology lead to optical imaging systems that are able to record up to several trillion frames per second (fps) [1, 2] and thus reaching the picosecond (ps) and even the femtosecond (fs) regime, in which it is possible to trace the propagation of light [1] or of phonons in a crystal [2].



Figure 0.1: Self-made chronophotography of a galloping horse.

Even though these trillion fps cameras reach the temporal regime, in which atomic or molecular processes take place, other methods are required to study dynamics in atoms or molecules, but which are based on similar principles as for example the chronophotography. A state-of-the-art method is to use the so-called pump-probe technique in combination with a reaction microscope (ReMi) [3]. Here, a first laser pulse, the so-called pump pulse,

initializes a dynamical process by excitation or ionization and a second pulse, the probe pulse, inquires the state of the system after a variable time delay¹. Making a sufficient number of “shots” at different delays allows to trace dynamics with a temporal resolution, which is in the order of the duration of the applied pulses. The interesting processes as for example vibration of the nuclei in a molecule or electronic transitions occur on time scales from a few fs down to several hundred attoseconds (as).

To achieve a sufficient temporal resolution, ultra-short laser pulses are required. Nowadays, one possibility is the production of attosecond pulses via high-harmonic generation (HHG) with IR pulses from Titanium:Sapphire (Ti:Sa) laser systems, which were developed in 1986 [4], 36 years after the invention of the first laser by Maiman [5]. These machines paved the way for a reliable and stable HHG. After the second harmonic was already observed in 1961 by Franken et al. [6], McPherson et al. discovered in 1987 the appearance of light with photon energies of odd multiples of the fundamental light [7], while he was studying multiphoton ionization processes in rare gases. Subsequent studies revealed properties of the HHG such as the plateau, in which the harmonics are generated with equal intensity and the cut-off [7, 8]. In the early nineties, this technique was discerned as promising candidate to open the research towards the attosecond time scale [9]. Nowadays, elaborated methods of pulse compression allow the production of single-cycle IR laser pulses, with enabling the production of single attosecond pulses of approximately 80 as duration [10]. Additionally, it could be demonstrated that it is possible to produce broadband XUV pulses with a Fourier limit of 2.5 as [11] and thus reaching the time scale of fast electronic dynamics.

In our laboratory, kinematically complete XUV-pump IR-probe experiments are carried out. As mentioned above, they are performed in a ReMi, which allows the reconstruction of the three-dimensional momenta of all produced charged particles. In addition, it enables the coincident measurement of multiple particles and thus the identification and the separation of several reaction channels.

Most of the previous experiments, which were performed at the presented setup, studied

¹ In contrast to the macroscopic methods mentioned above, in which subsequent pictures of a single object were made, in the “quantum mechanical world” processes are strongly influenced by the observation and, additionally, in the experiment the target particles themselves are used to detect the respective state of the system. However, due to the fact that all quantum mechanical observables are expressed by probability distributions, it is possible to superimpose snap-shots of several systems and consider this as probability distribution of a single one.

simpler systems, such as sideband oscillations in rare gases [12] and wave-packet dynamics, electron localization and autoionization lifetimes of doubly excited states in hydrogen [13–16]. This thesis takes a step towards more complex systems by presenting the results of a measurement on nitrous oxide (N_2O). Its trivial name is laughing gas and it is widely known for its usage in medicine (esp. dentistry) due to its anesthetic and analgetic effects [17] but also for its application as an oxidizer in rocket and car engines [18] and as propellant for foods (e.g. whipped cream). In addition, the molecule is one of the most important anthropogenic greenhouse gases (with an approximately 300 times higher impact on the stratospheric ozone than CO_2) [19]. Atmospheric nitrous oxide can undergo photodissociation. The fragments possibly react with the present ozone (O_3) to two NO molecules or to N_2 and O_2 [20]. Due to its crucial role in the greenhouse effect and the fact, that it is a simple example for a polyatomic molecule (since it is triatomic and has a linear shape), nitrous oxide is an interesting candidate for photon-interaction studies [21] from the UV (e.g. [22]) to the soft-X-ray regime [23]. Additionally, photoionization studies in the VUV and XUV regime are also of interest for planetary science in order to gain a deeper insight into the chemistry of the ionosphere of planets not only for the earth but also for other solar system planets (or planet-like objects) such as Mars, Venus, and Titan [24].

The thesis is structured as follows: In the following chapter II, the fundamental physics will be introduced. It begins with the generation of ultrashort laser pulses and how they are influenced by propagation through a dispersive medium. Then, it will be discussed, how such laser pulses interact with atomic systems and how the photoionization process can be described. The next section investigates the production of high harmonics by introducing the “three-step model” as well as the corresponding quantum mechanical model. Afterwards, a description of macroscopic aspects of HHG, such as phase matching, will be given. Subsequently, the physics of molecules will briefly be touched on, showing the Schrödinger equation in the Born-Oppenheimer approximation and the spectroscopic notation of the molecular states. Finally, it will be discussed, how molecules are influenced by XUV light fields with special attention to the Franck-Condon principle and a short introduction into the pump-probe technique.

Chapter III concentrates on the experimental setup, used to carry out the presented experiments. First, the laser system will be shown as well as methods to compress the pulses of the commercially available Ti:Sa laser down to approximately 10 fs. Subsequently, the beamline preparing the laser for and guiding it into the experiment will be presented.

This covers also the setup used for HHG and the IR beamline including the delay stage. At the end of this chapter, the ReMi technique will be introduced by showing the design of our ReMi. Additionally, its working principle and the reconstruction of the three-dimensional momenta from the measured data will be introduced. Finally, the acceptance and resolution of the reconstructed momenta will be discussed.

As essential part of this work, an XUV-photon spectrometer was designed and constructed. In chapter IV first the design will be presented by giving an overview over the whole setup of the device and explaining details concerning the actual spectrometer and the light-detection unit. Afterwards, it will be shown, how the spectrometer is connected to the ReMi, such that it is possible to measure the spectrum of the XUV light simultaneously to an ongoing experiment, and which additional information we gain by the combination of ReMi and spectrometer. To complete this section, it will be discussed how the measured spectra are calibrated using both, the geometry of the spectrometer as well as supporting data from a ReMi measurement.

The XUV-pump IR-probe measurement in nitrous oxide (N_2O) will be presented in chapter V. Here, we study photo-, autoionization, and dissociation of the triatomic molecule. First, a conspectus of the measurement will be given by introducing some experimental settings and properties of the investigated N_2O followed by an overview of the detected fragments of the target molecule, identifying several dissociation channels. Then, the single ionization of nitrous oxide is analyzed, showing the two possible channels: ionization into a stable state of N_2O^+ , or its dissociation into a charged and a neutral fragment. Subsequently, the double ionization channel of the molecule identified by the coincident detection of pairs of charged fragments will be shown. Here, two dissociation channels can be differentiated: the dissociation into N^+ and NO^+ , and into N_2^+ and O^+ . The influence of the IR-pump pulse onto these channels is investigated, showing that both are affected differently. To complete the picture of the double ionization process, the respective photoelectron energies are presented as function of the time delay between pump and probe pulse, as well as of the kinetic energy release (KER) of the particular ions.

Finally, chapter VI summarizes the results of this work and gives a brief outlook.

II Fundamentals

The part “Fundamentals” will introduce into the fundamental physics needed to understand the main part of this work. The experiments performed here are concerned with laser-induced dynamics in atoms or small molecules. In order to carry out XUV-pump IR-probe experiments, we are using ultrashort laser pulses. These are produced by a Titanium:Sapphire (Ti:Sa) laser with a duration of approximately 30 femtoseconds (fs). In order to improve the temporal resolution in the experiments, the pulses have to be compressed to a few femtoseconds. Therefore, the spectrum of the fundamental IR pulses is broadened via self-phase modulation (SPM) in a hollow-core fiber and re-compressed in a chirped-mirror compressor, which counterbalances the dispersion the pulses have collected within the SPM-hollow fiber as well as by propagating through dispersive media, such as air and glass. Afterwards, the pulses are used on the one hand to generate high harmonics for the production of the XUV-pump pulses and on the other hand as IR-probe pulses directly. In the following, the basic, physical principles of these effects will be introduced, whereas chapter III will explain the technical realization.

At first, the properties of ultrashort pulses will be discussed. How they are generated and how they are influenced by propagating through dispersive media. Then the process of HHG will be presented. Starting with a theoretical description at a single atom level we will proceed to consider macroscopic effects on this process. Finally, a brief introduction into the theoretical description of small polyatomic molecules will be given, as well as into the properties of electronic transitions.

1 Ultrashort Laser Pulses

The goal of our research is to temporally resolve photochemical processes. The so-called pump-probe experiments open the possibility to measure such dynamics. In this technique, the first incoming pump-pulse initiates a dynamical reaction in the target, as for example an excitation of a vibronic or dissociative state, which is then inquired by the probe-pulse. The pulse lengths of both pulses determine the temporal resolution of the experiment. Since the dynamics to be explored are fast, it is important to achieve pulses with a duration of only a few femtoseconds.

1.1 Generation via Mode Locking

Already one year after the invention of the laser by Maiman in 1960 [5], the first q-switched laser was realized [25]. This technique enabled pulse durations of about 10 ns. In the mid-sixties the principle of mode locking was discovered [26]. Today, modern Ti:Sa laser systems using this technique achieve pulse durations of a few tens of femtoseconds [27]. It is based on fixing the relation between the phases of many emitting longitudinal modes in the laser cavity and leads to a significant increase of the peak power in the sum over all modes. This can be done actively, which is called “active mode locking” or passively (“passive mode locking”). The Ti:Sa laser systems are mainly based on passive Kerr-lens mode locking, which will be discussed later on.

Considering a laser cavity of length L , standing waves are formed, whereas their frequency ω_C is connected to the cavity length according to

$$L = n \frac{\lambda_C}{2} = n \frac{\pi c}{\omega_C} \quad (1.1)$$

where c is the speed of light, λ_C the wavelength of the n^{th} mode and n represents an integer. These standing waves are called longitudinal modes. There is a fixed frequency spacing of $\Delta\omega_C = \frac{\pi c}{L}$ between the individual modes. Apart from that, the amplitudes and phases are fluctuating statistically. To gain ultrashort pulses it is necessary to introduce a fixed intensity distribution in the frequency domain as well as a phase relation. This will lead to a pulse train in the time domain. Then the total electric field can be written as a coherent sum over all longitudinal modes, which can be described as plane standing waves [28]

$$E(t) = \sum_{q=-n}^n E_0 \exp(i[(\omega_0 + q\Delta\omega)]t + q\varphi), \quad (1.2)$$

where E_0 is the amplitude of the electric field, ω_0 is the central wave length, and φ is the constant phase difference between 2 modes $\varphi_{q+1} - \varphi_q = \varphi$ and the phase of the central mode is defined as 0. Now, one can solve this sum analytically (1.2) and obtains

$$E(t) = A(t) \exp(i\omega_0 t) \quad (1.3)$$

with

$$A(t) = E_0 \frac{\sin((2n+1)\frac{\Delta\omega t + \varphi}{2})}{\sin\left(\frac{\Delta\omega t + \varphi}{2}\right)}. \quad (1.4)$$

The electric field $E(t)$ can be understood as a sine-like carrier wave at the carrier frequency ω_0 and a (slowly varying) time-dependent amplitude $A(t)$. The intensity $I(t)$ is proportional to the squared amplitude $I(t) \propto |A(t)|^2$. Due to the fixed phase relation the modes interfere and build a train of short pulses. The amplitude reaches its maximum when the denominator of equation 1.4 vanishes. This is fulfilled for $\sin((\Delta\omega t + \varphi)/2) = 0$, which is the case when² $(\Delta\omega t + \varphi)/2 = m\pi$. The periodicity of the pulse train is then the inverse time difference τ_P between two maxima. This can be calculated as

$$\frac{1}{2}((\Delta\omega t_1 + \varphi) - (\Delta\omega t_2 + \varphi)) = m\pi - (m+1)\pi \quad (1.5)$$

$$\Leftrightarrow \Delta\omega(t_1 - t_2) = 2\pi \quad (1.6)$$

$$\Leftrightarrow (t_1 - t_2) = \tau_P = \frac{2\pi}{\Delta\omega} = \frac{2L}{c}. \quad (1.7)$$

² In the case $(\Delta\omega t + \varphi)/2 = m\pi$ both, the numerator and the denominator of equation (1.4) approach 0. Nevertheless, it can be shown by L'Hôpital's rule that the limit converges to a finite number. For functions $f(x)$ and $g(x)$ with $f(x_0) = g(x_0) = 0$ it obtains that $\lim_{x \rightarrow x_0} \frac{f(x)}{g(x)} = \lim_{x \rightarrow x_0} \frac{f'(x)}{g'(x)}$, and accordingly in the present case $\lim_{x \rightarrow m\pi} \frac{\sin((2n+1)x)}{\sin(x)} = \lim_{x \rightarrow m\pi} \frac{(2n+1)\cos(x)}{\cos(x)} = 2n+1$.

The periodicity is equal to the circulation time of the pulse in the laser cavity, which means, there is only a single pulse that oscillates back and forth.

Up to now, mode locking was only presented in the time domain and in a very ideal case by assuming some simplifications, the most important ones being the constant phase of the central mode and that the amplitudes of the different modes are equal. For more general calculations, an analogue description by switching to the frequency domain via Fourier transform can be used. In this case a wave propagating along the z -direction is described by [29]

$$E(z,t) = \frac{1}{2\pi} \int_{-\infty}^{\infty} d\omega \cdot \tilde{E}(z,\omega) \cdot \exp(i\omega t) \quad (1.8)$$

$$\tilde{E}(z,\omega) = \frac{1}{2\pi} \int_{-\infty}^{\infty} dt \cdot E(z,t) \cdot \exp(-i\omega t). \quad (1.9)$$

Furthermore, one can split $\tilde{E}(z,\omega)$ into a spectral amplitude $a(\omega)$ and a spectral phase $\varphi(z,\omega)$:

$$\tilde{E}(z,\omega) = a(\omega) \cdot \exp(i\varphi(z,\omega)). \quad (1.10)$$

To illustrate mode locking, in figure 1.1 a calculated laser-pulse train consisting of 15 locked longitudinal modes is shown in the frequency and time domain as well as the resulting intensity distribution. The perfect mode locking of these few modes leads to pulses with a duration of several femtoseconds. In a real laser cavity a number of $\sim 10^6$ modes are locked (but not as perfectly as in the calculation). As it will be shown later, the minimal achievable pulse duration is determined by the spectral width of the longitudinal modes, but with a given spectrum the pulse length depends on the number of coupled modes.

1.1.1 Pulses with Gaussian Envelopes

The amplitude function $A(t)$ and the spectral amplitude $a(\omega)$ are often described by Gaussian functions. They have the advantage to fit well the reality and, at the same time,

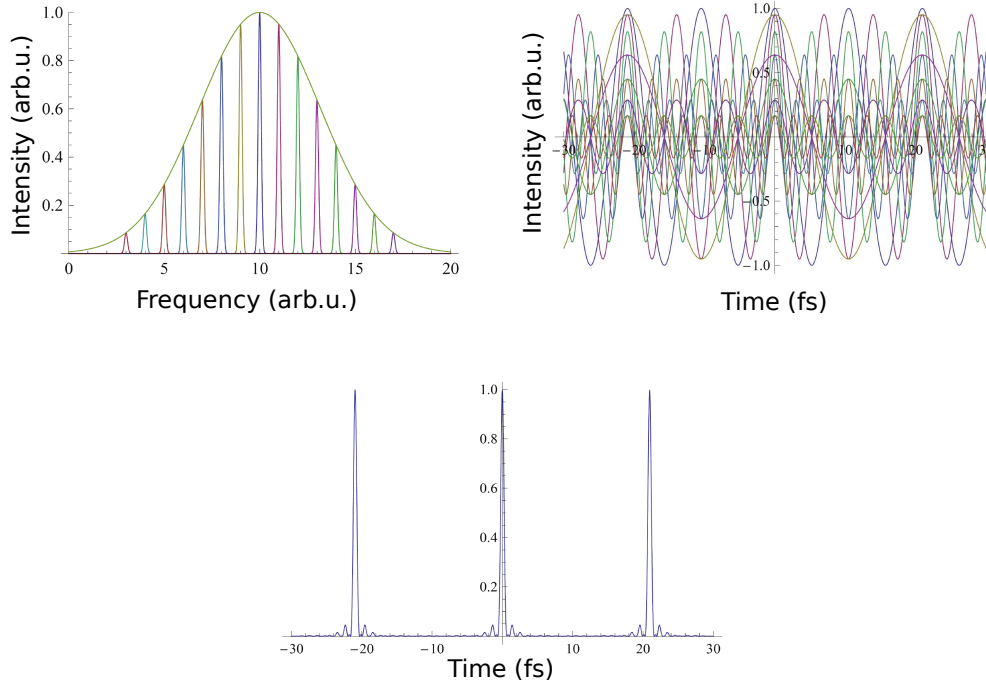


Figure 1.1: From [30]. Above, on the left side, a pulse train consisting of 15 longitudinal modes is shown in the frequency domain. Their individual weights are given by the spectral gain profile of the gain medium, approximated by a Gaussian curve. Above, on the right side, every single mode is plotted in the time domain and they are already phase locked with each other. As one can see, there are 3 points in time, where the 15 modes have a common maximum and in the lower plot the intensity distribution of the interfering modes is shown. The more modes participate in this process the shorter the pulses are.

they can be treated analytically to a certain degree in calculations [31]. In addition, the shape of a Gaussian function is not influenced by Fourier transformation.

Using Gaussian functions for the amplitude function $A(t)$ and the spectral amplitude $a(\omega)$, equations (1.3) and (1.10) transform to

$$E(t) = A_0 e^{-2\ln 2 \left(\frac{t}{\tau}\right)^2} e^{i(\omega_0 t)} \quad (1.11)$$

and

$$\tilde{E}(z, \omega) = a_0 e^{-2 \ln 2 \frac{(\omega - \omega_0)^2}{(\Delta \omega)^2}} e^{i\varphi(z, \omega)}, \quad (1.12)$$

with A_0 and a_0 as the peaks of the respective amplitude, $\Delta \omega$ is the spectral width and τ the pulse duration. Both, the pulse duration and the spectral width are given as full width at half maximum (FWHM) values. An interesting measure for the strength of a laser pulse is the peak power P_0 , respectively the peak intensity I_0 , since many interesting (non-linear) processes show a strong intensity dependence. The two quantities are defined as

$$P_0 = \frac{\varepsilon}{\int_{-\infty}^{+\infty} \exp(-4 \ln 2 (\frac{t}{\tau})^2) dt} \quad (1.13)$$

$$\Rightarrow I_0 = \frac{2P_0}{\pi w^2} = 4 \sqrt{\frac{\ln 2}{\pi^3}} \frac{\varepsilon}{w^2 \tau}, \quad (1.14)$$

with the pulse energy ε and w the beam waist. Here, it can be seen that the peak power and intensity is increasing, if either the pulse energy is increased or if the pulse duration shortens. In the lab, the single pulse energy is not easily accessible. What is measured instead is the averaged power P_{av} , which connects the pulse energy ε and the repetition rate f_{rep}

$$P_{av} = f_{rep} \cdot \varepsilon. \quad (1.15)$$

A final important characteristic of laser pulses is the time-bandwidth product. It gives, analogously to the Heisenberg uncertainty principle, a lower limit for the pulse duration τ for light with a certain spectral width $\Delta \omega$. For Gaussian pulses it is given by

$$\tau \cdot \Delta \omega = \frac{2 \ln 2}{\pi}. \quad (1.16)$$

Pulses that fulfill this condition are called Fourier limited.

1.1.2 Kerr-Lens Mode-Locking

In the previous section 1.1 the mechanism of mode locking was explained. Kerr-lens mode-locking is one of the most effective methods to provide ultrashort pulses, at which a

so-called Kerr-medium is inserted into the laser cavity.

The Kerr effect is based on the intensity dependence of the refractive index n of certain media [32]:

$$n = n_0 + n_2 I(t), \quad (1.17)$$

where n_0 is the linear and n_2 the non-linear coefficient of the refractive index and $I(t)$ the intensity of the light propagating through the media. Regarding a Gaussian laser beam, its intensity decreases from the center to the edges. It propagates through the Kerr-medium, which has a positive n_2 value. Therefore, the refractive index in the center of the beam is lower than at the edges, which leads to a self-focusing. The laser has to be adjusted in a way that the cavity losses are reduced when the beam is focused. In this case, higher intensities and, thus, the pulsed mode of the laser are preferentially amplified. Technically, it can be realized by inserting an aperture behind the Kerr-medium, thus the unfocused beam is partially blocked, whereas the self-focused beam passes entirely (see figure 1.2) [33, 34]. In addition, the Kerr-medium is a saturable absorber, that shows decreasing absorption with increasing intensity of the light interacting with it. As a result, higher intensities will experience a higher gain, which also leads to an affinity of the laser to operate in a pulsed mode with higher single-shot intensities and not in a cw-mode. This effect was discovered by W. Sibbet and O. Spence [35] in a Ti:Sa laser. There, the Ti:Sa crystal itself acts as Kerr-medium. This is the reason, why the Ti:Sa laser simplified the production of ultrashort laser pulses and found its way into many applications.

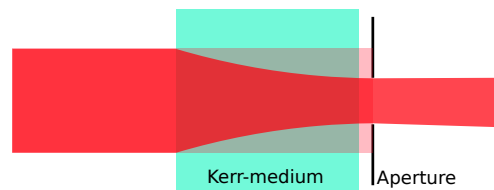


Figure 1.2: Illustration of the self-focusing of a laser beam in a Kerr-medium.

1.2 Propagation Effects

1.2.1 Dispersion

Dispersion depicts a wavelength λ or frequency ω dependent effect on waves propagating in a medium. For electro-magnetical waves the phase velocity v_{ph} differs from the speed of light in vacuum dependent on the frequency dependent refractive index $n(\omega)$ of the medium [28]

$$v_{ph}(\omega) = \frac{c}{n(\omega)}. \quad (1.18)$$

With $v_{ph} = \lambda\nu = \frac{\omega}{k(\omega)}$ dispersion can also be described by a frequency ($\nu = \frac{2\pi}{\omega}$) dependent wave number

$$k(\omega) = n(\omega)\frac{\omega}{c}. \quad (1.19)$$

Here, the optical spectrum is conserved, while the spectral phase of the pulse changes. As seen before in (1.8) the temporal- and spatial structure of the laser pulse writes as

$$E(z,t) = \frac{1}{2\pi} \int_{-\infty}^{\infty} d\omega \cdot \tilde{E}(z,\omega) \cdot \exp(i\omega t) \quad (1.20)$$

$$= \frac{1}{2\pi} \int_{-\infty}^{\infty} d\omega \cdot \tilde{E}(0,\omega) \cdot \exp(i\phi(z,\omega)) \cdot \exp(i\omega t), \quad (1.21)$$

where $\phi(z,\omega)$ is the spatio-spectral phase of the laser pulse. This phase describes the dispersive properties of matter. It is useful to look at the Taylor series of the total phase expanded around the central wavelength ω_0 [31, 36]

$$\phi(z,\omega) = \phi(0,\omega) + k(\omega)z \quad (1.22)$$

$$= \phi(\omega_0) + \underbrace{\frac{\partial\phi}{\partial\omega}|_{\omega_0}}_{GD}(\omega - \omega_0) + \frac{1}{2} \underbrace{\frac{\partial^2\phi}{\partial^2\omega}|_{\omega_0}}_{GDD}(\omega - \omega_0)^2 + \frac{1}{6} \underbrace{\frac{\partial^3\phi}{\partial^3\omega}|_{\omega_0}}_{TOD}(\omega - \omega_0)^3, \quad (1.23)$$

with

$$k(\omega) = k_{vac}n(\omega) = \frac{\omega}{c}n(\omega), \quad (1.24)$$

where k_{vac} is the wave vector in vacuum, $n(\omega)$ is the frequency-dependent refractive index and c is the velocity of light.

GD or group delay is a dispersion effect of the first order. It leads to a delay of the entire pulse without effecting the pulse shape.

GDD or group delay dispersion is a second order effect. It describes the frequency dependence of the group delay, at which different frequencies have a different delay. This results in a linear chirp of the pulse with frequencies increasing linearly in time from red to blue or vice versa, depending on the sign of GDD.

TOD or third-order dispersion. It is also based on the frequency dependence of the group delay dispersion. It leads to higher-order (nonlinear) chirps.

As can be seen from equation (1.23), the role of higher dispersion parameters rises with growing bandwidth. To generate pulses lasting only a few optical cycles, for which a bandwidth of an octave or more is needed, it is therefore required to counterbalance the collected (positive) dispersion, the laser beam accumulates while propagating through glass and through gases (such as air) in the cavity and behind.

1.2.2 Dispersion Compensation

The presented dispersion effects influence especially the pulse length by introducing a chirp, which is defined as a temporal frequency variation of the carrier wave. To achieve the shortest pulse possible, it is necessary to create negative dispersion to compensate the positive chirp in glass and gases. One of the easiest ways to create negative chirp is to spectrally disperse the light and let the different spectral components propagate different optical path lengths. The spectral dispersion can be realized by prisms [37, 38] or gratings [39]. The working principle of a grating compressor is shown in figure 1.3(a). A more profound and mathematical description can be found in [36].

Another method to introduce negative dispersion is the usage of so-called chirped mirrors. These mirrors consist of a stack of several semi-reflective layers of different materials. The distribution of the layers is chosen in a way that for short wavelengths Bragg's law is

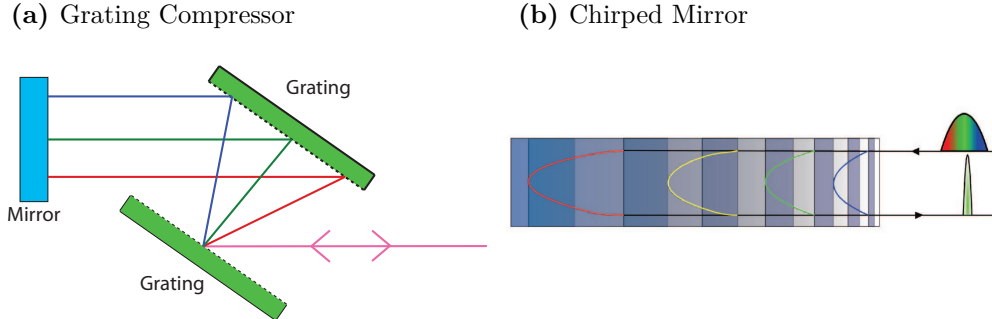


Figure 1.3: (a) Working principle of a grating compressor. The first grating spectrally disperses the incoming light, the second one collimates the spectral components. The light is back-reflected by a mirror via both gratings so that it is superimposed again. Due to the geometry, different spectral components cover different path lengths in order to compensate the chirp. (b) From [29]. Cross-section through a chirped mirror. Depending on the local layer spacing, light of a specific wavelength is reflected at a specific depth within the material, here introducing longer optical paths for red light vs. blue light in order to reverse the effect of normal dispersion.

fulfilled in the upper layers and for longer wavelengths in the lower ones (see figure 1.3(b)). The perfect layer distribution is optimized by specific computer algorithms to compensate for any kind of high-order dispersion [40].

1.2.3 Self-Phase Modulation

The amplification process in Ti:Sa lasers has a restricted gain bandwidth and shows various effects as gain narrowing. In addition, broadband, bandwidth-limited pulses easily reach a critical peak power, which would damage the Ti:Sa crystal. Therefore, usually chirped pulses with a narrowed spectrum are amplified, such that pulses not shorter than a few tens of femtoseconds are typically produced in such laser amplifiers. However, for the temporal resolution in the experiment, shorter pulse durations of a few femtoseconds are required. Therefore, we are using the effect of self-phase modulation (SPM) to broaden the spectrum of the laser pulses and gain shorter pulses.

SPM is a non-linear optical effect. Its origin lies in the induced intensity-dependent refractive index change of the medium. This change causes a phase modification on the incoming pulsed wave induced by its own temporal intensity profile $I(t)$, which is assumed to have a Gaussian shape [29]

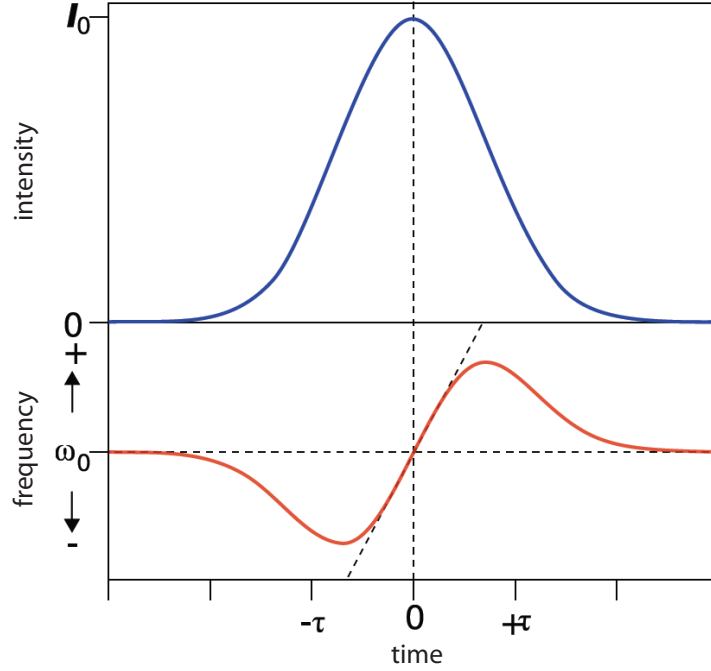


Figure 1.4: From [29]. It is illustrated in blue what the fundamental pulse envelope looks like and in red is shown the instantaneous frequency.

$$I(t) = I_0 e^{-\frac{t^2}{\Delta\tau^2}}. \quad (1.25)$$

The time- and intensity-dependent refractive index was already introduced in equation (1.17). It is divided in a constant part n_0 , which corresponds to the linear refractive index, and an intensity dependent part $n_2 I(t)$, which is coupled to the optical susceptibility:

$$n(t) = n_0 + n_2 I(t). \quad (1.26)$$

A Gaussian pulse, which propagates through a medium, gains an additional, non-linear phase. The temporal phase $\varphi(t)$ after a propagation length L is given by

$$\varphi(t) = \frac{\omega_0}{c} n(t) L. \quad (1.27)$$

This time-dependent nonlinear phase leads to a shift of the frequency $\Delta\omega(t)$, which is defined by

$$\Delta\omega(t) = -\frac{d\varphi(t)}{dt} \quad (1.28)$$

$$= -\frac{\omega_0}{c} L \frac{dn(t)}{dt} \quad (1.29)$$

$$= \frac{2\omega_0 L n_2 t}{c \Delta\tau^2} I_0 e^{-\frac{t^2}{\Delta\tau^2}} \quad (1.30)$$

with

$$\frac{dn(t)}{dt} = n_2 \frac{dI(t)}{dt} = -2n_2 \frac{t}{\Delta\tau^2} I_0 e^{-\frac{t^2}{\Delta\tau^2}}. \quad (1.31)$$

From equation (1.30) it is obvious that the broadening is due to the in- and decreasing intensity, since $\Delta\omega \propto I(t)$. Figure 1.4 shows the intensity envelope of a laser pulse (blue), whereas the red curves illustrates $\Delta\omega$; while the leading edge is red-shifted, the trailing edge is blue-shifted. The pulse shape is not influenced by SPM. Furthermore, equation (1.30) reveals that the strength of the spectral broadening is coupled to the original pulse length ($\Delta\omega \propto \frac{1}{\tau^2}$) [41].

Experimentally, the laser is focused into a thin, long hollow fiber ($\sim 250 \mu\text{m}$ and 1 m long) filled with a gas (in our setup it is typically filled with 3.5 bar of neon). The details of the laser and the pulse compression scheme used in the present work are given in chapter 5.

2 Atoms in IR Laser Fields

In the experiments presented in this work, IR laser pulses are used directly as probe pulse as well as to create attosecond pulse trains (APT) via high-harmonic generation (HHG) with photon energies in the extreme ultraviolet (XUV) regime acting as a pump pulse. In both cases, the IR pulses are focused to peak intensities in the order of 10^{11} to 10^{15} W/cm² corresponding to electric field strengths of about 10^5 to 10^9 V/cm, thus approaching the regime of one atomic unit (a.u.) e.g. $E_{a.u.} = 5.14 \cdot 10^9$ V/cm. This corresponds to the electric field an electron encounters in the first Bohr orbit of a hydrogen atom. Therefore, strong-field ionization may occur, which has been described within two different approximations, namely multi-photon or tunnel ionization.

Strong-field ionization was predicted in 1931 by Maria Göppert-Mayer [42]. In 1965, it was expressed by Keldysh [43] and the parameter, later known as the Keldysh parameter, γ was introduced. It is defined as

$$\gamma = \sqrt{\frac{I_p}{2U_p}}, \quad (2.32)$$

where I_p is the ionization potential of the specific atom and U_p the ponderomotive potential, which is a measure for the strength of the electric field. It is defined as the mean kinetic energy collected by a free electron (initially at rest) moving in the laser field and it is given by

$$U_p = \frac{e^2 E^2}{4m_e \omega_0^2}, \quad (2.33)$$

where e and m_e are the charge and the mass of an electron. The Keldysh parameter indicates, if the ionization is occurring in the multi-photon regime ($\gamma \gg 1$) or in the tunneling regime ($\gamma \ll 1$).

In table II.1 some examples of the ponderomotive potential, the Keldysh parameter and the excursion distance of an ionized electron are given for three intensities of the IR laser field that are relevant for specific physical processes to give an impression for typical, experimental conditions.

Physical process	Single-photon transition in N_2O (IR-probe pulse)	Strong-field ionization of N_2O	HHG in Ar
Intensity [W/cm^2]	$1 \cdot 10^{12}$	$5 \cdot 10^{13}$	$8 \cdot 10^{14}$
propagation distance [\AA]	0.82	5.78	23.12
Ponderomotive potential U_p [eV]	0.056	2.804	44.866
Keldysh parameter γ	10.72	1.52	0.42

Table II.1: Ponderomotive potential, propagation distance of the free electron and the Keldysh parameter for several experimentally relevant IR intensities that are similar to the conditions of the experiment described in chapter V. The considered IR-pulse parameters are: pulse duration $\tau = 25$ fs and central wavelength $\lambda_C = \frac{2\pi c}{\omega_0} = 775$ nm. For the single photon transition and the strong-field ionization the ionization potentials I_p used was 12.89, the ionization potential for the single ionization of N_2O and for the HHG the $I_p = 15.76$ eV of argon was taken, which was used to generate the high harmonics in the experiments presented.

2.1 Multi-Photon Ionization

A single IR photon ($E_{IR} \approx 1.6$ eV) has not enough energy to overcome the ionization potential of an atom as argon ($I_p \approx 15.8$ eV), which is often used for HHG and as target gas in our experiments. In the multi-photon ionization (MPI) regime ($\gamma \gg 1$), the laser intensity is high enough that there is a finite probability that several photons are absorbed simultaneously [44] to ionize an atom. Here, it is even possible that more photons are absorbed than necessary for ionization. This effect is called above-threshold ionization (ATI) [45]. Figure 2.5 shows the typical ATI photoelectron energy spectra. The photoelectrons have discrete energies, which are spaced by the IR-photon energy, and the ionization rate w decreases with the number of photons involved ($w \propto I^n$). In addition, a strong laser field approaching the non-perturbative regime induces an AC Stark shift of the atomic states. As a result, the ionization potential I_p is shifted approximately by the ponderomotive potential to $I_p^* = I_p + U_p$ [46]. In the case, the ponderomotive potential exceeds the photon energy, the low-energy peaks disappear, whereas higher-order ATI peaks arising due to the higher field strengths. Therefore this effect has been called peak shifting [47], or ponderomotive shift [46].

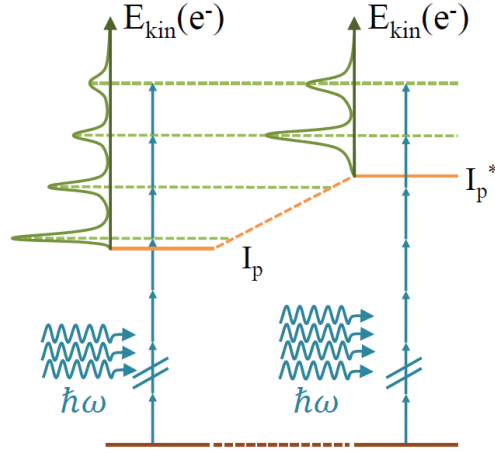


Figure 2.5: From [13]. Illustration of MPI for two different laser intensities. For higher intensities the ionization potential I_p is shifted to I_p^* due to the Stark shift. The photoelectron energy spectrum is showing the typical ATI peaks spaced by one photon energy.

2.2 Tunnel Ionization

Tunnel ionization is an approximation to describe strong-field ionization when the Keldysh parameter is $\gamma \ll 1$, at which the field strengths of the laser pulse is in the order of the Coulomb field between the nuclear core and the electron. In addition, the frequency of the electric field has to be sufficiently low, such that the atomic potential is able to follow its oscillation [46]. Then, the field distorts the atomic potential and only a barrier remains, through which the electron is able to tunnel out (see figure 3.9).

The most common expression to calculate the tunnel-ionization rate is given by the so-called ADK-formula [48]. It provides ionization rates for complex atoms and it is in good agreement with experiments [49]. The ADK ionization rate W , which is based on a quasi-classical approximation, is given by

$$W = \omega_A C_{n^*,l}^2 f(l,m) I_p \left(\frac{3E}{\pi(2I_p)^{\frac{3}{2}}} \right)^{\frac{1}{2}} \times \left[\frac{2}{E} (2I_p)^{\frac{3}{2}} \right]^{2n^* - |m| - 1} \cdot \exp \left(-\frac{2}{3E} (2I_p)^{\frac{3}{2}} \right), \quad (2.34)$$

where ω_A is the atomic unit of frequency, I_p the ionization potential, E the electric field

of the laser, the factors $f(l,m)$ and $C_{n^*,l}$ are given by

$$f(l,m) = \frac{(2l+1)(l+|m|)!}{2^{|m|}(|m|)!(l-|m|)!} \quad (2.35)$$

and

$$C_{n^*,l} = \left(\frac{2e}{n^*}\right)^{n^*} \frac{1}{(2\pi n^*)^{\frac{1}{2}}}, \quad (2.36)$$

with l the azimuthal quantum number, m the magnetic quantum number and n^* the effective principal quantum number. The change caused by effects such as electron shielding in many-electron atoms is approximated by

$$n^* = \frac{Z}{(2I_p)^{\frac{1}{2}}}, \quad (2.37)$$

where Z is the created charge of the ion. The two factors $f(l,m)$ and $C_{n^*,l}$ define the atomic structure and the term $\left(\frac{3E}{\pi(2I_p)^{\frac{3}{2}}}\right)^{\frac{1}{2}}$ results from temporal averaging over a whole laser pulse.

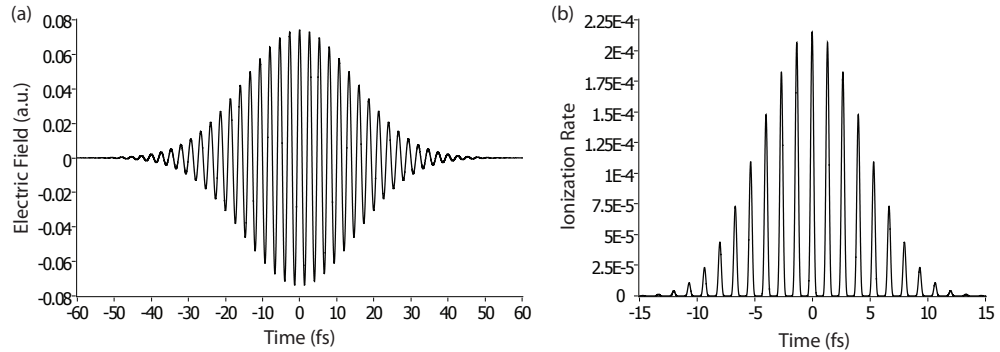


Figure 2.6: (a) A Gaussian laser pulse with 800 nm central wavelength, a FWHM of 25 fs and an electric field strength of 0.74 a.u., which corresponds to an intensity of 1.9×10^{14} W/cm². (b) The ADK ionization rate calculated for argon and the pulse shown in (a).

This model is applied to the theoretical description of the high-harmonic generation process. Technically, an IR laser beam is focused (to a few times $10^{14} \frac{\text{W}}{\text{cm}^2}$) into a gas target (typically Ar, or Ne). The corresponding Keldysh parameter is $\gamma \ll 1$ (compare with table II.1). The following section 3 will introduce the high-harmonic generation in more detail.

To give an impression for the ADK ionization rate (see equation 2.34) for conditions similar to the experiment presented in chapter V, figure 2.6(b) shows the ADK ionization rate for the single ionization of argon, which was used for HHG in the experiment and for a Gaussian shaped laser pulse shown in figure 2.6(a). The ionization rate is strongly connected to the electric field, such that only near the field maxima, the ionization occurs. Figure 2.7 illustrates the portion of ionized argon atoms as function of the temporal evolution of the assumed Gaussian pulses at different peak intensities.

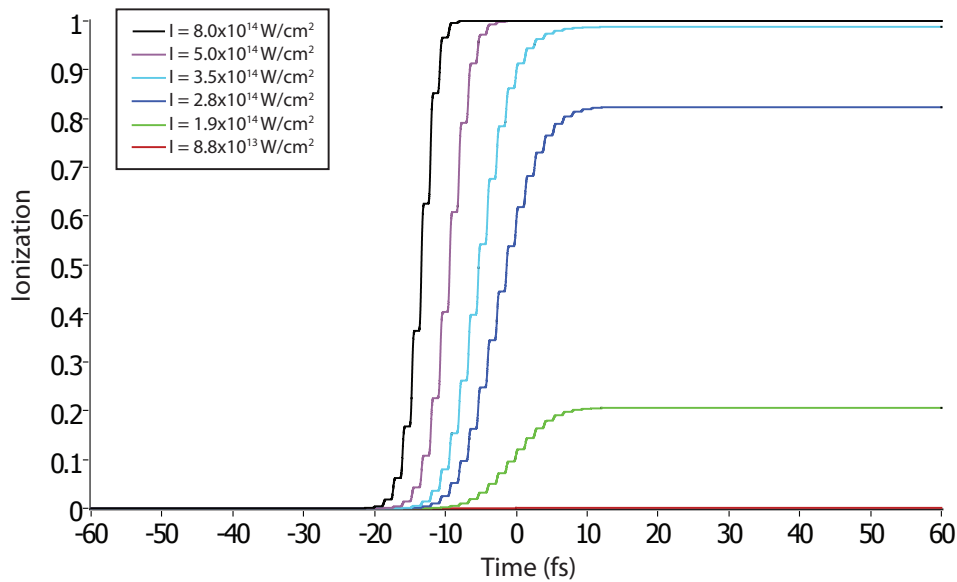


Figure 2.7: Portion of ionized argon atoms over time extracted from the ADK ionization rate for different laser intensities of a 25 fs long Gaussian laser pulse with 800 nm central wavelength.

3 High-Harmonic Generation

A typical Ti:Sa laser system produces light with a wavelength of about 800 nm. In the mid 90's it was already possible to compress such IR-Pulses to a few optical cycles [27]. A single optical cycle corresponds to a pulse length of 2.67 fs. It is impossible to further compress light pulses below this single-cycle limit. High-harmonic generation (HHG) provides a method to enter the sub-femtosecond regime. The HHG process has been known since the late eighties [7, 8]. Some years later Farkas and Toth proposed to use this technique for the creation of very short light pulses [50].

HHG is a non-linear and non-perturbative process. The harmonic light has a very characteristic spectrum, which is illustrated in figure 3.8. The spectral intensity is decreasing for the low-order harmonics followed by a long plateau. At one point, the intensity drops fast, which is called the cut-off.

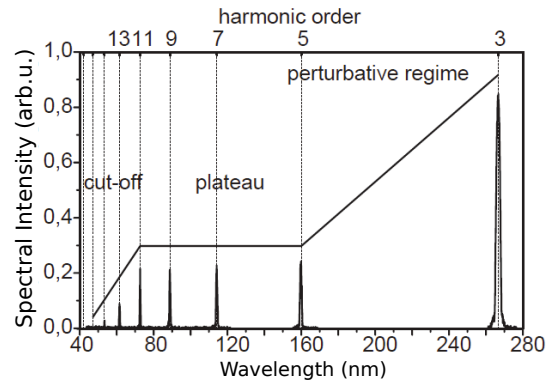


Figure 3.8: From [51]. Typical harmonic spectrum generated in xenon, showing the characteristic shape: the decreasing, the plateau and the cut-off.

Early studies tried to extend the plateau and to produce even higher-order harmonics [52, 53]. Systematic experiments in several gases showed that the cut-off energy E_{CO} is dependent on the ionization potential I_p of the target gas used for HHG as well as on the ponderomotive potential U_p of the laser, which was already introduced in equation (2.33). In 1992, the cut-off law was expressed by Krause as [54]

$$E_{CO} = I_p + 3.17U_p. \quad (3.38)$$

One year later, a simple quasi-static theory was developed that described the properties of the HHG spectra very well. This theory is known as *simple man's theory* or *three-step model* [55, 56]. It can be derived from a fully quantum-mechanical theory based on the strong-field approximation [57]. Both, the quasi-static and the quantum-mechanical approach will be discussed in the next sections.

3.1 Three-Step Model

The description of the HHG process from Corkum and Kulander is a semiclassical model. Its basic principle has been formulated earlier and was dubbed “antenna model” [58]. As the name implies, it divides the production of harmonic radiation into three steps. The fundamental laser beam firstly ionizes the electron via tunnel ionization. Afterwards, the free electron propagates within the laser field essentially unperturbed by the atom’s Coulomb potential. In some cases, the electron is finally driven back to its parent ion. There it can recombine with it under emission of a high-energetic photon. This simple model is able to reproduce the properties of the harmonic spectra and provides an insight into the atomic processes during HHG.

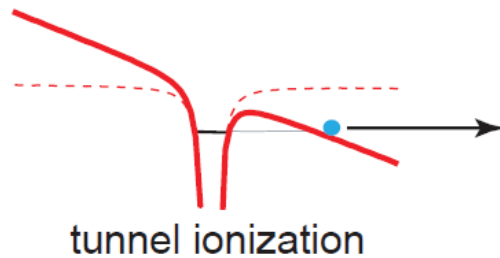


Figure 3.9: From [51]. First step: The laser bends the potential and the electron is able to tunnel out.

Step One: Ionization A high-intensity laser field $E(t)$ strongly interacts with an atomic potential. The effective potential $V(\mathbf{r}, t)$ can be approximated as composed of the Coulomb potential of a singly charged ion and the induced laser potential

$$V(\mathbf{r}, t) = \frac{e^2}{4\pi\epsilon_0 r} + e\mathbf{E}(t)\mathbf{r}. \quad (3.39)$$

This perturbation leads to a time-dependent bending of the atomic potential. At a certain time, depicted in figure 3.9, in the right-hand regime only a barrier remains, through which one of the bound electrons is able to tunnel out. The ionization rate is well described by the ADK theory, which was already introduced in section 2.2.

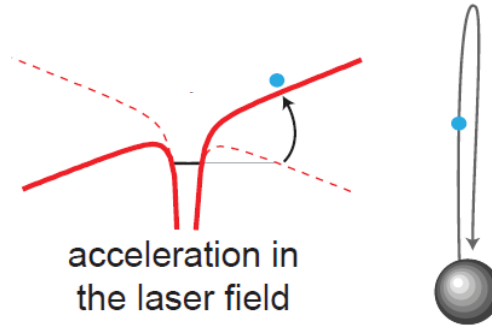


Figure 3.10: From [51]. Second step: The ionized electron moves driven by the electric field of the laser.

Step Two: Propagation The second step describes the propagation of an electron in the electric field. This field is supposed to be linear polarized and much stronger than the Coulomb potential so that the electron is only influenced by the electric field (strong-field approximation). The calculations can be reduced to a 1-D-model. After ionization, the electron is considered to be at rest and can be found in the origin ($x_0 = 0; v_0 = 0$). In doing so, a force takes effect on the electron that can be described as [55, 59]

$$F = -eE(t), \quad (3.40)$$

and this force results in an acceleration a in the oscillating laser field $E(t) = E_0 \cos(\omega t + \varphi)$

$$a = \frac{F}{m} = -\frac{e}{m_e} E(t) = -\frac{e}{m_e} E_0 \cos(\omega_0 t + \varphi), \quad (3.41)$$

with φ the phase of the laser field, at which the electron is tunneled out. Through a simple integration of the acceleration over time one can calculate the electron's velocity

$$v(t) = -\frac{eE_0}{m_e\omega_0} [\sin(\omega_0 t + \varphi) - \sin(\varphi)] \quad (3.42)$$

and integrating the velocity gives the position of the electron

$$x(t) = \frac{eE_0}{m_e\omega_0^2} [\cos(\omega_0 t + \varphi) + \omega_0 t \sin(\varphi) - \cos(\varphi)]. \quad (3.43)$$

The first to terms of equation (3.43) are time-dependent. The first one describes the oscillation of the electron with the laser field and the second one represents a drift, whose strength is defined by the phase φ . In figure 3.11 the electron trajectories are plotted. Only a few trajectories actually lead back to the parent ion where the electron is able to recombine.

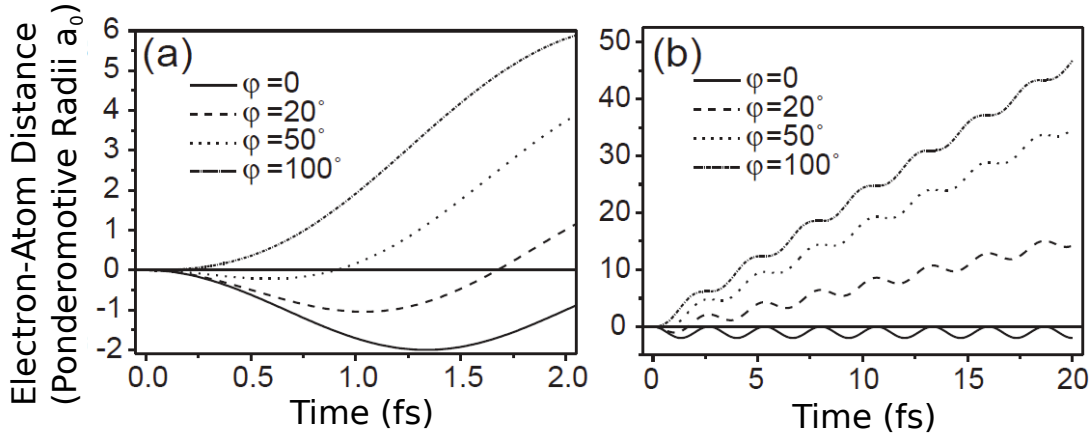


Figure 3.11: From [51]. Electron trajectories for various phases of the driving laser field, which has a central frequency of 800 nm and an intensity in the order of $10^{14} \frac{\text{W}}{\text{cm}^2}$. (a) shows an excerpt near to the origin from (b).

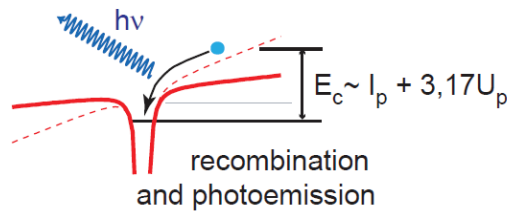


Figure 3.12: From [51]. Third step: There is a probability that the electron recombines and emits harmonic radiation, if it passes the ion again.

Step Three: Recombination The last step describes the recombination of the electron with its parent ion. After a time t , the electron returns to its initial point ($x = 0$). If the electron is captured again, a photon is emitted whose energy can be written as the sum over the ionization potential of the target atom I_p and the collected kinetic energy of the electron E_{kin} [60]:

$$\hbar\omega_{XUV}(t) = I_p + E_{kin} = I_p + \frac{1}{2}mv^2(t) \quad (3.44)$$

$$= I_p + 2U_p[\sin(\omega_0 t) - \sin(\omega_0 t_0)]^2, \quad (3.45)$$

where U_p is the ponderomotive potential and t_0 the instant of time of the ionization.

It is possible to determine a relation between the time the electron is ionized and the time it recombines with its parent ion from equation (3.43) [60]:

$$x(t) \propto \cos(\omega_0 t) - \cos(\omega_0 t_0) + \omega_0 \sin(\omega_0 t_0)(t - t_0) = 0. \quad (3.46)$$

This expression can not be solved analytically, but this equation can also be treated as differential equation by writing the $\sin(\omega_0 t_0)(t - t_0)$ as a derivative of a cos-function. Then the equation can be written as

$$\cos(\omega_0 t) - \cos(\omega_0 t_0) = \frac{d}{d(\omega_0 t)} \cos(\omega_0 t) \Big|_{t_0} (\omega_0 t - \omega_0 t_0). \quad (3.47)$$

Now, it is possible to give a graphical solution (see figure 3.13) to find the recombination time for any t_0 by drawing the $\cos(\omega_0 t)$ function. It corresponds to the Kramers-Henneberger frame, in which the ion is oscillating with $\cos(\omega_0 t)$ and consequentially, the motion of the electron is a linear shift [60]. One has to draw the tangent at the point $\cos(\omega_0 t_0)$, which has the slope $\frac{d}{d(\omega_0 t)} \cos(\omega_0 t) \Big|_{t_0} = -\sin(\omega_0 t_0)$. The point in time $t_R > t_0$, at which the tangent crosses the $\cos(\omega_0 t)$ -curve, is the recombination time for the electron emitted at t_0 .

On the basis of this graphical solution it is possible to see straightaway that electrons ionized at the maximum of the electric field ($\omega_0 t_0 = 0$) have the longest trajectory possible

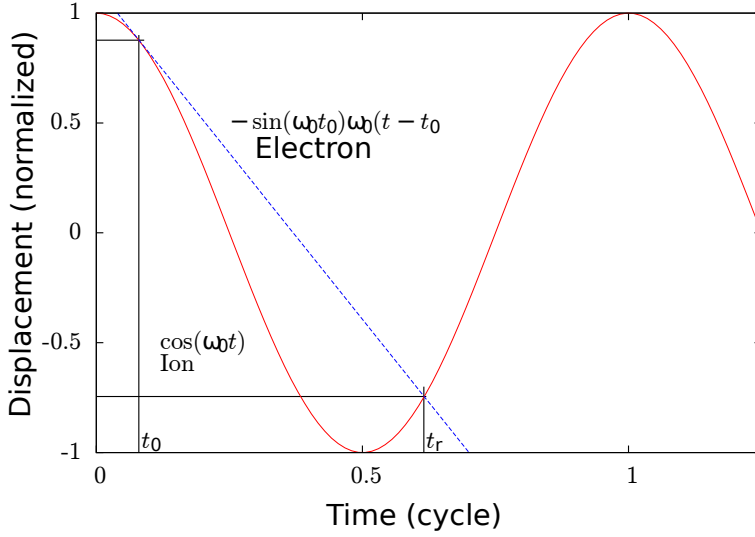


Figure 3.13: From [12]. Graphical solution for the estimation of the recombination time. The red solid line depicts the normalized ion trajectory and the blue dashed line represents the normalized electron trajectory, both in the Kramers-Henneberger frame [60].

and they are recombining exactly one optical cycle later ($\omega_0 t = 2\pi$). Electrons starting between $\omega_0 t_0 = 0$ and $\omega_0 t_0 = \frac{\pi}{2}$ as well as between $\omega_0 t_0 = \pi$ and $\omega_0 t_0 = \frac{3\pi}{2}$ have a chance to, whereas electrons leaving at all other times never return to the parent ion.

3.1.1 Return Energy and Electron Trajectories

In addition to the graphical solution, equation (3.46) can be solved numerically, at which an analytical function can be fitted. The resulting function is given by [60]

$$\omega_0 t = \frac{\pi}{2} - 3 \sin^{-1} \left(\frac{2}{\pi} \omega_0 t_0 - 1 \right). \quad (3.48)$$

This expression now defines a relation between the emission t_0 and recombination time t . With this solution it is possible to express the kinetic energy of the returned electron as function of the emission time. The kinetic energy is defined as

$$E_{kin}(\omega_0 t_0) = \frac{1}{2} m v^2(t) = 2U_p [\sin(\omega_0 t) - \sin(\omega_0 t_0)]^2. \quad (3.49)$$

Now, equation 3.48 can be inserted and this yields

$$E_{kin}(\omega_0 t_0) = \frac{1}{2} m v^2(t) = 2U_p [\cos(3 \sin^{-1}(\frac{2}{\pi} \omega_0 t_0 - 1)) - \sin(\omega_0 t_0)]^2. \quad (3.50)$$

Figure 3.14 depicts the kinetic energy, which is normalized to the ponderomotive potential U_p . The electron emitted at $\omega_0 t_0 = 0.05 \cdot 2\pi$ (and which returns at $\omega_0 t = 0.7 \cdot 2\pi$) gain the most kinetic energy, namely $E_{max} = 3.17 \cdot U_p$ as already mentioned earlier.

Figure 3.14 also shows that any kinetic energy (apart from E_{max}) can be achieved by two different electron trajectories, from which one is emitted before and one after $\omega_0 t_0 = 0.05 \cdot 2\pi$. They differ in the propagation distance and time. The electron emitted earlier is propagating longer than the one freed later and thus the corresponding trajectories are classified into long and short trajectories.

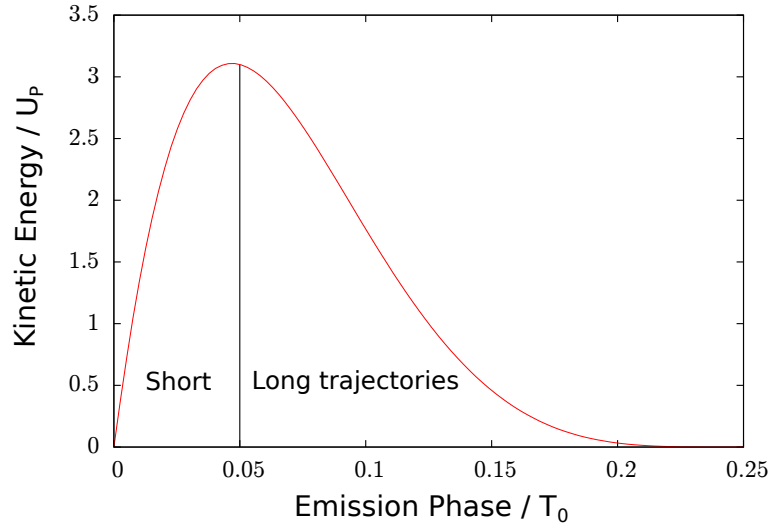


Figure 3.14: Kinetic energy of the electron at the recombination normalized to U_p versus the phase of the fundamental laser pulse at the emission time.

The presence of two trajectories yielding the same energy results in quantum path interference [61], here also leading to a visual influence on the spatial profile of the harmonic spectrum. This effect can be avoided by appropriate phase-matching conditions, which will be explained in detail in section 3.3. The long-trajectory electrons are much more sensitive (by a factor of ≈ 27) on phase effects due to the laser focusing than the short-trajectory electrons [62, 63]. Setting the right experimental conditions, the

contribution of the long-trajectory electrons to the harmonic spectrum can be suppressed [61].

3.1.2 Saturation Intensity

The above introduced cut-off law $E_{max} = I_p + 3.17 \cdot U_p$ indicates that higher harmonic energies can be expected for increasing laser intensities. At some point, this is not anymore valid without restrictions due to the high ionization rates within the target gas. As it was shown in figure 2.7, at certain intensities all target particles become ionized at the leading edge of the laser pulse. The freed electrons form a plasma and, as a consequence of this, the dispersion in the target gas will be changed. This strongly influences the so-called phase matching, which will be introduced in section 3.3, and may lead to a decreased brightness of the harmonics. But this effect can also lead to a reduction of the XUV pulse-train duration, which is called ionization gating [64, 65].

To give a more accurate expression for the cut-off law, it is necessary to account for the depletion of the ground-state population, which will be the case at a certain so-called saturation intensity I_S . Then, the maximum harmonic energy is defined by the respective ponderomotive potential $U_p(I_S)$ [60]

$$E_{max} = I_p + 3.17 \cdot U_p(I_S). \quad (3.51)$$

The saturation intensity is determined by the properties of the target species, as well as of the considered laser pulses. A detailed derivation can be found in reference [60]. It can be calculated as

$$I_S = \frac{1.7 \cdot I_p^{3.5}}{\left(\ln \left(\frac{0.86 \cdot |C_{n^*,l}|^2 \cdot f(l,m) \cdot I_p \cdot 3^{(2n^* - |m| - 1)} \cdot \tau}{-\ln(1 - p_s)} \right) \right)^2} \times 10^{12} \frac{\text{W}}{\text{cm}^2}, \quad (3.52)$$

with I_p being the ionization potential in eV of the target medium, $C_{n^*,l}$ and $f(l,m)$ are factors defining the atomic structure (see equations 2.36 and 2.35), n^* the effective principal quantum number (see equation 2.37), m the magnetic quantum number, τ the pulse duration in fs and p_s the ionization probability at the peak of the considered pulse, which can be obtained from the ADK ionization rate given in equation 2.34.

The saturation intensity and the corresponding maximum harmonic energy can be estimated for the experimental conditions of the experiment shown in chapter V. The laser

pulses had a duration of 25 fs and, for the calculation of the ADK rate, a Gaussian shaped pulse is used that have a central wavelength of 775 nm. The harmonics are generated in argon, which has an ionization potential of 15.76 eV and single ionization is assumed. With these parameters the saturation intensity is in the order of $I_S \approx 2.25 \times 10^{15}$ W/cm², with which a ponderomotive potential of $U_p(I_S) = 126.19$ eV is achieved. According to equation 3.51, the highest possible harmonic energy is $E_{max} = 415.78$ eV. The XUV-photon energies observed in the experiment are considerably lower, namely below 50 eV (see figure 10.7), which would correspond to an ponderomotive potential in the order of $U_p \approx 10.8$ eV and a laser intensity of approximately $I = 1.92 \times 10^{14}$ W/cm².

3.2 Quantum-Mechanical Model

The HHG process can also be described by a full quantum-mechanical model. This model was introduced in the mid-90s [57, 66]. Here, the laser field $E_0 \cos(\omega t + \phi)$ is considered to be polarized in x -direction and only a single electron is active (single-active electron approximation[67]). The electron is treated as wave function $\psi(\mathbf{x}, t)$, which has to fulfill the time-dependent Schrödinger equation. It can be written as

$$i|\psi(\mathbf{x}, t)\rangle = \left[-\frac{1}{2}\nabla^2 + V(\mathbf{x}) - E \cos(t)x\right]|\psi(\mathbf{x}, t)\rangle. \quad (3.53)$$

For the solution of this differential equation, it is assumed that all bound states, except the ground state $|0\rangle$ are neglected as well as its depletion. In addition, similar to the semi-classical model the ionized electron is treated as free particle unperturbed by the Coulomb potential of the ion (strong-field approximation). The resulting wave function is given by

$$|\psi(t)\rangle = \exp(iI_p t)(a(t)|0\rangle + \int d^3\mathbf{v} b(\mathbf{v}, t)|\mathbf{v}\rangle), \quad (3.54)$$

where $a(t) \approx 1$ is the ground state amplitude and $b(\mathbf{v}, t)$ are the corresponding continuum state amplitudes of the velocity of the electron \mathbf{v} . The time-dependent dipole moment $X(t)$ can be calculated using this exact solution of the Schrödinger equation:

$$X(t) = \langle\psi(t)|X|\psi(t)\rangle = \int d^3\mathbf{v} d_x^*(\mathbf{v})b(\mathbf{v}, t) + c.c., \quad (3.55)$$

where $d(\mathbf{v}) = \langle v|X|0\rangle$ is the transition matrix element between ground and continuum state and $d_x(\mathbf{v})$ is its component parallel to the polarization direction of the electric field. Here, the canonical momentum \mathbf{p} in atomic units ($m_e = 1$ and $e = 1$) is introduced

$$\mathbf{p} = \mathbf{v} + \mathbf{A}(t), \quad (3.56)$$

$\mathbf{A}(t)$ denotes the vector potential of the electric field. With this the dipole moment can be written as [68]

$$X(t) = i \int_0^t dt' \int d^3\mathbf{p} E \cos(t') d_x(\mathbf{p} - \mathbf{A}(t')) \times d_x^*(\mathbf{p} - \mathbf{A}(t)) \exp(-iS(\mathbf{p}, t, t')) + c.c., \quad (3.57)$$

where

$$S(\mathbf{p}, t, t') = \int_{t'}^t dt' \left(\frac{(\mathbf{p} - \mathbf{A}(t'))^2}{2} + I_p \right) \quad (3.58)$$

is the quasi classical action. A closer look on equation (3.57) reveals that the quantum mechanical model also contains the three steps. The first term in the integral $E \cos(t') d_x(\mathbf{p} - \mathbf{A}(t'))$ is the probability amplitude for the transition of an electron from the ground state to a continuum state at time t' and with the canonical momentum \mathbf{p} . Thereafter, the electron propagates until the time t and along the way it collects a phase, which is equivalent to $\exp(-S(\mathbf{p}, t, t'))$. Finally, the last term $d_x^*(\mathbf{p} - \mathbf{A}(t))$ indicates the probability, with which the electron recombines with its parent ion at time t .

In the quantum mechanical model several effects are taken into account, such as spreading of the electron wave function during propagation or interference effects. Nevertheless, it approves the semi-classical theory. All electron trajectories not described by the semi-classical model vanish through fast oscillations. Therefore, the free electrons in the laser field can be described classically using the depicted approximations [69].

3.3 Phase Matching

The models introduced above described the HHG process on a single atom level. The HHG signal measured in experiment is the interference of the pulses emitted by many atoms

in the generation medium. The resulting macroscopic harmonic radiation is influenced by propagation effects in the gaseous generation medium. To gain a macroscopically detectable signal, the single waves emitted from each atom in the medium have to interfere constructively. Therefore, the emitted radiation has to be in phase with the fundamental laser field over a major part of the high-harmonic conversion volume and, thus, the signals of all contributing atoms. The phase-mismatch of the q -th harmonic to the fundamental laser field can be expressed by [51, 67]

$$\Delta k = qk(\omega_f) - k(q\omega_f), \quad (3.59)$$

where ω_f is the fundamental frequency. The frequency dependence of the wave vector k is effected mainly by three different factors:

- The refractive index of the harmonic-generation medium k_{disp}
- The dispersion in the plasma formed by ionized electrons within in the generation medium k_{pl}
- The focusing of the laser k_{geom}

The total wave vector k writes as

$$k = k_{vac} + k_{disp} + k_{pl} + k_{geom}, \quad (3.60)$$

where

$$k_{vac} = \frac{2\pi\omega}{c} \quad (3.61)$$

is the wave vector in the vacuum. For its mismatch one yields

$$\Delta k = \Delta k_{vac} + \Delta k_{disp} + \Delta k_{pl} + \Delta k_{geom} \quad (3.62)$$

with

$$\Delta k_{vac} = q\frac{\omega_f}{c} - \frac{q\omega_f}{c} = 0. \quad (3.63)$$

Neutral Dispersion The speed of light propagating through a dispersive medium is dependent on the particular wavelength-dependent refractive index $n(\omega)$. Consequentially, the

fundamental IR pulses and the HHG radiation are propagating with different velocities. The refractive-index dependent wave vector is defined by

$$k_{disp}(\omega) = (n(\omega) - 1) \frac{\omega}{c}. \quad (3.64)$$

and the mismatch for the q th harmonic at the spectral frequency $q\omega_f$ with respect to the fundamental frequency ω_f is given by

$$\Delta k_{disp} = qk_{disp}(\omega_f) - k_{disp}(q\omega_f) = (n(\omega_f) - n(q\omega_f)) \frac{q\omega_f}{c}. \quad (3.65)$$

The refractive index is higher for the near-infrared driving laser fields than for the XUV-pulses, therefore the phase mismatching is always positive

$$\Delta k_{disp} > 0. \quad (3.66)$$

The neutral dispersion can be influenced by the choice of the gas used for HHG. It is also possible to use compounds of several gaseous media [70].

Plasma Dispersion The strong IR laser field is able to ionize a huge number of electrons. Only a small part recombines with their parent ion to emit high-harmonic radiation. The residual electrons can stay free for several ns and build a plasma. This free-electron plasma also has a wavelength-dependent refractive index $n_{pl}(\omega)$

$$n_{pl}(\omega) = \sqrt{1 - \left(\frac{\omega_p}{\omega}\right)^2} = \sqrt{\left(1 - \left(\frac{N_e}{N_c(\omega)}\right)\right)}, \quad (3.67)$$

where $\omega_p = \sqrt{\frac{e^2 N_e}{\epsilon_0 m_e}}$ is the plasma frequency, N_e is the density of free electrons and N_c the critical plasma density. If a critical plasma density $N_c = \frac{\epsilon_0 m_e \omega_c^2}{e^2}$ is reached, electromagnetic radiation at frequency ω_c is efficiently absorbed by the plasma. At typical HHG conditions the free-electron density is much lower than the critical density and therefore equation(3.67) can be approximated by

$$n_{pl}(\omega) \approx 1 - \frac{1}{2} \left(\frac{\omega_p}{\omega}\right)^2. \quad (3.68)$$

For the k -vector it yields

$$k_{pl}(\omega) = (n_{pl}(\omega) - 1) \frac{\omega}{c} = -\frac{\omega_p^2}{2c\omega} \quad (3.69)$$

and correspondingly

$$\Delta k_{pl} = qk_{pl}(\omega_f) - k_{pl}(q\omega_f) = \frac{(1 - q^2)\omega_p^2}{2cq\omega_f}. \quad (3.70)$$

In general, the harmonic order is $q \gg 1$, the distribution of the plasma dispersion is negative:

$$\Delta k_{pl} < 0. \quad (3.71)$$

Geometrical Dispersion In the experimental setup used for this work, the IR beam is focused by a focusing mirror in a static gas target in order to produce harmonic radiation. Around the focus, the phase of the laser beam changes. The beam waist of a Gaussian beam in the focus w_0 is defined by the focal length f , the beam size at the focusing optical element w_l and the wavelength λ

$$w_0 = \frac{f}{\pi w_l} \lambda. \quad (3.72)$$

The beam diameter $w(z)$ can also be described as a function of the position z on the propagation axis, with $z = 0$ being the focal position:

$$w(z) = w_0 \sqrt{1 + \left(\frac{z}{z_R}\right)^2}, \quad (3.73)$$

with the Rayleigh length

$$z_R = \frac{\pi w_0^2}{\lambda}. \quad (3.74)$$

For the Gouy-phase evolution one obtains

$$\phi_{foc} = -\arctan\left(\frac{\lambda z}{\pi w_0^2}\right) = -\arctan\left(\frac{z}{z_R}\right). \quad (3.75)$$

Now, the wave vector can be derived from the phase:

$$\mathbf{k}(\mathbf{r}) = \nabla\phi(\mathbf{r}). \quad (3.76)$$

In the discussed case it is

$$k_{geom}(\omega) = -\frac{d\phi_{foc}(z)}{dz} = -\frac{2}{(b + \frac{4z^2}{b})}, \quad (3.77)$$

where b is the confocal parameter and is given by $b = 2z_R$. This only affects the fundamental laser beam, therefore the phase mismatch is given by

$$\Delta k_{geom} = qk_{foc}\omega_f - \underbrace{k_{foc}(q\omega_f)}_{=0} = -\frac{2q}{(b + \frac{4z^2}{b})}. \quad (3.78)$$

This distribution is always $\Delta k_{foc} < 0$ and its strength varies with the focal position.

Total Phase Matching With all the contributions to the phase mismatch it is possible to summarize this into one equation

$$\Delta k = \Delta k_{disp} + \Delta k_{plasma} + \Delta k_{geom} \quad (3.79)$$

$$= (n(\omega_f) - n(q\omega_f))\frac{q\omega_f}{c} + \frac{(1 - q^2)\omega_p^2}{2cq\omega_f} - \frac{2q}{(b + \frac{4z^2}{b})}. \quad (3.80)$$

The output of the HHG is most efficient, if $\Delta k = 0$. In the experiment there are several parameters to minimize Δk , e.g. the intensity and pulse length of the fundamental IR-laser pulse, the focal length, the position of the gas cell with respect to the focal position, the pressure of the generation medium and the type of gas used for HHG.

With a given phase mismatch $\Delta k \neq 0$ it is possible to approach the expected harmonic yield by [64, 71]

$$I \propto \text{sinc}^2\left(\frac{\pi}{2} \frac{L}{L_c}\right), \quad (3.81)$$

where $\text{sinc}(x) = \frac{\sin(x)}{x}$, L is the interaction length and $L_c = \frac{\pi}{\Delta k}$ the coherence length. Another interesting measure is the absorption length L_a , the distance, after which the

intensity of light propagating through a medium decreased to $\frac{1}{e}$. It is defined as

$$L_a = \frac{1}{\rho\sigma}, \quad (3.82)$$

where σ is the photo-ionization cross-section and ρ the particle density. Figure 3.15 shows the output photon flux as function of the medium lengths L for different coherence lengths L_c . For an efficient HHG production L_c should be sufficiently long ($L_c > L_a$). According to the fact that L_a limits the harmonic generation, the interaction length should be at least $L > 3L_a$ but it is unnecessary to increase the medium length too much, since the intensity saturates with growing L .

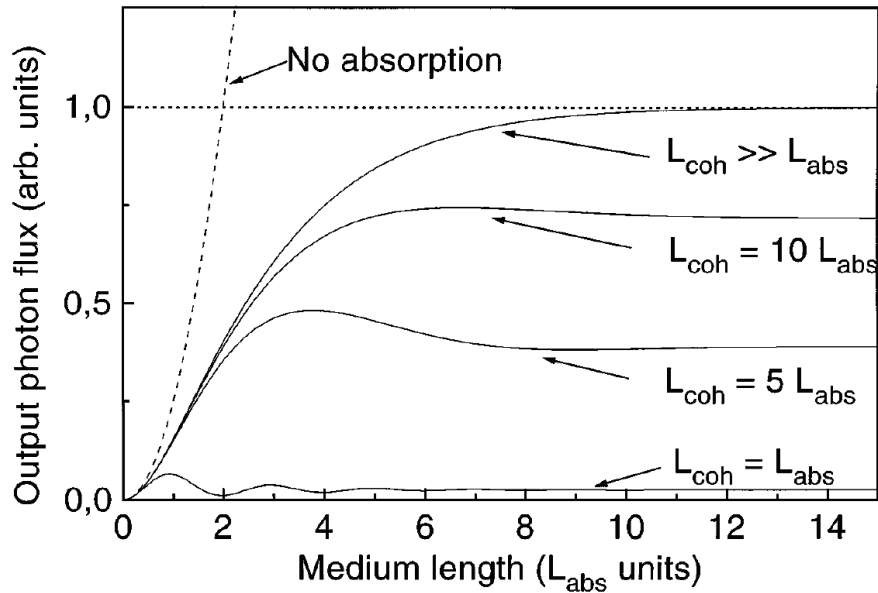


Figure 3.15: From [71]. The output intensity in arbitrary units in relation to the medium length in units of the absorption length.

3.4 Attosecond Pulse Trains

The HHG process occurs every half cycle of the laser pulse, at which the electric field is strong enough to tunnel-ionize an electron. As a result an attosecond pulse train (ATP) is generated. The pulse duration of the individual XUV pulses is shorter than the oscillation period of the driving IR laser field. The returning time of the electrons spreads over 75% of the laser period $T_0 = 2.67$ fs, suggesting the generated pulses are in the same order

of magnitude and their FWHM is in the order of $0.75T_0 \times 0.5 \approx 1$ fs, which approaches the subfemtosecond regime. In case the long trajectory contribution is suppressed by phase matching (see section 3.1.1), the duration of the XUV pulses reduces to ~ 600 as at FWHM [60].

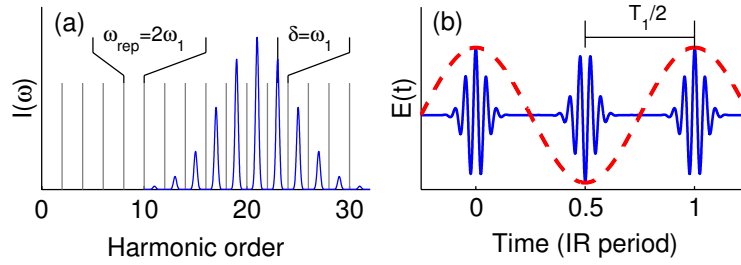


Figure 3.16: From [72]. Illustration of an APT (a) in the frequency domain and (b) in the time domain. The frequency components are spaced by twice the fundamental frequency, whereas the attosecond pulses are generated every half cycle of the laser field.

The temporal profile I_{XUV} of the ATP train can be approximated as sum over the single Frequency components:

$$I_{XUV} = \left| \sum_{q_{\text{odd}}} A_q \exp(-i\omega_q t + i\phi\omega_q) \right|^2, \quad (3.83)$$

with A_q and ϕ_q the Amplitude and phase at the energy of the harmonic order q . The phase is dependent on the phase matching, which is explained in section 3.3. With perfect phase matching, the single-pulse duration of the harmonic radiation is $T_0/2N$ concerning N involved frequency components [73]. The generated frequency components are spaced by a multiple of the frequency of the driving laser field (see figure 3.16). Their spacing is connected via Fourier transformation to the repetition rate of the process, which is $T_0/2$. As a result, the frequency components are spaced by twice the fundamental frequency and only odd harmonics are produced.

3.5 Sidebands

So far, solely the production of harmonic radiation was described. However, in the experiment they are used again to interact with an atom or molecule. We consider now an atom with at least one electronic state with an ionization potential lower than the photon energies of the XUV pulses ($I_p < E_{XUV}$). In this case, the atom can be singly ionized by

one XUV photon. The resulting kinetic energy of the freed electron E_e corresponds to the difference between the ionization potential I_P and the photon energy E_{XUV}

$$E_e = E_{XUV} - I_P. \quad (3.84)$$

The harmonic spectrum is consisting of frequency components that are equally spaced by twice the frequency of the fundamental driving laser pulse $2\omega_0$. This characteristic structure also emerges in the photoelectron spectrum. They are separated by the energy difference between two harmonics $2\hbar\omega_0 \approx 3.2$ eV. In addition, the intensity distribution of the harmonic spectrum is impressed onto the intensity distribution of the photoelectron spectrum modified by the photon energy-dependent photo-ionization cross-section [12].

The so-called sidebands occur when an additional weak IR-field ($I_{IR} \approx 10^{11} \text{ W/cm}^2$) is present during the ionization process. This field is interacting with the electrons and they can absorb or emit an additional photon from the IR field (see figure 3.17). Due to the fact that the energy spacing of the photoelectrons is twice the fundamental frequency, the sidebands appear exactly in the middle between two harmonic peaks. In literature, this effect is called laser-assisted photoelectric effect (LAPE) [74].

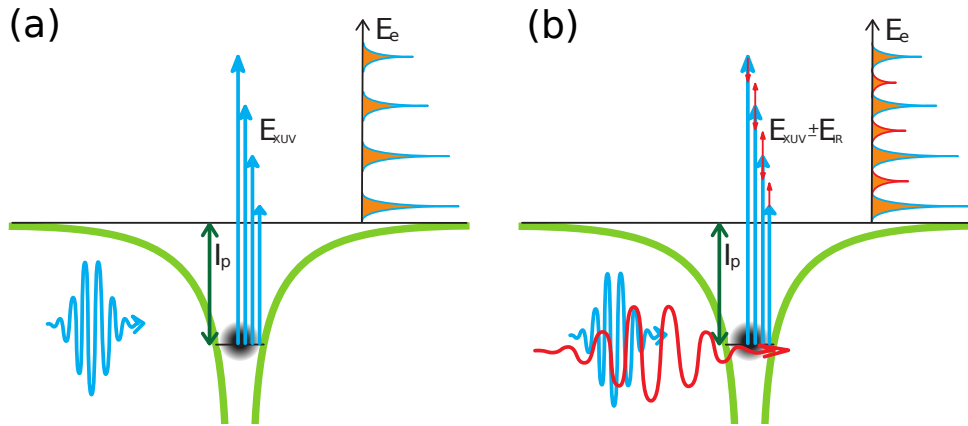


Figure 3.17: From [12]. (a) Photo-ionization with the harmonic radiation only and (b) with an additional weak IR-field. The ionized electrons can absorb or emit an extra photon from the IR field and the sidebands occur.

For the production of the sidebands both the XUV and the IR have to be present at the ionized atom. The process can also be interpreted as cross-correlation and, thus, the intensity profile of the sidebands $S(\tau)$ is proportional to the intensity of the IR

and XUV pulses [75] with a temporal intensity profile τ_{TPI} being a convolution of the intensity-envelope of the XUV-pulse train τ_{XUV} and of the IR-Pulse τ_{IR} over the delay time t [74]

$$S(\tau) \propto \int_{-\infty}^{+\infty} I_{\text{XUV}}(t - \tau) I_{\text{IR}}(t) dt. \quad (3.85)$$

Assuming Gaussian pulses, the relation between the pulse durations are given by

$$\tau_{\text{XUV}} = \sqrt{\tau_{\text{TPI}}^2 - \tau_{\text{IR}}^2 - \tau_{\text{geo}}^2}, \quad (3.86)$$

where τ_{geo} is a geometrical quality factor in the case the IR and the XUV beams are not propagating collinearly [76].

Furthermore the sidebands can not only be used to characterize the temporal intensity profile of the ATP and the IR pulse, even the chirp of the of the harmonics can be estimated as well as the electric field of the single pulses of the APT. The technique used to interpret the sidebands is called reconstruction of attosecond harmonic burst by interference in two photon transition (RABITT). It should not be explained here, but for more information, in [12] this technique is described in detail and it was used to study sideband oscillations in several gases as well as to reconstruct the attosecond pulse trains produced in our HHG setup.

4 Molecules

The experiments presented in this work are concerned with nitrous oxide (N_2O). This triatomic molecule has a linear shape with the two nitrogen atoms on one and the oxygen atom on the other side. With an XUV pulse ($\sim 17 - 45$ eV), which is produced via HHG as described in the previous chapters, we are pumping the system by single and double ionization, and by populating many excited electronic states with additional vibrational and rotational levels. After a variable time delay Δt a part of the fundamental IR beam, produced in the Ti:Sa amplifier system, probes the current state of the system. By varying Δt dynamical processes can be imaged. This chapter will briefly introduce a general theoretical description of polyatomic molecules, showing the respective Schrödinger equation and explains the spectroscopic notation of the molecular orbitals. Thereafter, some properties of the excitation of molecular systems in XUV fields will be discussed with special attention given to the Franck-Condon principle, the role of different vibrational modes, and to the introduction of the pump-probe technique.

4.1 General Description

Molecules are bound system of at least two nuclei and one or more electrons and they cannot be treated just simply as a sum over the involved atoms. The single atoms are interacting with each other building complex systems in a state balanced between attraction and repulsion. Even for the simplest molecular system, H_2^+ , it is impossible to solve the respective Schrödinger equation analytically without any simplification. Therefore, it is necessary to ease the problem by introducing some approximations. One of the most important approaches, called the Born-Oppenheimer approximation, is provided by an intrinsic feature of the constituents of the molecules, namely the large difference between the masses of the nuclei and the electrons, whereas the forces acting on the particles are comparable. As a result, nuclear and electronic dynamics occur on different time scales, separated by a factor of approximately 10^3 , such that both can often be treated separately in good approximation. Regarding dynamical processes of the electrons, the position of the nuclei can be assumed to be stationary.

4.1.1 Born-Oppenheimer Approximation

A quantum mechanical system is described by its total wave function Ψ , which can be found by solving the time-independent Schrödinger equation [77]

$$\mathcal{H}\Psi = E\Psi, \quad (4.87)$$

where \mathcal{H} is the Hamiltonian, an operator corresponding to the total energy of the considered system, of which the wave function Ψ is an eigenfunction and E an energy eigenvalue. Assuming all involved particles interacting through the Coulomb force solely, the Hamiltonian for a molecule consisting of i nuclei with mass M_i and momentum P_i , and j electrons with mass m_j and momentum p_j is given by [78]

$$\mathcal{H} = \sum_i \frac{P_i^2}{2M_i} + \sum_j \frac{p_j^2}{2m_e} + V(Q_i, q_j), \quad (4.88)$$

with $\frac{P_i^2}{2M_i}$ and $\frac{p_j^2}{2m_j}$ the respective kinetic energy operators for the nuclei and electrons, in which P_i and M_i are the nuclear and p_j and m_e the electronic momenta and masses, and $V(Q_i, q_j)$ the total potential energy of the system. Q_i and q_j represent the nuclear and electronic coordinates. In order to gain the potential energy term one has to account for the Coulombic interaction between all combinations of charged particle pairs, resulting in [78]

$$V(Q_i, q_j) = \sum_{j < k} \frac{e^2}{r_{jl}} + \sum_{i < k} \frac{Z_i Z_k e^2}{r_{ik}} - \sum_{ij} \frac{Z_i e^2}{r_{ij}}, \quad (4.89)$$

in which r_{jl} , r_{ik} , and r_{ij} are the distances between the j^{th} and l^{th} electron, the i^{th} and the k^{th} nucleus, and the i^{th} nucleus and the j^{th} electron, respectively, and Z_i and Z_k are the atomic numbers of the considered nuclei.

Now, in the Born-Oppenheimer approximation it is assumed that, considering the electronic dynamics, the nuclear position can be treated as fixed. As a result, the kinetic energy term of the nuclei in equation (4.88) is 0 and the Schrödinger equation can be

written as

$$\left(\sum_j \frac{p_j^2}{2m_e} + V(Q'_i, q_j) \right) \psi(Q'_i, q_j) = E'(Q'_i) \psi(Q'_i, q_j). \quad (4.90)$$

In this case, $\psi(Q'_i, q_j)$ is an electronic wave function with the corresponding eigenvalue $E'(Q'_i)$ and the nuclei are at fixed positions at $Q_i = Q'_i$. For a different set of nuclear positions Q''_i , the potential energy, as well as the electronic energy eigenfunctions and eigenvalues will alter. Solving the Schrödinger equation for a sufficient number of different sets of Q_i , will reveal the dependence of the wave functions and energies to q_j and Q_i , resulting in e.g. the potential energy surfaces (PES), which represent the energy eigenvalue of the electrons as a function of the distance between two fractions of the molecule. One important assumption here is that the electronic wave function adapts instantaneously to changes of the nuclear coordinates.

Then, the total wave function $\Psi(Q_i, q_j)$ can be expressed as product of the electronic wave function $\psi(Q_i, q_j)$ and the nuclear wave function $\chi(Q_i)$

$$\Psi(Q_i, q_j) = \psi(Q_i, q_j) \chi(Q_i). \quad (4.91)$$

Equation (4.91) can be inserted into the Schrödinger equation (4.87) to find the energy eigenvalues E of the total system. The total energy of the molecule is then determined mainly by three contributions: the total energy of the electrons, and the kinetic energies of the vibrational and the rotational motion of the nuclear particles. The energy spacing of electronic states is in the order of several electron volts (eV), leading to times of several hundreds of attoseconds (as) for electronic dynamics, whereas vibrational states have energy separations of approximately 0.1 eV and their motion occurs in the range between a few and hundred femtoseconds. Finally, the rotational motion proceeds within picoseconds with energies in the μeV range.

4.1.2 Spectroscopic Notation

Even with approximations, the solution of the Schrödinger equation for molecules is a hard task, which can be performed e.g. via the Hartree-Fock method [79]. The resulting single-electron wave functions are also called molecular orbitals and they can, for example, be described as linear combination of atomic orbitals [78].

Unlike spherically symmetric atoms, the molecular orbitals have more complex symmetry properties. Linear molecules such as the triatomic nitrous oxide, on which the experiments presented in this work are mainly concentrated, have a cylindrical symmetry. The electronic states of molecules are labeled with respect to their angular momentum and their symmetry properties. The spectroscopic notation is given by [80]

$$^{(2S+1)}\Lambda_{g/u}^{(+/-)}. \quad (4.92)$$

Here, Λ denotes the projection of the total orbital angular momentum L_z onto the molecular axis ($L_z = \hbar\Lambda$). Similar to the notation of atoms, the different states with $\Lambda = 0, 1, 2, 3, \dots, L$ are entitled by (capital) Greek letters $\Sigma, \Pi, \Delta, \Phi, \dots$. The multiplicity $2S + 1$ is defined by the total spin S , which is the sum over all spins of the involved electrons. It indicates the multiplet splitting of the corresponding state.

The remaining two terms $(+/-)$ and g (erade), and u (ngrade) are connected to the symmetry properties of the molecule. Concerning linear molecules, the eigenfunction can be reflected on a plain including the molecular axis. Then, the $+$ and $-$ sign denotes whether the sign of the eigenfunction is changed or preserved upon the reflection. Analogously, the wave function can also be reflected on a plain perpendicular to the molecular axis, which passes through the center of mass of the molecule. In this case, g assigns the preservation and u the change of the sign of the eigenfunction. The latter is only applicable for homonuclear molecules [81].

Additionally, the states can be classified by a prefixed label consisting of Latin letters X, A, B, C, \dots , at which X is the ground state and the other ones are higher excited states with increasing energy. To give an example, the ground state of H_2 can be written as $X^1\Sigma_g^+$.

4.2 Molecules in XUV Light Fields

The interaction of light with an atomic or molecular system is a substantial part of our experiments. Previously, it was already briefly discussed, how the IR laser pulses interact with atomic systems. In most cases, its photon energy of approximately 1.6 eV is not sufficient for ionization with a single photon. Increasing the intensity of the laser pulses enables processes such as multi-photon, tunnel, or over-the-barrier ionization. For the latter two the strong electric field significantly modifies the Coulomb potential of the atom or molecule. In contrast, the energy of the XUV radiation, which we are generating for our

experiments within an energy range of 17 – 45 eV, is sufficient to access various excited, singly and even doubly ionized states with one photon. In this interaction, electrons are lifted to energetically higher states, possibly provoking a vibrational or rotational motion of the molecule, or dissociation.

4.2.1 The Franck-Condon Principle

As already introduced for the Born-Oppenheimer approximation, electron dynamics are much faster than the motion of the nuclei. As a result, electronic transitions occur instantaneously as compared to the time scale of nuclear dynamics. That means, the internuclear distance R remains unchanged during an electronic transition from one to another electronic state. This is known as the Franck-Condon principle and it is illustrated in figure 4.18, in which the vertical blue arrows correspond to an excitation of an electron from one to another state at a fixed value of R .

In this context, it is interesting to look on the transition probabilities between the different states and vibrational levels. The nuclei in the different vibrational levels can be approximated by linear harmonic oscillator wave functions. In the vibrational ground state, the spatial nuclear wave function has its largest expectation value at the equilibrium internuclear distance R_{eq} . Regarding excited vibrational states, the probability density is largest at the classical turning points.

Let us consider the electronic transition from the state k to state l , with the respective total wave functions Ψ_k and Ψ_l . The transition amplitude is proportional to the transition matrix element $D_{kl} = \langle \Psi_l | D | \Psi_k \rangle$ of the electric dipole operator D , which is given by [83]

$$D_{kl} = \int \chi_l^* D_{kl}^{el} \chi_k d^3R, \quad (4.93)$$

in which χ_i are the nuclear wave function and D_{kl}^{el} is the electronic part of the dipole operator matrix element. Additionally, the nuclear wave function is a product of a vibrational wave function $S_{vib}(R, \nu)$, and a rotational wave function $Y_J^M(\Theta, \phi)$, where ν is the vibrational quantum number, J is the rotational angular momentum, $M\hbar$ is its projection on the molecular axis, Θ the polar, and ϕ the azimuthal angle. Then, D_{kl} can be written as

$$D_{kl} = \int S_{vib}(\nu'') D_{kl}^{el} S_{vib}(\nu') R^2 dR \int \int Y_{J''}^{M''} Y_{J'}^{M'} d \cos \Theta d\phi. \quad (4.94)$$

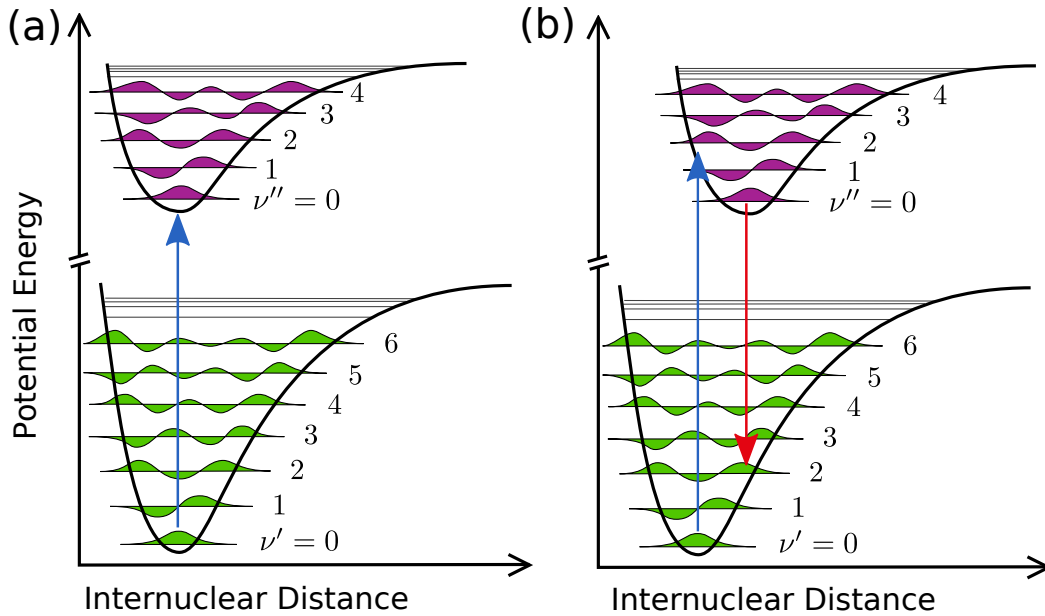


Figure 4.18: Adapted from [82]. Potential energy curves for two different states (a) with the same equilibrium distance and (b) with different equilibrium distances. According to the Franck-Condon principle electronic transitions between two states are on vertical lines since the nuclear positions are treated as fixed. The arrows indicate possible transition paths following the Franck-Condon principle: the higher the spatial overlap of the vibrational wave functions of different states, the higher is the transition probability. The blue arrows represent an excitation process from the vibrational ground state of the lower lying state. In (a) it is most likely that the electron populates the vibrational ground, whereas in (b) the highest spatial overlap is achieved in an excited vibrational level $\nu'' = 2$. The red arrow in (b) depicts a relaxation process from an excited state, which is in the vibrational ground state $\nu'' = 0$ to a lower state. In the illustrated case, a transition to a vibrationally excited state will be favored.

The Franck-Condon principle claims that D_{kl}^{el} is independent of the internuclear distance R . Then, it can be moved out from the integral. The absolute square of the remaining part

$$q_{\nu', \nu''} = \left| \int S_{vib}(\nu'') S_{vib}(\nu') R^2 dR \right|^2 \quad (4.95)$$

is known as the Franck-Condon factor, which indicates that the transition probability between two vibrational levels depends on the spatial overlap of the two corresponding vibrational wave functions. In figure 4.18 some examples for the most probable transitions

are shown.

4.2.2 Vibrational Modes

As seen before, after the transition from one state to another state, the considered molecule can be in an excited vibrational state. In a polyatomic molecule the bond lengths can be compressed or stretched. In addition, the bond angles can be modified. In general, a linear molecule consisting of N atoms has $3N - 5$ normal modes of vibration. In triatomic molecules, as e.g. N_2O , mainly three different vibrational modes are distinguishable, namely the symmetric ν_1 , the antisymmetric stretching mode ν_2 and the bending mode ν_3 , which are depicted in figure 4.19.

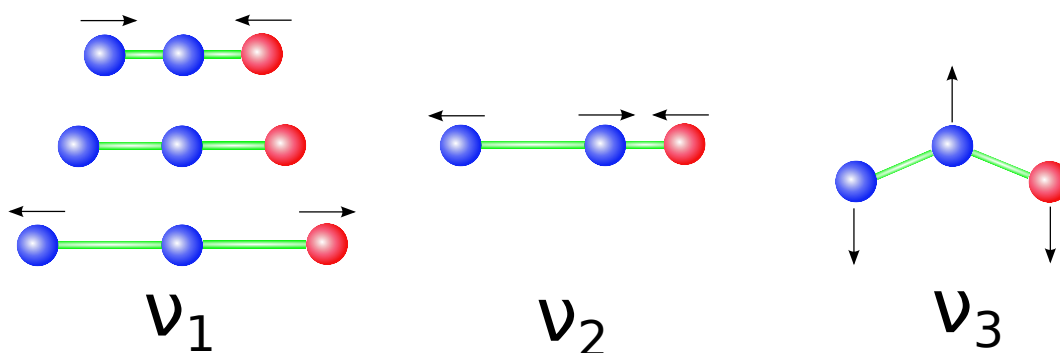


Figure 4.19: Adapted from [79]. Illustration of the three main vibrational modes: ν_1 the symmetric stretching mode, ν_2 the antisymmetric stretching mode and ν_3 the bending mode.

For a molecule, which is in a symmetric stretching mode, the bond lengths are stretched or compressed, such that the center of mass of the whole system is unchanged. In the asymmetric stretching mode, one molecular bond is stretched while the other one is compressed. In the first two cases, the vibrational motion of the nuclei is on the respective bond axis. Additionally, the terminal nuclei can move perpendicular to the molecular axis, which results in a change of the bond angles [78].

4.3 XUV-IR Pump-Probe Experiments

Studying electronic transitions and vibrational motion of molecules requires temporal resolutions in the regime from several hundred attoseconds to a hundred femtoseconds. No detection system can provide such a resolution. In the experiments presented in this

work, we are therefore using the so-called pump-probe technique. For its invention Ahmed Zewail was awarded with the Noble Prize in chemistry in 1999 [84].

In this technique a first, so-called pump pulse initializes a dynamical process in the considered system by promoting it into an excited (or even ionized) state. Subsequently, a second, so-called probe pulse interacts with the target at a variable time delay and a signal is recorded, such as absorption or fluorescence of the considered system [85], or, as shown in this work, the 3D momenta of the generated charged fragments. With sufficient time steps, a dynamic process can be temporally resolved and measured.

The achievable temporal resolution of such experiments is in the order of the FWHM of the involved light pulses. In our experiment, the target is pumped by the XUV pulses generated via HHG. It has a broad energy spectrum ($\sim 17-45$ eV) and ionizes or coherently excites several states of the studied molecules. As probe pulse, we are using the IR pulses from a SPM-broadened Ti:Sa amplifier with approximately 12 fs FWHM. State-of-the-art laser systems can also generate pulses far below 10 fs approaching the single-cycle regime [86] and even in the sub-cycle regime [87]. Therewith it is possible to produce attosecond pulses clearly below 100 as [88], such that also fast electronic processes will be accessible, as for example shown in [89].

III Experimental Setup

In this chapter the experimental techniques will be introduced that are used to perform the experiment in this work. The photoionization and different dissociation processes of the triatomic molecule nitrous oxide were studied by means of XUV-pump IR-probe measurements. The production of the required laser pulses starts in a commercially available laser system producing 32 fs laser pulses with 1 mJ pulse energy. The pulses are further compressed by a combination of self-phase modulation (SPM) hollow fiber system and chirped mirror compressor. Afterwards, 70 % of the IR energy is used to produce attosecond pulse trains (APT) with energies in the extreme ultraviolet (XUV) via high-harmonic generation (HHG), whereas the other part can be temporally shifted with respect to the APTs. Then, both pulses are superimposed collinearly and focused into the supersonic gas-target jet of the so-called reaction microscope (ReMi), with which we are able to reconstruct the initial three-dimensional momentum vectors of charged particles created in the interaction with the laser pulses on a single-event per laser shot basis.

This chapter begins with a short description of the Titanium:Sapphire (Ti:Sa) laser system, followed by the setup of the SPM hollow fiber and the chirped mirror compressor. Afterwards the design of our vacuum system will be presented with special attention given to the differential pumping between the main chamber and the ReMi, which has to be operated under ultra-high vacuum conditions. Then, the realization of the production of the high-harmonic radiation will be discussed. Finally, the design and the working principle of the ReMi will be explained as well as how the momenta of the measured particles are reconstructed.

5 The Laser System

5.1 The Titanium:Sapphire Laser

Within the scope of this work is a commercially available Titanium:Sapphire (Ti:Sa) laser system from KMLabs was used. It consists of a Ti:Sa oscillator³, which provides ultrashort femtosecond pulses with a high repetition rate (80 MHz), but low pulse energies. A second stage of the system⁴ reduces the repetition rate to 8 kHz and amplifies the pulses via the chirped-pulse amplification (CPA) technique [90]. Figure 5.1 shows an illustration of the whole setup with the detailed beam path.

Oscillator The Ti:Sa oscillator is based on Kerr-lens mode locking (see section 1.1). A frequency doubled, continuous wave (cw) Nd:YVO high-stability pump laser (5.5 W)⁵ is focused into a Ti:Sa crystal inducing lasing. The resulting laser pulses have a spectral width of ≈ 68 nm and a pulse duration of approximately 18 fs. As mentioned earlier, the repetition rate is 80 MHz and the laser has a mean output power of 680 mW corresponding to a single-pulse energy of 8.5 nJ.

Amplifier For efficient HHG, intensities of about 10^{14} to 10^{15} W/cm² have to be achieved in the experiment. For typical focusing parameters, pulses with an energy of several hundred μ J are required. Therefore, the pulses emerging from the oscillator have to be amplified by a factor of $\sim 10^5$ to 10^6 .

In the amplifier system first, a highly dispersive double-grating arrangement induces a chirp to the oscillator pulses causing an extension of the pulse duration to several picoseconds. This is necessary to stay below the damage threshold of the Ti:Sa amplifier crystal during the whole amplification process. In order to achieve the demanded increase of the pulse energy, the repetition rate has to be reduced. A Pockel's cell is used for this purpose. Every 10^4 th pulse is selected to pass the Pockel's cell leading to a new repetition rate of 8 kHz. In the next step, a Q-switched frequency-doubled Nd:YAG laser⁶ with 100 W average power, 10 mJ pulse energy, 100 ns pulse duration, and also 8 kHz repetition

³ MTS-I Femtosecond Oscillator from Kapteyn-Murnane Labs Inc., Boulder, CO 80301 USA, www.kmlabs.com

⁴ "Dragon" from Kapteyn-Murnane Labs Inc., Boulder, CO 80301 USA, www.kmlabs.com

⁵ Verdi V6, Coherent Deutschland GmbH, 64807 Dieburg, www.coherent.de

⁶ LDP-200MQG from LEE Lasers Inc., Orlando, Florida

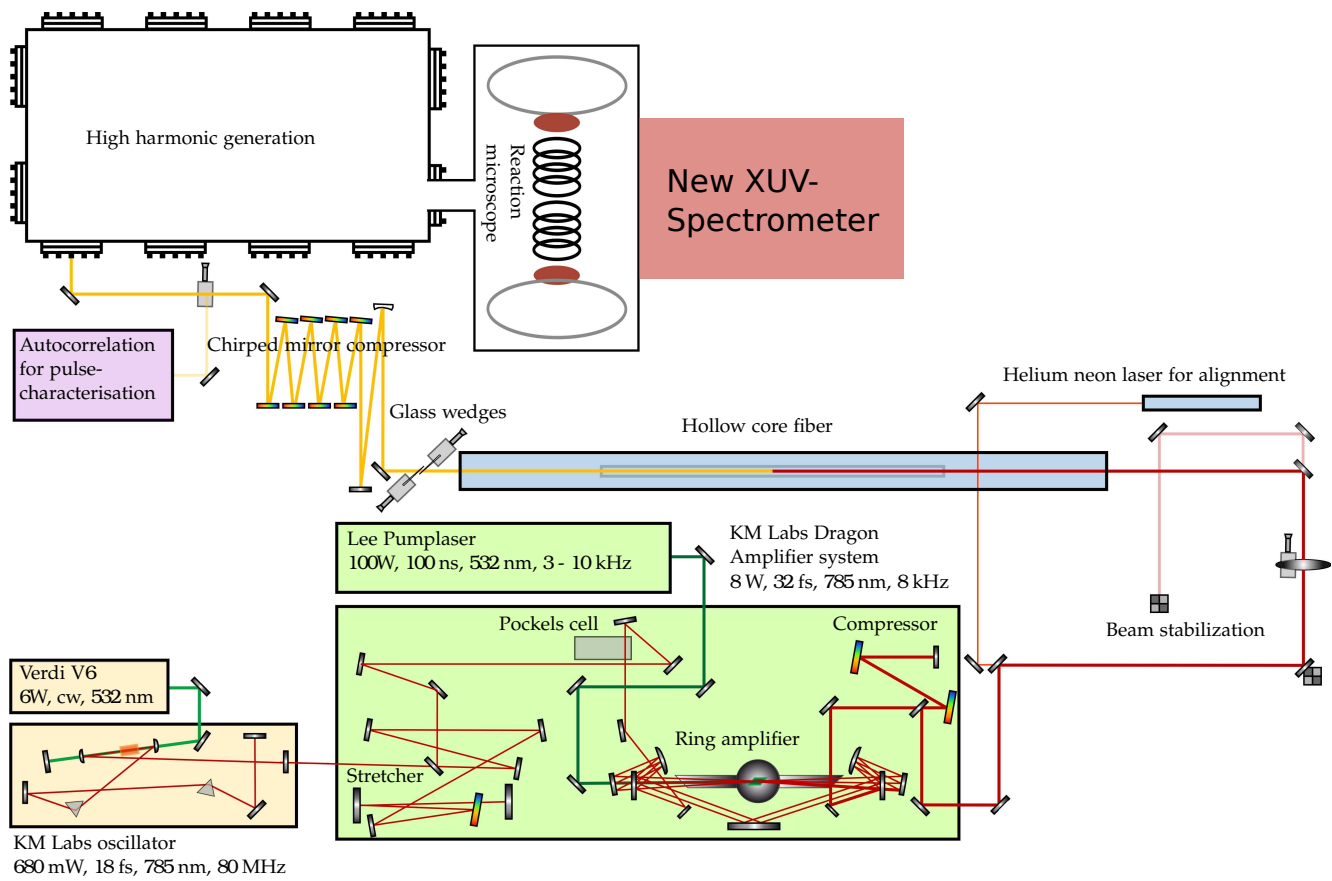


Figure 5.1: Adapted from [91]. Illustration of the femtosecond laser system.

rate, is focused simultaneously with the weak IR pulses into a cryogenically cooled Ti:Sa crystal. In this multi-pass ring amplifier, the amplified pulse passes the crystal thirteen times collecting energy every round trip. Finally, the pulses have to be re-compressed by a grating compressor (see sec. 1.2.2). The resulting Fourier limited pulses have a duration of about 32 fs and a pulse energy of 1 mJ.

5.2 Pulse Compression

Self-Phase Modulation Hollow-fiber-System In the first experiments with this setup, the pulses were used directly as they come from the laser system [12, 92]. In 2012, the setup was upgraded with a new pulse compression stage to improve the temporal resolution of the experiments [13]. The upgrade was motivated on the one hand by interesting processes in atomic or small molecular systems as electronic or vibrational transitions, which occur on timescales between 100 as and 20 fs. On the other hand, shorter pulses with the same pulse energy, have less optical cycles and higher field strengths. Therefore, HHG with such pulses lead to higher harmonic energies and shorter APTs at the same time [93]. Harmonic generation with a 30 – 35 fs pulse leads to an APT with 7 – 9 pulses, whereas a 10 fs driving laser pulse produces only 3 attosecond pulses. For the compression of the pulses, self-phase modulation (SPM, see sec. 1.2.3) is used to broaden the spectrum of the IR-pulses in a hollow-core fiber.

The laser beam is focused with a plano-convex lens ($f = 1500$ mm) into a hollow-core fiber. The fiber is ~ 1 m long, has a diameter of $250 \mu\text{m}$ and it is filled with neon. Due to the high peak intensities in the fiber, SPM occurs and leads to a broadening of the spectrum, which is dependent on the neon pressure within the fiber. Figure 5.2 shows the spectral broadening for different pressures. In the experiments presented, 3.5 bar of neon are chosen as an optimum between spectral broadening and disturbing effects induced by the high pressure, e.g. dispersion, beam fluctuations, and plasma formation.

Chirped-Mirror Compressor At the exit of the hollow-core fiber, the pulses have a spectral width of approximately 400 nm and a Fourier limit of 10 – 12 fs. They still hold between 55% and 65% of the initial pulse energy. Due to various effects, as dispersion in the entrance and exit windows (1 mm glass each) of the SPM-fiber system, and in neon, the inherent non-linear phase induced by SPM and other non-linear effects as self-steepening [41], the laser pulse has collected a significant amount of chirp. A chirped mirror setup is

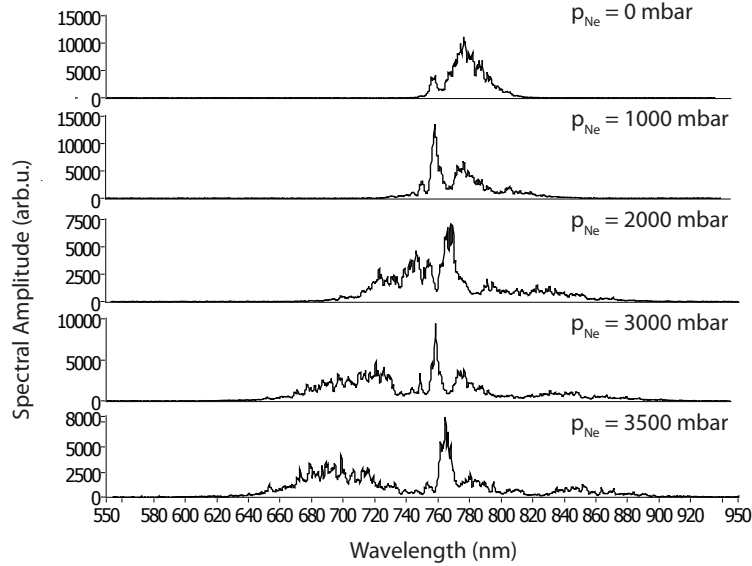


Figure 5.2: Spectral broadening of the fundamental IR laser pulses in the hollow fiber for different pressures of neon.

not only used to compensate for the second-order dispersion collected in the hollow-core fiber, it also pre-compensates subsequent dispersive elements, e.g. the entrance window of the HHG chamber (1 mm), a beam splitter (0.5 mm) and ~ 7 m propagation distance in air.

It is difficult to estimate the total amount of dispersion induced. Especially the dispersion collected within the hollow-core fiber cannot be measured in our setup and is only approximated by given values for comparable systems⁷ as $\approx 180 \text{ fs}^2$. In a commercially available system⁸, a set of six pairs of chirped mirrors is used for pulse compression. Each mirror introduces a negative second-order dispersion of $\approx -35 \cdot 1/\text{fs}^2$, corresponding to ~ 1 m air or 1 mm of glass. A picture of the currently used setup is shown in figure 5.3.

In the end, the 32 fs pulses are compressed to ~ 12 fs with 0.5 to 0.6 mJ pulse energy.

⁷ e.g. Kaleidoscope Hollow Fiber Compressor. http://www.fentolasers.com/fileadmin/documents/Leaflets/2014/04_2014/KALEIDOSCOPE.pdf

⁸ Ultra-broadband compression mirror set, Ultrafast Innovations, Am Coulombwall 1, 85748 Garching, www.ultrafast-innovations.com

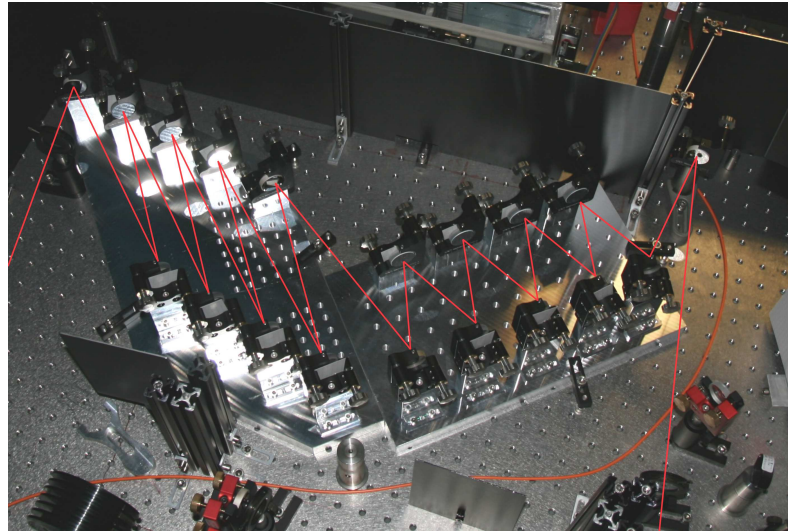


Figure 5.3: Picture of the chirped-mirror compressor. It is a combination of mirrors with two different incidence angles 5° and 19° . The self-designed support permits to use up to 7 pairs of chirped mirrors.

6 The HHG Setup & Beamline

6.1 The Vacuum System

After the re-compression of the IR pulses by the chirped mirrors, the laser beam is guided into a vacuum system for HHG, since XUV radiation is efficiently absorbed in air as well as in glass. Furthermore, the second arm of this two-color interferometer, in which the unchanged IR pulses can be delayed, is also placed in the vacuum chamber to reduce perturbations as air flows or temperature gradients. This is necessary to ensure the interferometric stability.

6.1.1 Main Chamber

The main vacuum chamber, which is depicted in figure 6.4, is a box-shaped vessel⁹ mounted on a separate support above an optical table. Both are connected with diaphragm bellows (see figure 6.5). Inside the vacuum chamber a breadboard is placed whose three posts are attached through the bellows directly to the optical table. Thus the breadboard carrying

⁹ Costum product made from PINK GmbH Vakuumentchnik, 97877 Wertheim, www.pink.de

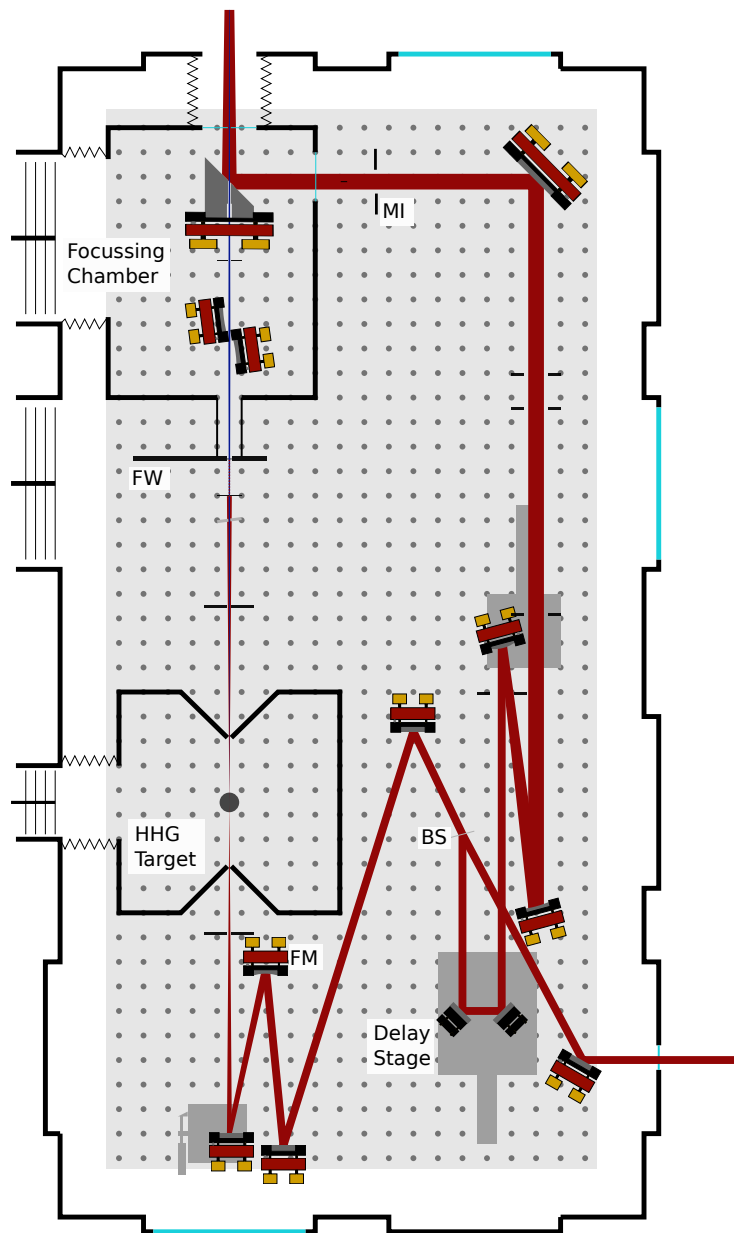


Figure 6.4: Adapted from [94]. Overview of the main chamber and the beamline. The abbreviations denote: **BS**-beam splitter, **FM**-focusing mirror, **FW**-filter wheel, **MI**-motorized iris. To give an impression for the scale of this illustration it should be noted that the grid-shaped array of grey dots represent the drill holes in the optical table, which are spaced by 25 mm.

all optical elements is not connected to the vacuum chamber and vibrations caused by the turbo-molecular pumps (TMPs) are not transferred. Besides the optical elements, two separate vessels are mounted onto the inner breadboard. One contains the HHG setup, which has to be pumped separately due to the high gas load from the HHG target. The second one serves as differential pumping stage between the main and the experimental chamber, namely the reaction microscope. Again, both inner chambers are connected via diaphragm bellows to the outer one and, thus, to the TMPs to minimize the transferred vibrations.

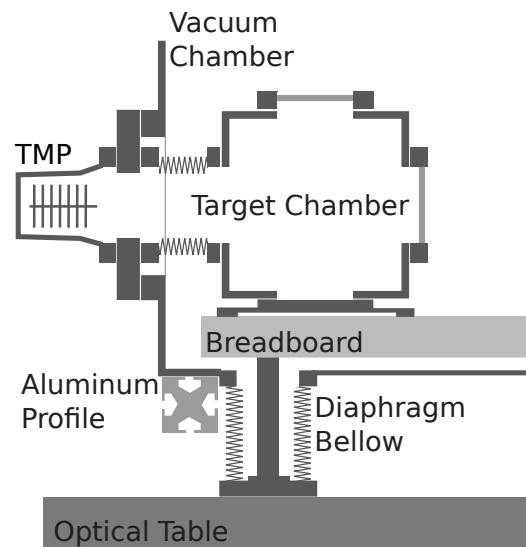


Figure 6.5: From [95]. Schematic design of the vibration isolation of the optical setup from the vacuum chamber, which is supported by aluminum profiles. The breadboard, at which all optical elements are mounted, is placed on an optical table. All connections are realized by flexible diaphragm bellows in order to minimize the transferred vibrations.

6.1.2 Differential Pumping Stage

The central experimental device, the reaction microscope (ReMi), will be explained in chapter 7. Here, it shall only be noticed that the ReMi has to be operated under ultra-high vacuum (UHV) conditions, namely 5×10^{10} to 8×10^{11} mbar. Consider the volume of the main chamber, noting that all optical elements and motorized devices are placed in it and taking into account the gas load from the HHG, it is obvious that it would be a hard task to reach the UHV regime within the entire vacuum system. In addition, the main

chamber is constructed to be quickly vented, such that adjustments of the laser beamline or changes in the experimental setup can be easily realized, thus avoiding long periods of pumping-down or baking-out times. The chamber is pumped with a 500 l/s TMP and a pressure of $\sim 3 \times 10^{-5}$ mbar can be achieved. As a result, a differential pumping stage between the HHG chamber and the ReMi is necessary.

Figure 6.6 illustrates the vacuum system¹⁰ with special attention to the differential pumping between the main chamber and the ReMi. As already mentioned, besides the HHG setup a second vessel is placed inside the main chamber, serving as first step of the differential pumping stage. In this smaller, so-called focusing chamber, which is hermetically sealed to the bigger main chamber, both beams are focused and sent collinearly into the ReMi. The XUV beam is entering through a thin metal foil and the IR beam through a low-dispersive $2 \mu\text{m}$ thin nitro-cellulose pellicle. On the ReMi side, a second nitro-cellulose pellicle with a 2 mm hole in the middle for transmission of the XUV radiation is placed to minimize the conductance value between the first and the second step of the differential pumping stage. At the first stage 1×10^{-6} mbar can be reached.

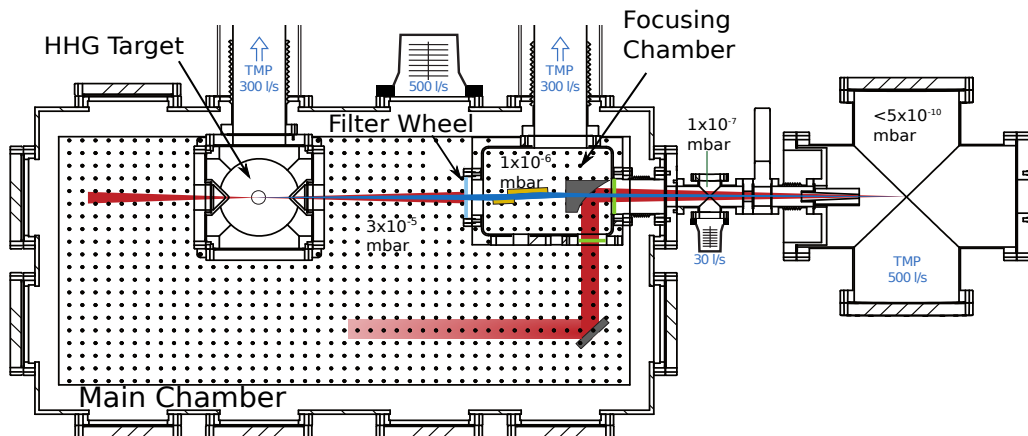


Figure 6.6: Adapted from [12]. Scheme of the main chamber including the HHG target and the focusing chamber, and the ReMi illustrating the differential pumping between both chambers. The details of the various beam paths in the vacuum system can be found in figure 6.4. Here, the grid-shaped array of black dots again represents the drill holes in the optical table, which are spaced by 25 mm.

¹⁰ In this figure the beam path is only indicated for clarity reasons. The detailed optical setup is shown in figure 6.4.

The second differential pumping stage connects the exit of the main chamber and the entrance of the ReMi. It is an independently pumped cross fitting. Here, the 30 l/s TMP attains a pressure of 1×10^{-7} . At this point, the vacuum of the ReMi can be separated with a pneumatic gate valve with a viewport. Finally, a 110 mm long conical tube section (inner diameter: 17 mm at the entrance and 7.7 mm at the exit of the tube section) serves as last barrier for the pressure between the differential pumping stage and the ReMi.

Altogether, a pressure of $< 2 \times 10^{-10}$ mbar can be achieved in the ReMi. The apertures between the different differential pumping stages and also the conical tube section are designed to hold a pressure gradient of at least one order of magnitude each. The numerical estimations on the conductance values and achievable pressures are calculated in detail in [12].

6.2 Beamline

As depicted in figure 6.4 the IR beam enters the main chamber through a 1 mm thick fused-silica window. The beam is then guided onto a beam splitter (BS), which the beam splits into the two spectrometer arms. The main part, 70%, is passing and is used to produce high harmonics, whereas the remaining 30% are reflected into a delay stage, in which the pulses can be temporal shifted with respect to the HHG pulses before they are focused into the experimental chamber.

6.2.1 HHG Beamline

In the XUV generating path, the laser beam is focused with a concave mirror ($f = 500$ mm, FM) into the HHG-target chamber. A mirror is used instead of a lens to avoid additional dispersion, but this necessitates that the focusing mirror is hit in a very acute angle to minimize the astigmatism in the focus. Figure 6.7 shows a CAD model of the HHG-target chamber. It is a cubic vessel, which is pumped directly by a 300 l/s TMP to not impair the vacuum in the main chamber ($\sim 10^{-5}$ mbar) by the gas load from the HHG target. In addition, the cube is closed on all sides except for an introversive conical entrance and exit hole ($\varnothing 2$ mm).

The HHG process takes place in a static gas target within a cylindrically shaped aluminum tube, depicted in figure 6.8. One side of the tube is connected to a gas supply outside the vacuum system, such that the cell can be filled with different gases. In the experiments presented in this work ≈ 100 mbar argon is used for HHG. The entrance

and exit openings of the tube have diameters of $200\ \mu\text{m}$ and $150\ \mu\text{m}$, respectively. The cell is suspended by a multidimensional, motorized translation stage allowing both, the adjustment of the tube to frequently needed changes in the alignment of the laser beam path and the optimization of the phase matching by adapting the position of the HHG target along the beam-propagation axis.

After HHG, the fundamental IR beam is co-propagating with the harmonic radiation. The IR light is filtered out by thin metal foils to inhibit disturbing influences of this part of the IR radiation in the experiment. These thin metal foils are mounted on a motorized filter wheel (FW). Different materials and filter thicknesses can be applied. Aluminum filters have the best transmission characteristics for harmonics produced in argon [96] as well as for the interesting energies for our experiments. They are transparent for photons between 17 eV and 72 eV (see figure 6.9). We are using thicknesses of 200 nm, 400 nm and 600 nm. Thus we are able to regulate the XUV intensities to a certain extend. In addition, a glass window can be inserted instead of the metal filters, for aligning the HHG beamline into the experiment either with an HeNe-laser, which is adjusted collinearly with the fundamental beam, or with the IR light directly. Furthermore, the filter wheel seals the vacuum of the focusing chamber against the vacuum of the main chamber, enabling a pressure gradient between both vacua and, thus, it ameliorates the differential pumping

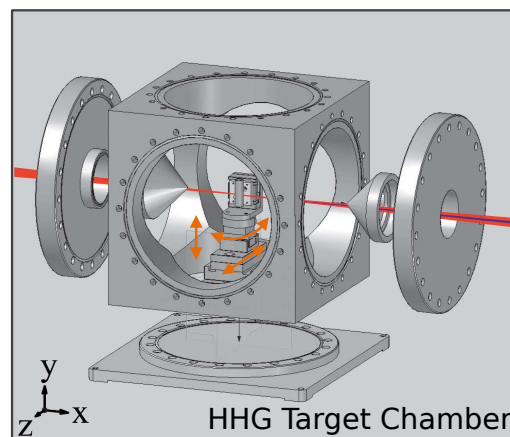


Figure 6.7: From [13]. CAD model of the HHG target chamber. The laser is focused into a small tube filled with rare gas. The target tube is mounted on a motorized stage in order to align the tube and improve the phase matching.

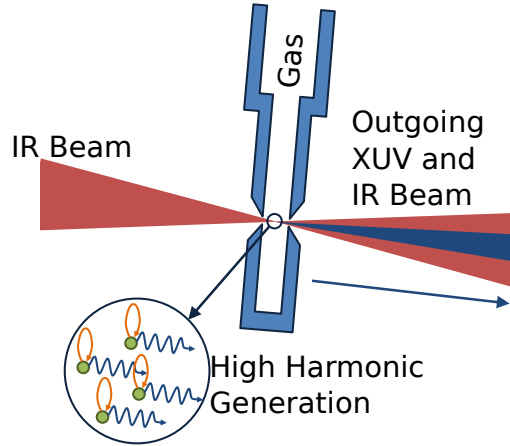


Figure 6.8: From [13]. Scheme of the target tube, in which the HHG process occurs. It is filled with a rare gas at a constant pressure (50 – 200 mbar).

between the main chamber and the ReMi.

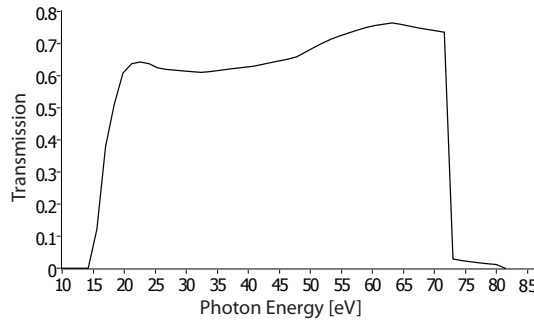


Figure 6.9: Transmission profile of a 200 nm thick Al foil. Data taken from [97].

Finally, the XUV beam is focused with a modified Kirkpatrick-Baez configuration into the target of the ReMi. In the original Kirkpatrick-Baez setup two spherical mirrors are used whose substrates are perpendicular to each other [98, 99]. In our modified version the second perpendicular spherical mirror is replaced by a parallel cylindrical mirror in order to achieve vertical and horizontal focusing of the XUV beam at the same spot. We are using a spherical mirror with a radius of curvature (ROC) of 5000 mm and a cylindrical mirror with an ROC of 60 mm. Both mirrors are coated with a thin gold layer and are hit under 6° grazing incidence in order to achieve a reflectivity up to 80% at photon energies

between 30 eV and 50 eV. With the high reflectivity we can expect up to 10^6 to 10^7 XUV photons per laser shot within the target volume in the ReMi [12].

6.2.2 IR Beamline

The part of the laser beam reflected from the beam splitter is used as probe pulse in the two-color pump-probe measurements. The pulses are guided into a delay stage, a retro-reflector, mounted on a piezo-driven delay stage¹¹, which allows delays up to 10 picoseconds. The whole delay-stage setup is embedded in a manual linear translation stage, enabling the rough adjustment of the temporal overlap between the pulses in both interferometer arms, when the main chamber is vented. The diameter of the beam is increased to approximately 25 mm to diminish both, the focal size in the experimental target as well as power losses due to the drilled hole in the IR-focusing mirror, through which the XUV beam passes into the ReMi. A motorized iris (MI) can be used for the spacial alignment of the IR path and to control its intensity. Afterwards, the IR beam is guided through a nitro-cellulose pellicle into the focusing chamber where it is deflected by 90° and simultaneously focused with an off-axis parabolic-mirror of 600 mm focal length. As already mentioned, a 3 mm hole is drilled through the center of the parabolic mirror, to let the XUV beam pass, such that both pulses propagate collinearly and are focused into the interaction volume of the ReMi.

6.3 Characterization of the High Harmonics

High harmonic radiation shall be used in the present experiments to excite electronic transitions. For the understanding of the results it is mandatory to know the photon energies, with which the target atoms or molecules are pumped. Therefore, an XUV spectrometer was installed at one side of the main chamber [12, 95]. In addition, this tool can also be used to optimize the HHG before entering the reaction microscope. Figure 6.10 gives an overview of the main chamber including the spectrometer beam path.

A flip mirror can be inserted between the HHG setup and the focusing chamber, guiding the beam towards the spectrometer. The XUV light passes two spherical gold mirrors, with $ROC_1 = 1500$ mm and $ROC_2 = 3000$ mm. They focus the XUV radiation through a

¹¹ PI Physik Instrumente, P-629.1CL PI Hera Flexure-Guided nano positioning Piezo Stage, 1500 μm with capacitive feedback.

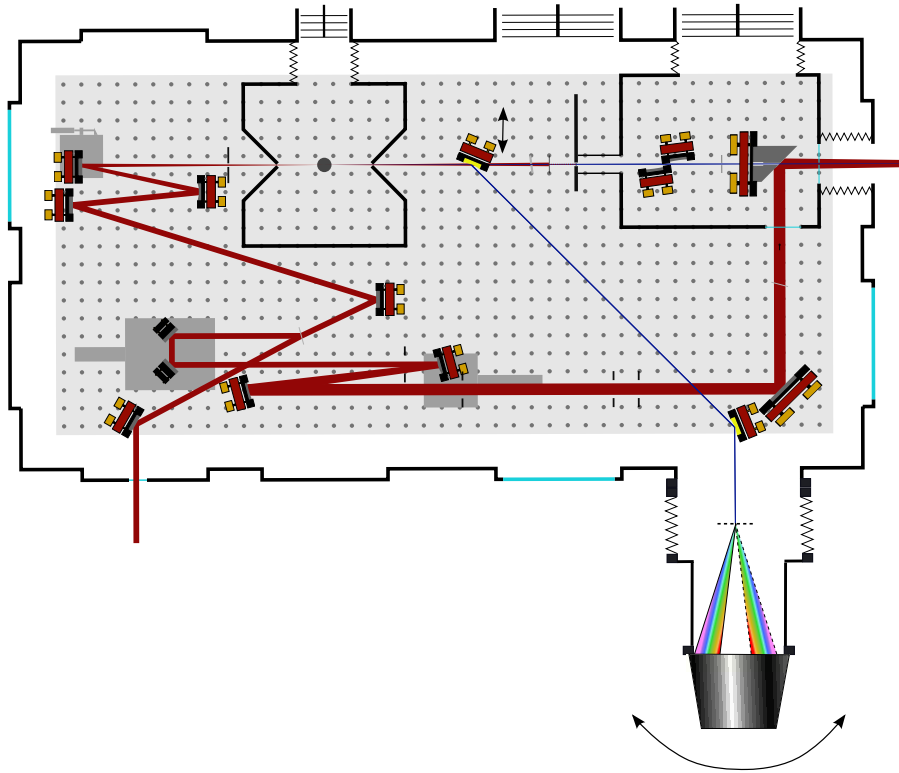


Figure 6.10: Adapted from [94]. The main chamber including the beam path to the spectrometer at the side of the vessel. A mirror has to be inserted into the beam path guiding the XUV beam into the spectrometer.

free-standing Si_3N_4 transmission grating on a cooled XUV CCD-camera¹². The grating has a lattice spacing of $g = 100$ nm. To reduce stray light from the fundamental IR radiation, an 800 nm thick aluminum foil is placed into the beam path.

The camera only detects an extract of the XUV spectrum. For a complete spectrum, several pictures taken for different diffraction angles have to be merged. The camera can be moved on a circle around the grating and it can be fixed at defined positions. The resulting spectra are calibrated by knowing the spectrometer geometry, using the fact that the harmonic energies are equally spaced, and using the transmission profile of the inserted aluminum filters. A different beam alignment can lead to a modified spectrometer geometry and considerable shifts of the diffraction angles. Therefore, an exact, permanent

¹² Pixis-XO, Princeton Instruments Inc., Trenton, NJ 08619, USA, www.princetoninstruments.com

energy calibration is not realizable.

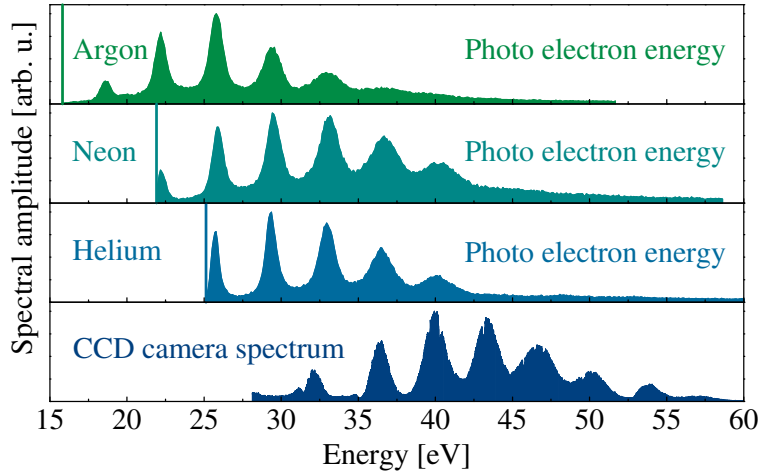


Figure 6.11: From [13]. Three photoelectron spectra for single ionization of different target gases (argon, neon, and helium) measured in the ReMi. The vertical lines indicate the respective ionization potential. The fourth spectrum was measured with the XUV spectrometer.

The XUV spectra can also be compared with the photoelectron spectra measured in the ReMi, in which the harmonic spectrum is also encoded. The resulting spectrum does not represent the exact intensities of the harmonics, since the ionization process strongly depends on the energy-dependent ionization cross-sections. Furthermore, single harmonic peaks could be enhanced through atomic, or molecular resonances. Figure 6.11 shows different XUV spectra measured by both techniques. The first three graphs show photoelectron energy-spectra measured in the ReMi for single photoionization of different target gases (Argon, Neon and Helium). The different ionization thresholds for the various gases show themselves as thresholds for the low-energy electrons increasing from Ar to He (lines in figure 6.11). The bottom graph depicts the spectrum measured in the XUV spectrometer. Particularly noticeable is that here more high-energy photons are visible, whereas the low-energy part is missing. This can be explained by the combination of several effects. The quantum efficiency of the CCD chip drops by a factor of 3 going from 25 eV to 15 eV. Moreover, the diffraction efficiency of the transmission grating is low for energies below 30 eV ($< 9\%$ [100]) and so is the grazing incidence reflectivity of the gold coated mirror ($< 20\%$ [100]). The intensity drop in the high-energy regime in the XUV spectrum corresponds to the cut-off energy in argon at the estimated laser intensity and

in addition it coincides with the Cooper minimum of argon [101].

The implementation of the XUV spectrometer shown in this section was described in [12, 95]. Some disadvantages of this device led to the idea to build an improved version of the spectrometer, which observes the outgoing XUV radiation from the ReMi. The design, the installation, and the initial operation was an essential part of my work. Chapter IV presents the second XUV spectrometer in detail and shows first XUV spectra.

7 Reaction Microscope

The experiments carried out within the scope of this work were performed in a so-called reaction microscope (ReMi). It combines the cold target recoil-ion momentum spectrometer (COLTRIMS) technology with an electron spectrometer allowing the simultaneous measurement of positively and negatively charged fragments. Since the first description [102], this technology has found its way into many different applications [3]. Originally, the ReMi was build to study ion collisions with atoms or molecules. Here, we are focusing a laser beam into a cold, collimated supersonic gas jet. The light is interacting with the target atoms or molecules in the gas jet. They are ionized, and accordingly molecules can even dissociate. The charged particles are then projected by a weak electric and magnetic field onto time and position sensitive detectors. With these information, a full three-dimensional momentum vector can be calculated for every particle. Furthermore, multiple particles can be measured in coincidence allowing to distinguish between different reaction channels.

7.1 Design

The design and the setup of the ReMi, which was used to carry out the experiments presented in this work, is described in detail in [92]. The main ReMi components are depicted in figure 7.12. The given coordinate system will be used throughout this work. The laser propagation direction defines the x -axis, the supersonic gas jet propagates along the negative y -axis and the spectrometer axis is oriented along the z -axis.

7.1.1 Target

Performing high-resolution momentum spectroscopy requires well-defined momenta of the initial particles. In order to have a target for our experiments with a low thermal momentum, it is cooled via supersonic expansion. Gas at a high pressure (~ 3 bar) expands through a thin nozzle ($\varnothing \approx 30 \mu\text{m}$) into a vacuum. The gas expands adiabatically and the entropy remains unchanged, which leads to a cooling of the gas with decreasing pressure. The velocity of the expanding gas exceeds the speed of sound and the so-called “zone of silence” is formed (see 7.13). Considering an ideal case for the calculation of the expansion velocity, at which the total thermodynamical potential, or enthalpy, is transformed into

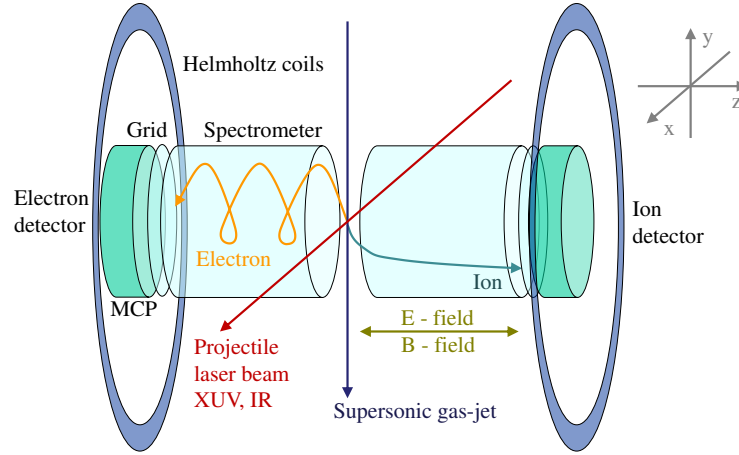


Figure 7.12: From [13]. Schematic design of the reaction microscope. The laser beam (red) ionizes a target particle in the supersonic target jet (blue). The created charged fragments are driven by an electric field, which is produced by a series of spectrometer plates (light green), towards time- and position-sensitive detectors (dark green). Coaxial Helmholtz coils (light blue) generate a magnetic field to induce a gyromotion of the electrons.

kinetic energy. The enthalpy H is defined as [103]

$$H = U + pV = \frac{5}{2}Nk_B T_0, \quad (7.1)$$

with U the internal (thermal) energy of the system, p and V pressure and volume of the considered gas, N the number of particles, k_B the Boltzmann constant, and T_0 the temperature of the gas before expansion. The velocity v of a single target atom with mass M can then be calculated with

$$v = \sqrt{\frac{5k_B T_0}{M}}. \quad (7.2)$$

Considering nitrous oxide as target gas, which has a mass of 7.31×10^{-26} kg, at room temperature (294.15 K), the particles of the jet expand with 527.1 m/s, whereas the speed of sound of nitrous oxide (approximated as ideal gas) is $c_{N_2O} = \sqrt{\kappa \frac{RT}{M N_A}} \leq 268.8$ m/s, with $\kappa \leq 1.3$ the adiabatic index, R the gas constant and N_A the Avogadro constant.

Two skimmers with small apertures (200 and 400 μm) cut out only a small fraction of

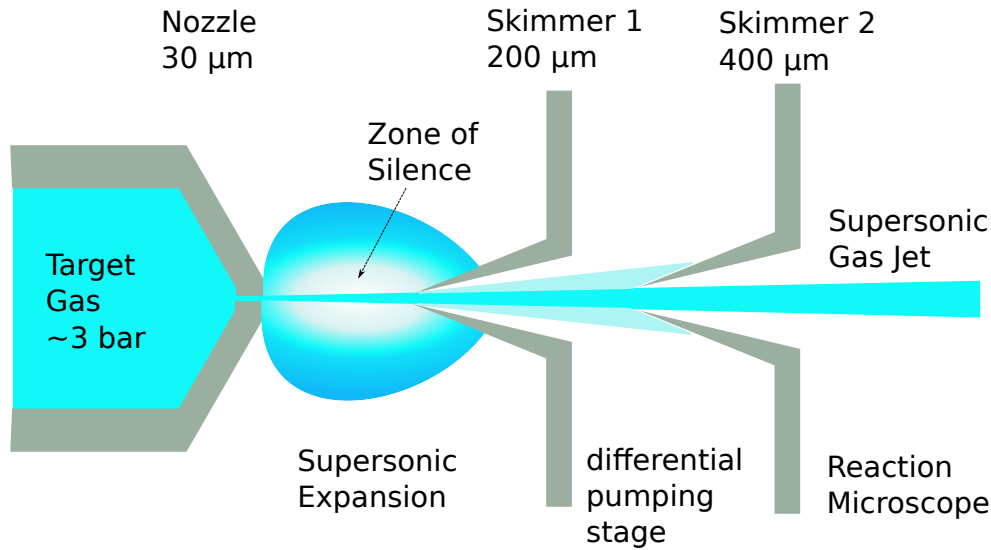


Figure 7.13: Adapted from [92]. Creation of the supersonic target jet. Gas is expanding through a nozzle. In doing so, the gas exceeds the local speed of sound, which is due to the high pressure gradient and the so-called zone of silence is formed. A set of two skimmers extracts the low spread-momentum particles of the gas jet.

the gas jet and, thus, they limit the maximal transversal momentum of the jet particles in x - and z -directions. In the experiment we can achieve target temperatures T_{jet} below 1 K, resulting in $\Delta p_{therm,x} \approx \Delta p_{therm,z} \approx 0.14$ a.u. for nitrous oxide [92, 104]. Since the jet cannot be collimated in propagation direction, $\Delta p_{therm,y}$ is determined by the energy spread in propagation direction $\Delta E_{therm} = k_B T_{jet} \approx 0.13$ meV, which transforms to $\Delta p_{therm,y} \approx 0.89$ a.u.. An illustration of the gas-jet setup is shown in figure 7.13.

7.1.2 Spectrometer

The spectrometer is the centerpiece of the ReMi. Its schematic design is illustrated in figure 7.14. The target atoms or molecules in the gas jet are ionized by a laser pulse. The charged fragments are then driven by a homogeneous electric field towards the detection system. The electric field is generated via 32 ring-shaped plates (1 mm thick), which are connected with suitable resistances (180 k Ω). The plates are equally spaced by 7 mm to achieve a constant voltage drop. The last spectrometer plate is followed after 10 mm by a ring with a width of 12 mm and an inner diameter of 110 mm. It has a bias voltage and

shields the electric field from field lines coming from the vacuum-chamber walls, which are on ground potential [105].

In some ReMis, the spectrometer is followed by a field-free drift region with the double length of the acceleration distance. In this case, the TOF becomes independent on the position in the target, at which the particles starts their propagation towards the detectors. This effect is called time focusing and it is necessary, if the interaction volume is considerably large. In the presented experiment, the interaction volume is well defined by the focal size of the laser beams ($\approx 30 \mu\text{m}$), such that here no drift region is implemented, which simplifies the reconstruction of the momenta (presented in section 7.2).

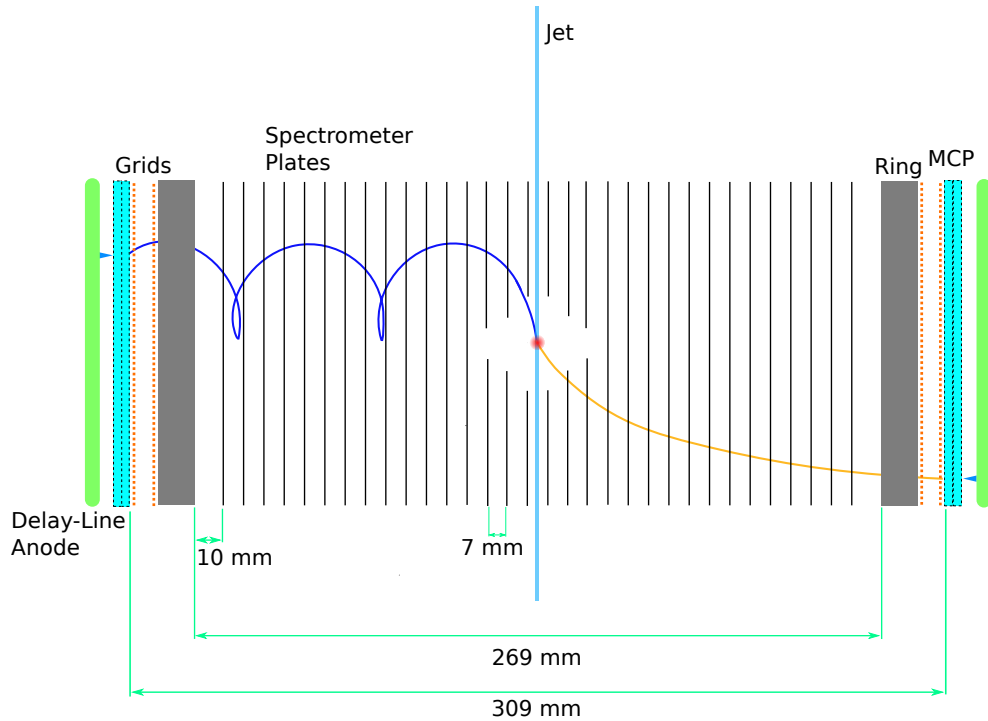


Figure 7.14: Illustration of the spectrometer section of the ReMi including the detection system consisting of multi-channel plates (turquoise) and delay-line anodes (green). The 32 ring shaped anodes (black solid lines) are spaced by 7 mm. Around the target area, the plates are cut into two halves, in order to let the laser pass. The respective halves are connected via Kapton-insulated wires. A ring (gray) completes the spectrometer, which is then closed with two grids (orange dotted line). In addition, a showcase event is depicted: the laser (red) ionizes a particle in the target jet (light blue), the freed electron is accelerated towards the left-hand side detector (blue trajectory) and the ion is driven towards the right-hand side (peach-colored trajectory).

For most experiments, the voltage at the end of the spectrometer does not exceed ± 400 V, whereas the detectors are operated at $2 - 3$ kV. Therefore, the spectrometer has to be insulated from the high-potential area, due to possibly induced field inhomogeneities at the ends of the spectrometer. These would cause a deflection of the charged particles and, thus, distort the experimental results. In order to avoid this effect, the spectrometer is closed at both ends with two fine-meshed copper grids (mesh size: $224 \mu\text{m}$, wire diameter: $30 \mu\text{m}$), which have a transmission of 85 %. The first grid is placed directly behind the ring, at a slightly higher potential. The second one is placed at a distance of 8 mm relative to the first one and close to the detector surface. It is on a potential between the first grid and the detector.

An additional magnetic field, which is parallel to the electric field, is applied in the ReMi, which induces a cyclotron motion of the charged fragments¹³. The magnetic field is produced by a slightly modified Helmholtz configuration consisting of two coils with a diameter of 750 mm that have a distance of 450 mm. Each coil has nine windings and they generate a homogeneous B-field throughout the spectrometer. The magnetic flux density applied in the ReMi is $B = 7.88$ Gauss. The coils are slightly tilted with respect to the spectrometer axis in order to compensate the geomagnetic field ($B_{geo} \approx 0.03$ to 0.06 Gauss).

7.1.3 Detectors

Multi-Channel Plates The detection systems for electrons and ions each consists of a stack of two micro-channel plates (MCPs) and a crossed pair of delay-line anodes (see figure 7.15(a)). The MCPs are 1.5 mm thick glass plates with a diameter of 80 mm, interspersed with small channels with a diameter of $25 \mu\text{m}$, which are spaced by $32 \mu\text{m}$, and which have a bias angle of $8^\circ \pm 1^\circ$. Their working principle is similar to a photo-multiplier. A voltage is applied between the front and the back side of the MCP-detector (~ 1000 V per MCP). An impacting charged particle initializes a cascade of secondary electrons, as depicted in figure 7.15(b). Thus, one MCP can amplify the signal by a factor of approximately 10^5 . In order to have sufficient amplification and, thus, to be sensitive on single particles, a stack of two MCPs is used. The generated electron cloud is then accelerated towards the

¹³ Due to the high mass, the magnetic field can be neglected for the ion motion. Only the electrons are considerably affected.

delay-line anodes, with which the hit position is measured. In addition, the cascade of electrons induces a drop of the voltage. This signal can be read out and used to calculate the time-of-flight of the particles. The temporal resolution of the system is in the order of 1 ns [106].

Delay-Line Anode For the determination of the point of impact, the electron cloud is hitting a crossed pair of delay-line anode (DLA) each consisting of two isolated copper wires spaced by 0.5 mm. Two wires are wound horizontally and the other two vertically as depicted in figure 7.16 (a). The wire pairs consist of a reference and a signal wire (see figure 7.15(b)) forming a so-called Lecher system. Both are on positive potential with respect to the rear side of the MCP. Usually, the signal wire is at 200 V, which is approximately 50 V above the potential of the reference wire, such that the most electrons emitted from the channel plates are collected by the higher-charged wires. Then, the charge propagates as a signal along the two wires towards both ends of each lecher conductor. The arrival times are measured and the difference between both is proportional to the impact coordinate perpendicular to the winding direction of the wire. The working principle of a single delay

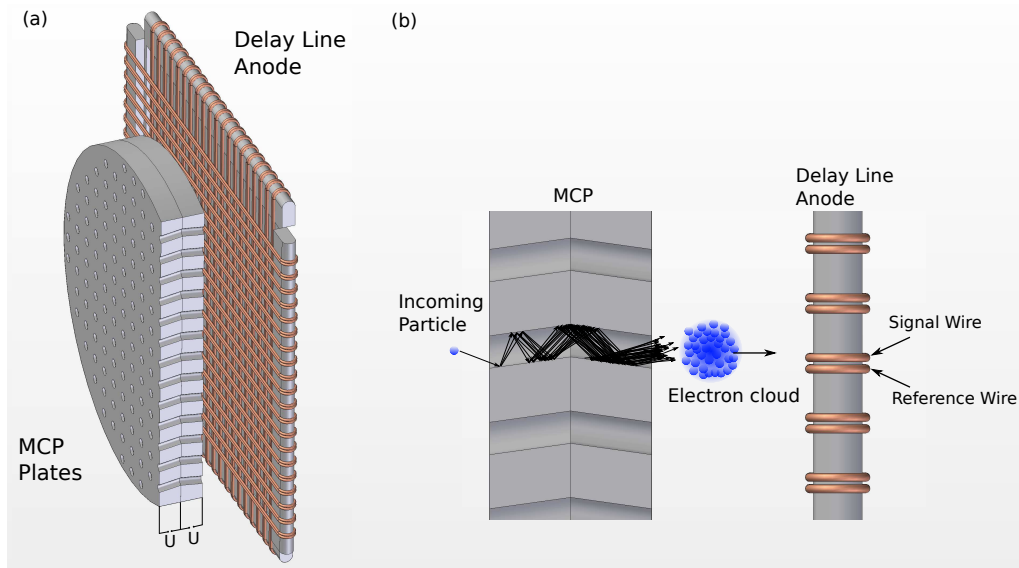


Figure 7.15: (a) Schematic of the ReMi detection system consisting of an MCP detector for the measurement of the time-of-flight and a delay-line anode for the position read-out. (b) A zoomed view from (a) to illustrate the working principle of the MCPs.

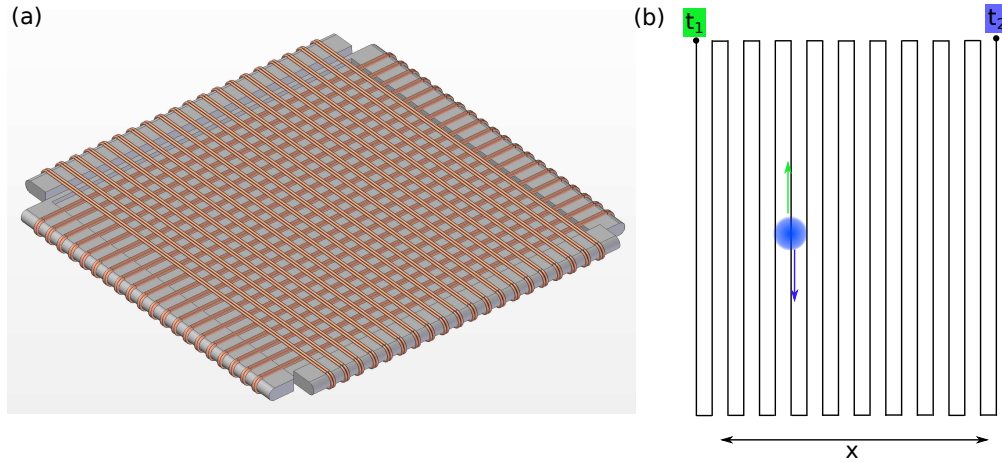


Figure 7.16: (a) Simplified CAD drawing of the delay-line anode (DLA) consisting of a crossed pair of wires in order to measure the 2-D hit position. Each wire pair consists of a reference and a signal wire. (b) Working principle of a DLA for the hit position in x -direction. An electron cloud hits the wire and the deposited charge propagates towards both ends of the line. The arrival-time difference ($t_1 - t_2$) is proportional to the x -position.

line is depicted in figure 7.16 (b). With two perpendicular delay-line anodes, the 2-D impact position can be determined.

The Lecher system is used on the one hand, to improve the transmission of the signal. The wires are unshielded in order that the electrons have direct access to the conductor. However, the signal of a single unshielded filament is distinctly damped by radiant exitance and can be superimposed by external, high-frequent noise fields. By applying the reference wire, the radiant-exitance field spans in between the both filaments, which reduces the damping as well as external influences [107]. In addition, the propagation velocity of the signal is reduced, which simplifies the time measurement. On the other hand, since the reference wire carries no considerable signal from the impacting electrons, the signal-to-noise ratio can be improved by subtracting the reference from the signal.

The spatial resolution of the DLA is mainly determined through the spacing between the single windings of the delay line. In our setup it is 0.5 mm [106]. However, the electron cloud may extend over several windings and additionally the signal strength is fluctuating between the single events. Therefore, the signals are processed by constant-fraction-discriminators, which determines the center of a pulse independent from its amplitude [108]. As a result, the center of the electron cloud, which ranges over several windings,

can be identified even if it is in between two wires, such that the effective resolution can be better than the wire spacing [108]. The electronic processing of the measured signals and further technical details of the detection and data acquisition is described in [92].

7.2 Calculation of Momenta

This section introduces the reconstruction of the three-dimensional momentum from the TOF and the impact position of the particle on the detector. It is based on the equations of motion of a charged particle in electric and magnetic fields. It is assumed that the initial momentum components in x - and z -direction of the target fragments before ionization are negligible. Under these conditions, the sum over the momenta of all fragments originated in one reaction has to vanish and, thus, different reaction channels are distinguishable. In addition, the TOF of the ions can be used to determine the measured ion species, since it depends on the charge-to-mass ratio. Also, the ion momentum parallel to the spectrometer axis, namely p_z , can be reconstructed via the TOF, whereas p_x and p_y are encoded in their impact position on the detector. In contrast to the ions, the motion of the electron in the electric and magnetic field is more complicated leading to more complex spatial spectra. In addition, electrons originating from different ion species can not be distinguished. Therefore, it is necessary to correlate electrons to certain ion species via coincident detection.

7.2.1 Ion Momentum

The three-dimensional momentum vector can be expressed in cylindrical coordinates, since the spectrometer axis is parallel to the direction of the electric and magnetic fields, with one momentum component p_z parallel to the spectrometer axis, one perpendicular to it $|\mathbf{p}_r| = \sqrt{p_x^2 + p_y^2}$ and the azimuthal angle $\phi = \arctan \frac{x}{y}$. The longitudinal ion momentum p_z can be calculated from the TOF t_i , which depends on the charge-to-mass ration q/m and the initial velocity of the ions in z -direction $v_{i,z}$ after ionization or dissociation. The resulting equation of motion is given by [13]

$$l = v_{i,z}t_i + \frac{1}{2}at_i^2, \quad (7.3)$$

with $a = \frac{qU}{ml}$ the acceleration of a charged particle with the extraction voltage U over the acceleration length l . The longitudinal momentum can then be expressed by

$$p_z = m \frac{l}{t_i} - \frac{1}{2} qU \frac{t_i}{l}. \quad (7.4)$$

The transversal ion momentum can be determined by the impact position on the detector. The distribution of the ions is shifted in propagation direction of the gas jet, due to the jet velocity of the target particles. The center of the ion distribution is defined as (x_{i0}, y_{i0}) . The hit position can then be written as $|\mathbf{r}_i| = \sqrt{(x_i - x_{i0})^2 + (y_i - y_{i0})^2}$ and the respective ion velocity is given by $v_{i,r} = \frac{|\mathbf{r}_i|}{t_i}$. Then, the transversal ion momentum \mathbf{p}_r can be written as

$$\mathbf{p}_r = \frac{\mathbf{r}_i m}{t_i}, \text{ or} \quad (7.5)$$

$$p_x = \frac{(x_i - x_{i0})m}{t_i}, \text{ and } p_y = \frac{(y_i - y_{i0})m}{t_i}. \quad (7.6)$$

In the calculation of the ion momentum, the B-field can be neglected due to its weak influence. Both momentum components can be used to reconstruct the azimuthal angle ϕ ($\cos(\phi) = \frac{p_x}{|\mathbf{r}_i|}$ and $\sin(\phi) = \frac{p_y}{|\mathbf{r}_i|}$) and even the orientation of the (linear) molecule [104].

7.2.2 Electron Momentum

The longitudinal momentum of the electrons can be calculated analogously to the longitudinal ion momentum by means of equation (7.4). In contrast, the transversal momentum is encoded in the gyroradius r_c of the electrons. The applied electric and magnetic field causes a Lorentz force, which forces the electrons to move on spiral trajectories. The radius of the cyclotron motion depends on the magnetic field strength B , the charge e of the electron and its transverse momentum $\mathbf{p}_{e,r}$:

$$r_c = \frac{\mathbf{p}_{e,r}}{eB}. \quad (7.7)$$

The gyroradius is not directly accessible, but it can be extracted from the hit position and time of the electron on the detector. Figure 7.17 illustrates the cyclotron trajectory of the electron projected onto the detector plane and all corresponding quantities. An electron is emitted with the transversal momentum $\mathbf{p}_{e,r}$ and an azimuthal emission angle

ϕ . It is moving on a circular trajectory with the radius r_c and at the detection time its trajectory covers an angle α on the circle, which depends on the cyclotron resonance ω_c and the TOF of the electron t_e

$$\alpha + \omega_c t_e = \frac{eB}{m_e} t_e, \quad (7.8)$$

with m_e the electron mass. The hit position R can be interpreted as chord of a segment of the circle, at which the electron is moving, and trigonometric considerations yield in [104]

$$|\sin(\frac{\alpha}{2})| + \frac{R}{2r_c}. \quad (7.9)$$

Equation (7.7) can be inserted in equation (7.9) to obtain the transversal momentum

$$p_{e,r} = \frac{ReB}{2|\sin(\frac{1}{2}\omega_c t_e)|}. \quad (7.10)$$

The azimuthal emission angle is $\phi = \phi_{Detector} - \frac{1}{2}\omega_c t_e$.

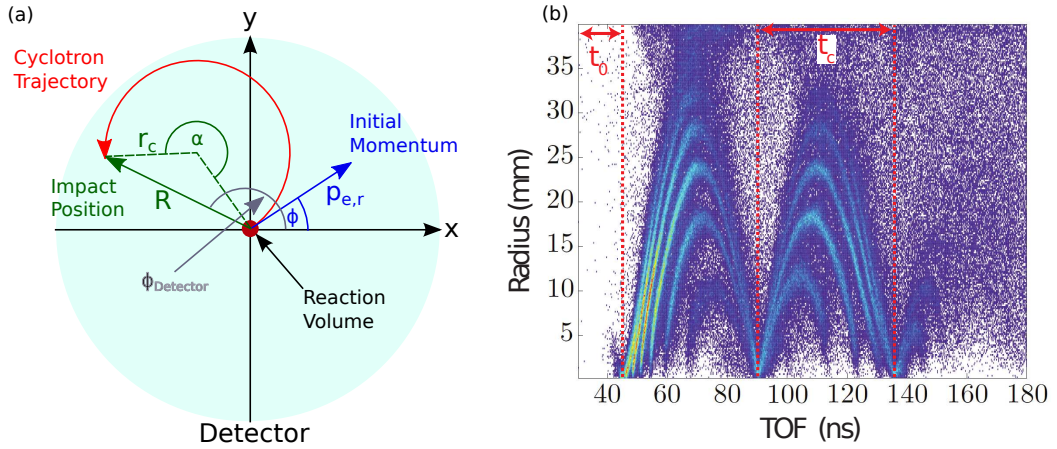


Figure 7.17: Adapted from [13, 91]. (a) Illustration of the reconstruction of the transversal electron momentum $p_{e,r}$ emitted under the azimuthal angle ϕ . Shown is the cyclotron trajectory of the electron, with the radius r_c , projected onto the detector plane as well as the impact position R . (b) Radial position as function of the TOF of the electrons, which provides the period time of the cyclotron motion t_c by analysis of the periodic structure, as well as the offset time t_0 .

After every full period of the cyclotron motion, all electrons, regardless of which energy, are passing again their origin, regarding the projection onto the detector plane. This leads

to a loss of the resolution for the transversal momentum for electrons detected after an integer number of periods, which means for electrons with TOF $t_e = n \cdot \frac{2\pi}{\omega_C}$. The TOF is defined by the extraction voltage and the longitudinal momentum, thus, the knot-position can be adapted by changing the extraction voltage.

7.2.3 Calibration

For a reliable analysis of the experimental data it is necessary to determine the free parameters used in the reconstruction of the momenta. The homogeneity of the electric field within the spectrometer was verified during the buildup of the ReMi, which is described in detail in [92]. The electric field is then determined by the applied acceleration voltage U ($= 250$ V in the experiment presented in chapter V) and the acceleration length l , which is known from the design drawings ($l = 154.5$ mm). The parameters x_{i0} and y_{i0} are obtained by the barycenter of the ion position spectra.

The time period of the cyclotron motion t_c of the electrons can be found by plotting the radial position of the electron as a function of the electron TOF, which is depicted in figure 7.17(b). As described earlier, after an integer number of periods, all electrons return to the spectrometer axis and appear as nodes in the spectrum at $r = 0$. As a result, the time difference between two nodes represents t_c , from which the magnetic field B can be calculated as

$$B = \frac{2\pi m_e}{t_c e}. \quad (7.11)$$

Finally, the time offset between the recorded ionization and the laser triggering signal has to be identified, which corresponds to the absolute time zero t_0 . It can be found by extrapolating the node positions towards earlier times. Then, the time difference between $t_e = 0$ and the extrapolated first node depicts the absolute time zero t_0 .

The acceleration voltage U and length l are estimated only by the applied voltage and the known spectrometer geometry, which may be not precise enough for the exact reconstruction of the momenta. At first, the longitudinal momenta of all measured ion species are reconstructed from the TOF spectrum (see figure 11.2) as described in section 7.2. Then, the extraction voltage and the time offset can be adapted, such that the longitudinal momenta of all ion species are centered around $p_z = 0$ a.u., as it is shown on the example of N_2O^+ in figure 7.18(a). In addition, it is possible to use the fact that the momentum transferred during the interaction of the photons to the target particles is

negligible, such that the obtained momenta has to balance each other. In the analysis, the sum of the longitudinal momenta of one electron $p_{e,z}$ and one ion $p_{i,z}$, both originated from the single ionization of the target particles and measured coincidentally, is observed and the respective parameters are fined-tuned, such that the momentum sum fulfills the condition $p_{e,z} + p_{i,z} = 0$, as it is shown in figure 7.18(b).

In addition, photoelectron-energy spectra are often used in the analysis to extract valuable information. Therefore, it is important to improve the calibration of the electron energies. Usually a short-time reference measurement is performed using argon as target gas in the ReMi before starting the intended measurement. In the single ionization of argon the state accessed with an XUV photon in the energy regime of 17 – 45 eV has an ionization potential of $I_p = 15.76$ eV. The respective photoelectron-energy spectrum carries the clear peak structure of the harmonic radiation. On the one hand, this distinct signal is used to improve the setting of the parameters mentioned above by plotting the photoelectron energies as function of the respective momenta in all three dimensions. On the other hand, it is possible to perform a reliable energy calibration. Considering two different peaks of the spectrum at the energies E_1 and E_2 , from which E_1 is the first energy peak observed in the spectrum. This peak will come from the photon of the lowest harmonic order n_1 , which exceeds the ionization potential I_p . Then, the energy position of the first peak and the spacing between both peaks have to fulfill the equations

$$\Delta E_{\text{HH}} = \frac{2}{n_1}(I_p + E_1) \quad (7.12)$$

$$\Delta E_{\text{HH}} = \frac{E_2 - E_1}{n_2 - n_1}, \quad (7.13)$$

with ΔE_{HH} being the high-harmonic spacing of $2\hbar\omega_0$, which is known from the IR spectrum taken at the exit of the SPM hollow fiber. In reference [13] it was shown that it is possible to determine the photoelectron energies up to an accuracy of 0.1 eV but anyhow much better than the spacing between two neighboring harmonics.

Figure 7.18 depicts several important graphs of the calibration procedure for the experiment presented in chapter V as examples for the properly adjusted parameters in the analysis. The momentum distributions of all ion species are centered around $p_z = 0$ a.u. as depicted in figure 7.18(a) for N_2O^+ as well as the respective sums of electron and ion momenta (compare figure 7.18(b)). The detectors are scaled to their perfect circular

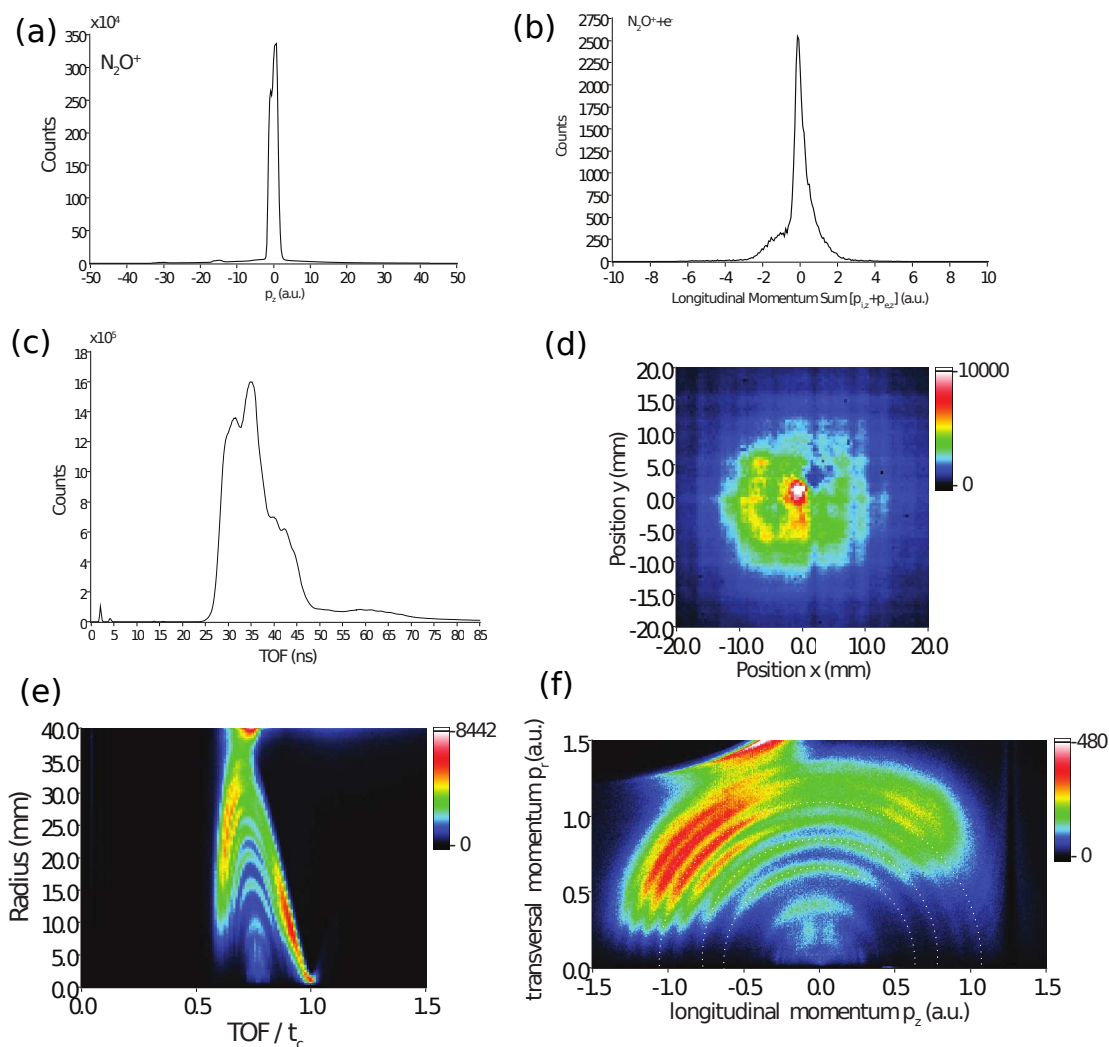


Figure 7.18: Several pictures from the adjustment of the parameters for the analysis of the measurement shown in chapter V necessary for the calibration of the ReMi spectrometer. (a) The longitudinal momentum of N_2O^+ . (b) The sum of electron and ion momentum for $N_2O^+ + e^-$. (c) The TOF spectrum of all electrons measured during the experiment. (d) Spatial distribution obtained on the electron detector. (e) Radial position as function of the TOF of the electrons. (f) Transversal electron momentum as function of the longitudinal electron momentum for $N_2O^+ + e^-$.

shape and their radius $R = 40$ mm and are then centered. As example a zoomed picture of the spatial distribution on the electron detector is shown in figure 7.18(d). The radial position of the electron as a function of the electron TOF is shown in figure 7.18(e). Due to the high extraction voltage ($U = 250$ V), only t_0 can be obtained, whereas the period of the cyclotron motion t_c and therewith the B-field is not directly accessible. However, the magnetic field is permanently applied without switching on and off the highly stable power supply. Therefore, the value is known from previous experiments carried out at lower extraction voltages, at which the electrons perform several periods of the cyclotron motion. Nevertheless, a wrong B-field value would cause distortions in several graphs as for example in figure 7.18(f). This plot shows the transversal momentum as function of the longitudinal momentum of the electrons in the $N_2O^+ + e^-$ channel. The fact that this distribution is centered and the ring-like structure follows perfect semicircles (see the white dotted lines in figure 7.18(f)) indicates a good parameter settings for the electrons.

7.3 Acceptance

The acceptance of a spectrometer is defined by the maximum momentum, which can be measured. Fragments emitted exactly towards the detector can be measured, regardless of their momentum, whereas all other particles can only be detected up to a certain momentum. The absolute value of it depends on several parameters as the emission angle, the acceleration length, the size of the MCP-detectors, the extraction voltage, and the strength of the magnetic field. Some examples are depicted in figure 7.19.

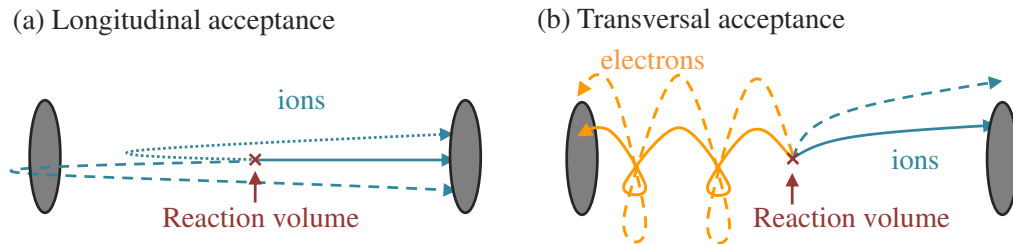


Figure 7.19: From [13]. (a) Illustration of the acceptance for the longitudinal momentum of the ions. For high longitudinal momenta pointing in opposite direction as the respective detector, the particles can not be decelerated within the spectrometer length at a given electric field. The same also applies for electrons. (b) Transversal acceptance. Ions and electrons with too high transversal momentum at given B - and E -fields as well as spectrometer geometry are not projected onto the detector area as depicted.

Particles emitted along the spectrometer axis z , but in opposite direction of the respective detector, are firstly decelerated by the electric field before they are driven back towards the detector. The deceleration length has to be smaller, than the spectrometer length. The maximum momentum $p_{-z,max}$ and the maximum energy $E_{-z,max}$ can be written in SI units as

$$p_{-z,max} = \sqrt{2mqU} \quad \text{and} \quad E_{-z,max} = qU, \quad (7.14)$$

with m and q the mass and the charge of the particle and U the extraction voltage (250 V in the experiment presented in chapter V). In the case, the particles are emitted perpendicular to the spectrometer axis, ions and electrons have to be treated separately. The influence of the magnetic field is negligible for the ions, whereas the electrons are strongly affected. The maximal transversal momentum for the ions $p_{r,max}$ (and the corresponding maximal energy $E_{r,max}$) is dependent on the ratio of the radius of the detector r_{det} and the spectrometer length l :

$$p_{r,max} = \frac{r_{det}}{l} \sqrt{\frac{mqU}{2}} \quad \text{and} \quad E_{r,max} = \frac{r_{det}^2}{l^2} \frac{qU}{4}. \quad (7.15)$$

Consequently, the extraction voltage has to be adapted for the particular processes and the expected momenta. In single ionization of atoms the kinetic energy of the ions generated is low and extraction voltages in the order of 1 – 2 V/cm can be sufficient. Using molecules as target, dissociation, or Coulomb explosions can occur. In such fragmentation processes, the ions gain much more kinetic energy and higher extraction voltages are necessary. For the conditions in the presented experiment ($U = 250$ V, $l = 154,5$ mm, $r_{det} = 40$ mm) one obtains a maximal transversal energy of the ions of $E_{r,max} \approx 4.2$ eV.

The maximum transverse momentum of the electrons $p_{e,r,max}$ (and the respective maximum energy $E_{e,r,max}$) that can be detected with the full solid angle is determined by their gyroradius, which has to be smaller than the half radius of the detector r_{det} (compare figure 7.17). One yields

$$p_{e,r,max} = \frac{qBr_{det}}{2} \quad \text{and} \quad E_{e,r,max} = \frac{(qBr_{det})^2}{8m_e}, \quad (7.16)$$

where q is the charge, B is the magnetic field strength. In the presented setup, the MCPs installed have diameter of 80 mm and the magnetic field is set to ~ 7.88 Gauss. Electrons

up to 21.8 eV can be measured at these parameters for all emission angles.

7.4 Resolution

The momentum resolution of the ReMi is limited by several factors. The main contributions for the momentum resolution of the ions is caused by the thermal motion of the particles in the target jet. As introduced in section 7.1.1 the momentum spreads are given by $\Delta p_{therm,x} \approx \Delta p_{therm,z} \approx 0.14$ a.u. and $\Delta p_{therm,y} \approx 0.89$ a.u..

In addition, one has to account for the temporal and spatial resolutions of the detectors. As mentioned earlier, the uncertainty in the TOF is $\Delta t = 1$ ns and the spatial resolution is $\Delta R = 0.5$ mm. It is possible to estimate the momentum resolution as [104]

$$\Delta p_z^2 = \Delta p_{therm}^2 + \left((8.039 \times 10^{-3} \frac{\text{cm a.u.}}{\text{eV ns}}) \cdot \frac{qU}{l} \Delta t \right)^2 \quad (7.17)$$

$$\Delta p_r^2 = \Delta p_{therm}^2 + \left((11.6 \frac{\text{a.u.}}{\sqrt{\text{amu eV}}}) \cdot \frac{\sqrt{qUm}}{2l} \Delta R \right)^2. \quad (7.18)$$

Besides the influences already mentioned, the resolution can be downgraded by the uncertainty in the source position. It is related to the size of the reaction volume, which is confined by the extension of the gas jet ($A \approx 1.6$ mm) along the laser propagation axis, since the gas jet is smaller than the Rayleigh length of the XUV ($z_R \approx 10$ mm) and by the focal size of the laser focus $w_f \approx 30$ μm in y - and z - directions. Nevertheless, an expected momentum spread in the laser-propagation direction could not be observed experimentally [13]. In addition, inhomogeneities of the electric and magnetic field can degrade the momentum resolution. To avoid this effect, the careful design was accompanied by electric field simulations and alignment tests of the Helmholtz coils [92].

In the experiments presented in part V the extraction voltage was $U = 250$ V. With this voltage, the expected final resolution for the ions is $\Delta p_x = 1.88$ a.u., $\Delta p_y = 2.07$ a.u., and $\Delta p_z = 0.19$ a.u..

For the momentum resolution of the electrons the thermal motion can be disregarded. The kinetic energies transferred to the electrons exceed the thermal kinetic many times. Therefore, only the uncertainty of TOF and the spatial resolution has to be taken into account. In addition, the momentum resolution depends on the gyromotion of the electrons. Electrons detected after an integer multiple of cycles cannot be resolved in momentum, due to the fact that in this case all electrons are projected to one point of the detector, independently to their momentum. By changing the extraction voltage, it is possible to

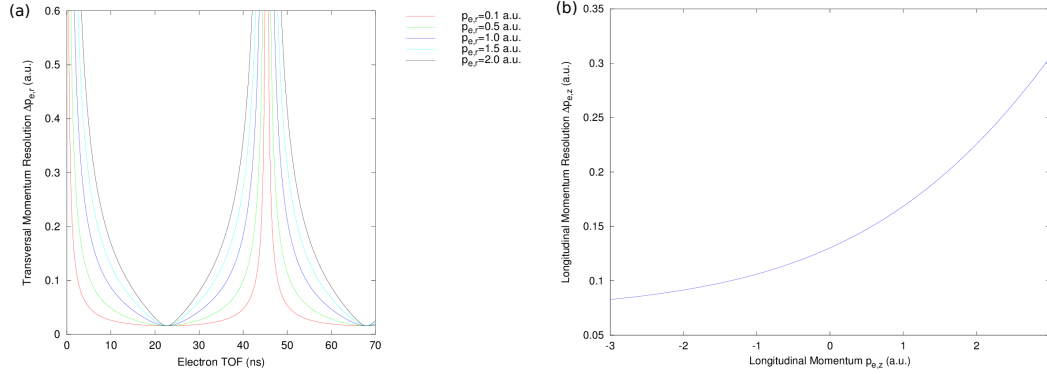


Figure 7.20: Resolution of (a) the transversal and (b) the longitudinal electron momentum calculated for the settings of the experiment presented in chapter V. The uncertainty of the transversal momentum depends on the considered momentum. Therefore in (a) the resolution is plotted for several (experimental relevant) momenta.

avoid such singularities within the interesting momentum regime. The resolution of the respective momenta can be estimated as [104]

$$\Delta p_{e,r} = \frac{4.02 \times 10^{-3} \frac{\text{a.u.}}{\text{mm G}}}{|\sin(\frac{1}{2}\omega_c t_e)|} \cdot B \cdot \sqrt{\Delta R^2 + \left(\frac{p_{e,r} \cdot \Delta t_e \cdot |\sin(\frac{1}{2}\omega_c t_e)|}{m_e \tan(\frac{1}{2}\omega_c t_e)} \right)^2} \quad (7.19)$$

and

$$\Delta p_{e,z} = 0.219 \frac{\text{cm a.u.}}{\text{ns}} \cdot \frac{\left(\sqrt{\frac{p_{e,z}^2}{2} + \frac{U}{27.2114 \text{ V a.u.}^{-1}}} + \frac{p_{e,z}}{\sqrt{2}} \right)^2 \sqrt{p_{e,z}^2 + \frac{2U}{27.2114 \text{ V a.u.}^{-1}}}}{p_{e,z} + \sqrt{p_{e,z}^2 + \frac{2U}{27.2114 \text{ V a.u.}^{-1}}}} \cdot \frac{\Delta t_e}{l}, \quad (7.20)$$

for $\Delta p_{e,r}$ and $\Delta p_{e,z}$ being the uncertainty transversal ($p_{e,r}$) and longitudinal ($p_{e,z}$) momentum, ω_c the cyclotron frequency, t_e the TOF of the electrons with mass m_e , the extraction voltage U , the spectrometer length $l = 154.5$ mm, $\Delta R = 0.5$ mm the spatial and $\Delta t = 1$ ns the TOF resolution. Figure 7.20 shows the uncertainty of transversal and longitudinal momentum computed for the settings of the experiment presented in chapter V. The extraction voltage is 250 V and the magnetic field 7.88 G. The TOF distribution of the

electrons is centered around ≈ 35 ns (see figure 7.18(c)) and the respective momenta are in the range of > -1.5 to < 1.5 a.u.. The achieved resolutions of the momenta can be extracted from figure 7.20. The uncertainty of the transversal momentum (photoelectron energy) in the experiment is between 0.015 a.u. (3.1 meV) and 0.5 a.u. (3.40 eV) depending on the momentum and the TOF. The longitudinal momentum can be resolved by 0.08 a.u. (0.09 eV) to 0.25 a.u. (0.85 eV). The relevant part of the photoelectron energies is well below 20 eV, which corresponds to a momentum of 1.21 a.u.. Then, the resolution for TOFs below 40 ns is better than 0.22 a.u. (0.66 eV) for the transversal and 0.18 a.u. (0.44 eV) for the longitudinal direction.

IV The XUV Spectrometer

One essential part of my work was the design, construction and implementation of a new XUV-spectrometer positioned after the ReMi in order to better control the experiment. As described in section 6.3, the setup already includes a similar spectrometer situated before the ReMi and some disadvantages of this device led to the idea to design an improved version. One of the main reasons is the position of the present spectrometer, which was mounted at the side of the HHG chamber (compare figure 6.10). As a result, a mirror has to be inserted into the XUV-beam path, between the HHG setup and the ReMi, to guide the harmonic radiation into the spectrometer to operate it. Therefore, it was not possible to access the harmonic spectrum without disrupting an ongoing measurement. The observation of the XUV spectrum during a measurement is, however, very useful to control the stability of the HHG source, such as e.g. a change in the produced photon energies, which can be a crucial parameter for some experiments. In addition, the design of the former setup contained a free-standing transmission grating to spectrally resolve the harmonic light and a CCD-chip to detect it. Both are responsible for low detection efficiency of low-energy harmonics (< 30 eV) in the high-harmonic spectrum (see figure 9.5), which in fact is the most intense part produced in argon and an important energy region for several experiments [13].

In this chapter, the design of the new spectrometer will be presented trying to overcome the disadvantages mentioned above. Thereafter, I will discuss how the spectrometer is combined with the ReMi spectrometer with special attention given to the operation of the spectrometer without influencing ongoing experiments. Finally, the calibration of the XUV spectrometer will be presented.

8 Design of an XUV Spectrometer

8.1 Overview

The newly designed spectrometer uses the light passing the ReMi. Figure 8.1 gives an overview over the entire spectrometer setup starting from the ReMi. Before the new assembly was implemented, the light exiting the ReMi was used to spatially and temporally align both interferometer arms. The focus in the ReMi was mapped by a lens onto a small CCD-camera, thus, the foci of the IR-beam path and the XUV-beam path (in which the Al filter was removed and the IR light passing the HHG cell was used) could be spatially overlaid. In addition, the temporal overlap of the pulses can be determined by means of the interference occurring when both pulses superimpose in the focus. In order to preserve this adjustment tool, a cross fitting was inserted right behind the ReMi. There, a mirror can be inserted by a linear translator, deflecting the beam by 90° through a view port after which the beam is used for adjustment as before. The view port is tilted to avoid direct back reflections of the light into the ReMi which could create a high background signal. Although the cross fitting is only pumped indirectly through the ReMi, the vacuum in the experimental chamber is not significantly affected. The cross fitting is followed by a gate valve¹⁴, which separates the vacuum of the ReMi from the vacuum of the spectrometer when it is not in operation or vented. The gate valve is equipped with an optical view port, thus, the vented spectrometer can be aligned. For this purpose, a HeNe laser can be coupled into the identical beam path as the IR laser.

A differential pumping stage ensures that the spectrometer can be operated during experiments in the ReMi. In order to have a low background coming from the residual gas, UHV vacuum is needed in the ReMi. We achieve pressures around 7×10^{-10} mbar, when the gas jet as well as the detectors are switched on. The pressure in the XUV spectrometer is about 1×10^{-8} . This is mainly due to some motorized components, such as a rotational stage, a flip mirror and a piezo-driven mirror support. In addition, the actual spectrometer is placed in a 36.5 cm long DN100 tube section including a diaphragm bellow. This section is only pumped indirectly and additionally the bellow provides a large surface area. The differential pumping stage consists of a cross fitting pumped by a 70 l/s turbo molecular pump (TMP). It is separated from the ReMi and the spectrometer

¹⁴ Custom made pneumatic double valve from VAT Deutschland GmbH, Am Hochacker 4, 85630 Grasbrunn, www.vatvalve.com

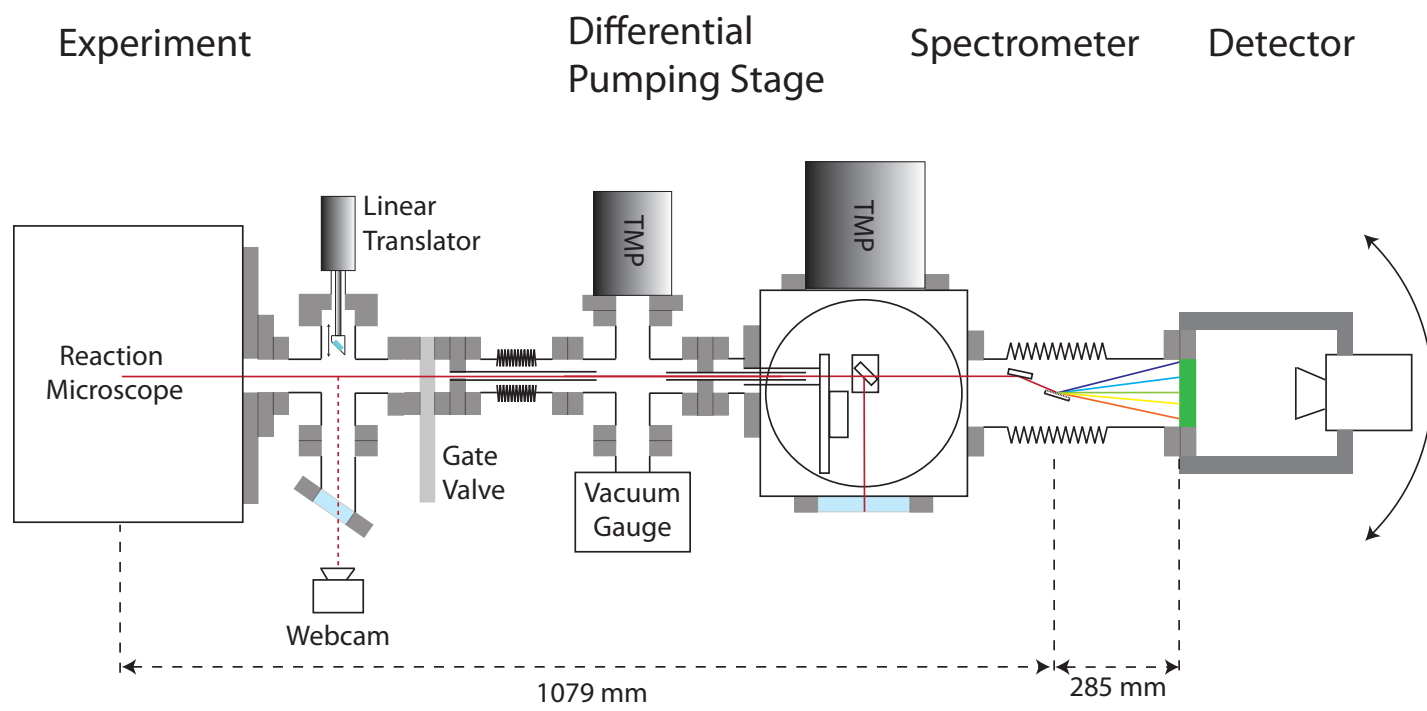
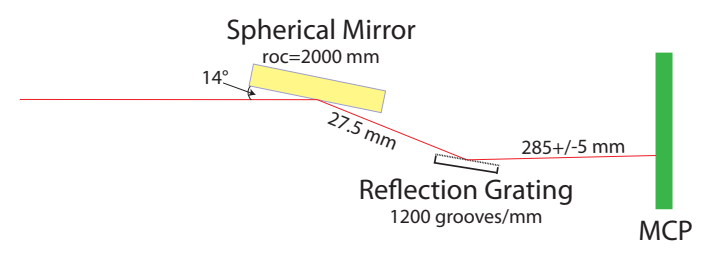


Figure 8.1: Overview of the XUV-spectrometer setup.



by two tube sections with a diameter of 10 mm and a length of 10 cm. The differential pumping stage is designed to hold at least a pressure gradient of one order of magnitude. At this stage, a diaphragm bellow serves as flexible connection between the ReMi and the spectrometer.

The main chamber of the spectrometer is a DN160 cubic vacuum vessel¹⁵. It is pumped via a 300 l/s TMP. A filter wheel mounted on a rotation stage can introduce an additional metal filter into the beam path. On one hand, this serves to get rid of the IR-probe beam to minimize stray light on the detector and, on the other hand, the brightness of the harmonics on the detector can be regulated by inserting filters with varying thickness. Furthermore, a flip mirror is placed in the cube. It guides the beam through a view port outside the chamber, where it also could be used for the adjustment of the experiment.

Finally, the beam is entering the actual spectrometer section. It is placed in a DN100 tube section. The beam is focused by a spherical gold mirror with an roc of 2000 mm hit in grazing incidence ($\approx 14^\circ$), which leads to a strongly astigmatic focus. The focus in the horizontal dimension is on the detector plane. The light is spectrally resolved by a 1200 ln/mm reflection grating. The spectrum is detected with an uncoated 40 mm MCP detector in order to be sensitive for the low energetic harmonics and to be insensitive for IR light. The MCP signal is visualized by a fast *P47* phosphor screen, which is read out by a cooled CCD-camera¹⁶.

8.2 Spectrometer

The design of the spectrometer section is kept simple. All optical elements are placed on a cantilever which is mounted in the vacuum cube. It forms a plane guiding into the DN100 tube section and it ends in the bellow area, such that the diffraction grating can be placed in the turning point of the diaphragm bellow, as it is depicted in figure 8.2. The focusing optic is a gold-coated spherical mirror. It is hit under 14° grazing incidence (corresponding to 76° to the surface normal). The required focal length f of the mirror was calculated with the relation

$$\frac{1}{f} = \frac{1}{b} + \frac{1}{g}, \quad (8.1)$$

¹⁵ from PINK GmbH Vakuumentchnik, 97877 Wertheim, www.pink.de

¹⁶ CoolSNAP:K4 camera system from Photometrics, 3440 E. Britannia Drive, Tucson, Az 85706, www.photometrics.com

with the image distance b and g the object distance, which is the spacing between the focus of the XUV beam in the ReMi and the center of the focusing mirror. The focus position in the ReMi was estimated to be in the center of the chamber, which is traversed by the target jet. The exact displacement was calculated as $g \approx 1079$ mm using the dimensions of the standard vacuum parts and a detailed CAD drawing of the spectrometer setup. The image distance is composed by the spacing between mirror and grating (27.5 mm) as well as from there to the detector plane (285 mm). This results in a focal length of $f = 242.3$ mm. One has to account for not hitting the spherical mirror in normal incidence. The focus is astigmatic which means that the mirror has different focal lengths for the horizontal and vertical dimension of the beam. The original focal length of the mirror is modified by a factor, namely

$$f_{hor} = f_0 \cdot \cos(90^\circ - \alpha) \quad (8.2)$$

for the horizontal and

$$f_{vert} = \frac{f_0}{\cos(90^\circ - \alpha)} \quad (8.3)$$

for the vertical direction. Preferably, the horizontal focus shall be at the detector plane. In this case the focal length of the mirror has to be

$$f_0 = \frac{f_{hor}}{\cos(90^\circ - \alpha)} = \frac{242.3 \text{ mm}}{\cos(76^\circ)} = 1001.6 \text{ mm}. \quad (8.4)$$

According to the availability a mirror with $roc = 2000$ mm was chosen, since the roc is twice the focal length.

A holographic reflective diffraction grating¹⁷ is used to spectrally resolve the harmonic light. The laser hits the grating at the same incidence angle as the focusing mirror in order to let propagate the 0th order parallel to the incoming beam. The grating has a lattice parameter of 1200 grooves/mm and is coated with aluminum. It is not specially specified for the XUV regime, for which aluminum has not the highest reflectivity. Nevertheless, the signal is still high enough for the detector and in addition these gratings are cheap and fast available. Several gratings with different lattice parameters could be tested to find an

¹⁷ from Thorlabs Inc, 56 Sparta Avaneue, Newton, New Jersey 07860, www.thorlabs.com

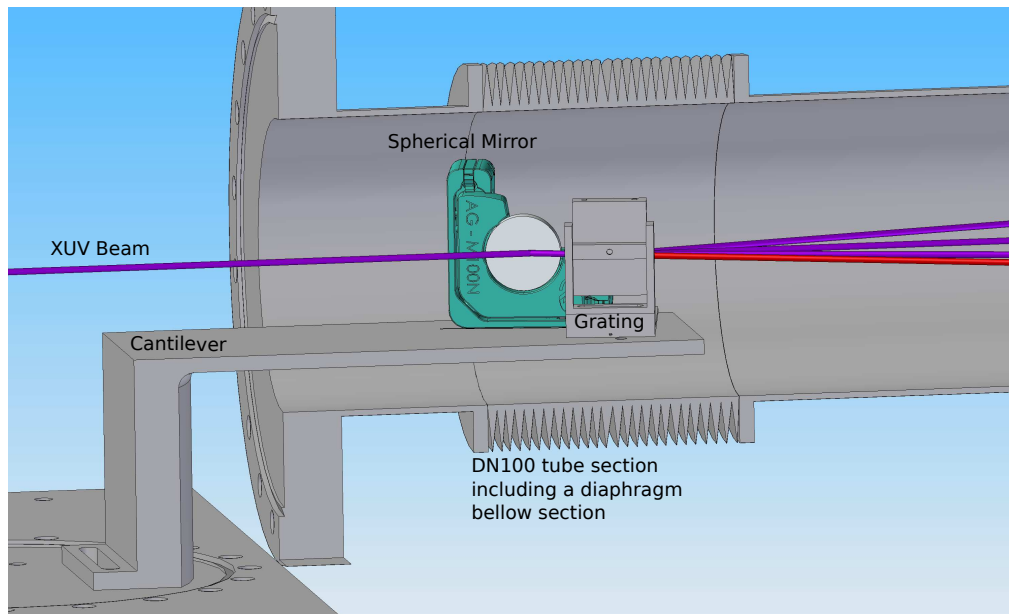


Figure 8.2: CAD drawing of the DN100 tube section with the diaphragm bellow and the cantilever, which supports the spherical mirror and the grating.

optimum between resolution and diffraction angle with the option to replace the grating by a specially designed one. Currently, the lattice spacing used permits to detect the 0th and the most energetic harmonics in one and the whole harmonic spectrum at a second position of the detector. As a result, the calibration can be performed easily and the total spectrum does not have to be composed by several pictures of different diffraction angles.

8.3 Detection System

The detection system is mounted at the end of the DN100 tube section. It can be turned in a circle around the center of the grating and be fixed at certain, defined positions. Furthermore, the distance between the grating and the detector can be slightly varied (± 10 mm) in order to adapt the detector plane to the exact focal position, since the focal position depends on the incidence angle on the focusing mirror, which can be slightly modified through changes in the daily adjustment. The light is detected by an MCP detector with a diameter of 40 mm. Firstly, a chevron-assembled double-MCP was tested, but it turned out that a single MCP is enough to gain a sufficiently high signal. The detector is uncoated in order to not increase the quantum efficiency for IR light. A

phosphor screen coated with P47 phosphor is used to visualize the signal from the channel plate. The decay time of the screen ($\sim 3 \mu\text{s}$ from 90% to 1%) is in principle fast enough to resolve single APTs (12.5 ms time interval between two APTs at 8 kHz repetition rate). The difficulty is to find a high-speed camera to read out the phosphor screen, which is able to take 8000 frames per second (fps) at a reasonable resolution. Currently, a camera with a cooled CCD chip¹⁸ is used. It has 2048×2048 pixels, each with a size of $7.4 \times 7.4 \mu\text{m}^2$ and it is cooled down to -25°C . Its maximum read-out-speed is 12 fps. A common object lens¹⁹ images the phosphor screen onto the CCD chip. The camera is mounted at a fixed distance to the phosphor screen and the area in between is enfolded by a tube in order to have no stray light from the environment.

8.4 Subconstruction

The whole spectrometer is placed on a self-contained separate subconstruction. The design of it is oriented on the design of the support of the ReMi and consists of aluminum profiles²⁰. The construction is supported by height-adjustable feet in order to adapt the height of the spectrometer to the beam path of the experimental setup. Furthermore, the upper part sits on guide rails, such that the spectrometer can be moved perpendicular to the laser-beam propagation axis, not only to adjust the optical path in the spectrometer, but also because the ReMi can be moved on the same axis to find the best overlap between the target gas jet (moving with the ReMi) and the (fixed) laser beam. Moreover, the stand offers enough space to hold all technical devices needed, as controller for pumps, vacuum gauges and the motorized parts inside the spectrometer as well as a computer to read out the CCD camera.

I also designed a holding for the diaphragm bellow and the detector system. The bellow is needed to turn the detector around the grating. An adapter is mounted at each end of the DN100 bellow tube section. Both are connected with two aluminum posts that have a lockable hinge at the grating position and are lengthwise adjustable. It was necessary to account for the force with which the bellow is compressed ($\sim 100 \text{ kg}$) due to the pressure gradient between normal pressure and the vacuum inside the spectrometer.

¹⁸ Kodak KAI-4020M

¹⁹ Nikon Nikkor 50mm f/1.2 AI-s from Nikon GmbH, Tiefenbroicher Weg 25, 40472 Düsseldorf, www.nikon.de

²⁰ from item Industrietechnik GmbH, Friedensstraße 107-109, 42699 Solingen, www.item24.de

9 Combining the Spectrometer and the ReMi Technique

One of the major reasons to build the new spectrometer was the possibility to measure the harmonic spectrum during experiments in the ReMi in order to control the stability of the HHG. An important requirement is that connecting and operating the spectrometer is not influencing the ongoing experiments.

9.1 Operating the Spectrometer

In the first attempts to calibrate the spectra the HHG was optimized to the brightness of the harmonics and to high count rates in the ReMi. It turned out that the highest count rates are achieved, when the phase matching is optimal for both, short and long trajectories. As described in section 3.1, quantum-path interferences occur, affecting the spatial properties of the harmonic spectra. Figure 9.3 shows two different XUV spectra, one for phase-matching conditions supporting both trajectories and a second one, in which the long trajectory contribution is suppressed. In the case, both trajectories are efficiently phase matched, the complicated spatial high-harmonic structure does not allow a precise calibration. Therefore, phase-matching conditions were changed to a regime, in which only the short trajectories contribute to the harmonic spectrum, by changing the position of the HHG gas target with respect to the focal position. This can be achieved by focusing the laser beam in front of the HHG target. As a result, the brightness of the harmonics decreases and consequently the count rate in the ReMi drops dramatically to such an extent that it was impossible to carry out any experiment. The drastic intensity difference arises from the different positions, at which the HHG cell is placed, with respect to the focal position. Optimizing the HHG for the count rate in the reaction microscope results in a focal position close to the HHG cell. The adaption of the phase matching to see only the contribution of the short trajectory leads the focus away from the gas target. As a result, the available intensity of the laser pulses during the HHG process decreases and with that also the brightness of the produced XUV radiation.

Therefore, during measurements, the phase-matching conditions are adjusted to optimize the count rate in the ReMi. Nevertheless, in the most cases it is possible to extract a “clean” spectrum from the spectrometer by looking at the projection of a narrow window of the total 2-D spectrum, in which the quantum-path interferences are less distinct, as indicated in figure 9.3(c).

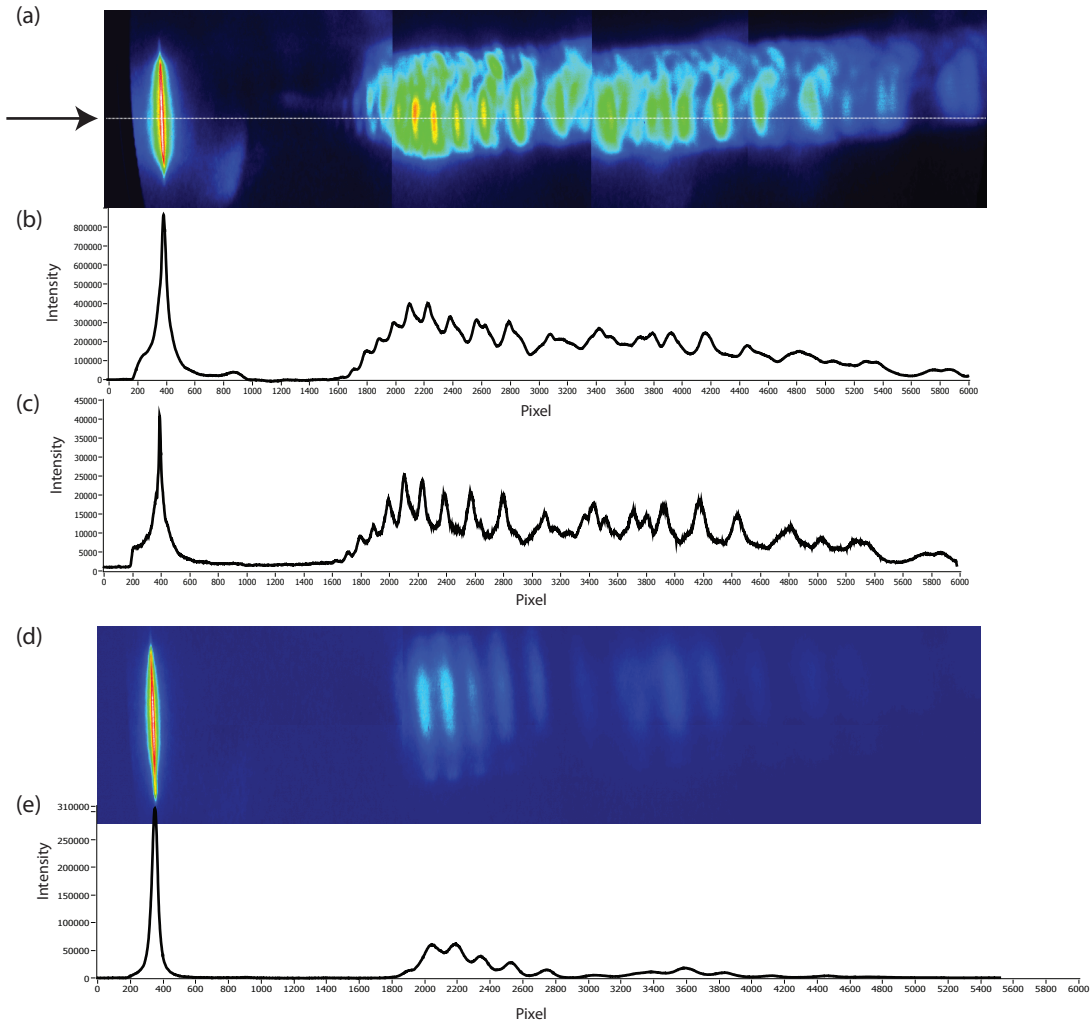


Figure 9.3: Two XUV spectra at two different focal positions. Both are shown as 2-D spatially resolved pictures ((a),(d)) and as projection onto the energy axis ((b),(e)). The upper XUV spectrum (a) was taken as the focal position was slightly behind, whereas in the lower spectrum (d) the focus was in front of the HHG cell. In the first case, the long and the short trajectories are phase matched leading to quantum-path interference, thus, the projected spectrum is barely interpretable. (c) shows a projection of a narrow window in (a). The window position is indicated with the black arrow and the white dotted line. The harmonic structure is more distinct compared to (b). The vertical lines in (a) are cutting points between different images that had to be merged to gain the total spectrum. They are also present in (d), but less pronounced.

9.2 Combining the Vacua

Eventually, a more crucial consideration for the simultaneous operation of the spectrometer is that the experiments are not affected. The usage of the XUV radiation necessitates that the vacua of the ReMi and the spectrometer have to be connected directly. A raised pressure in the ReMi would increase the background counts, thus rare reaction channels cannot be measured or the data acquisition has to be extended. Due to some technical reasons, it is difficult to decrease the pressure in the spectrometer to the same level (or lower) as in the ReMi. Therefore, the design of the spectrometer requires a carefully planned differential pumping stage. Its setup was already introduced in section 8.1 and is shown in more detail in figure 9.4. In the following, the calculations of the respective conductance values will be introduced and it will be shown that the differential pumping stage allows to connect both vacua without increasing the pressure in the ReMi.

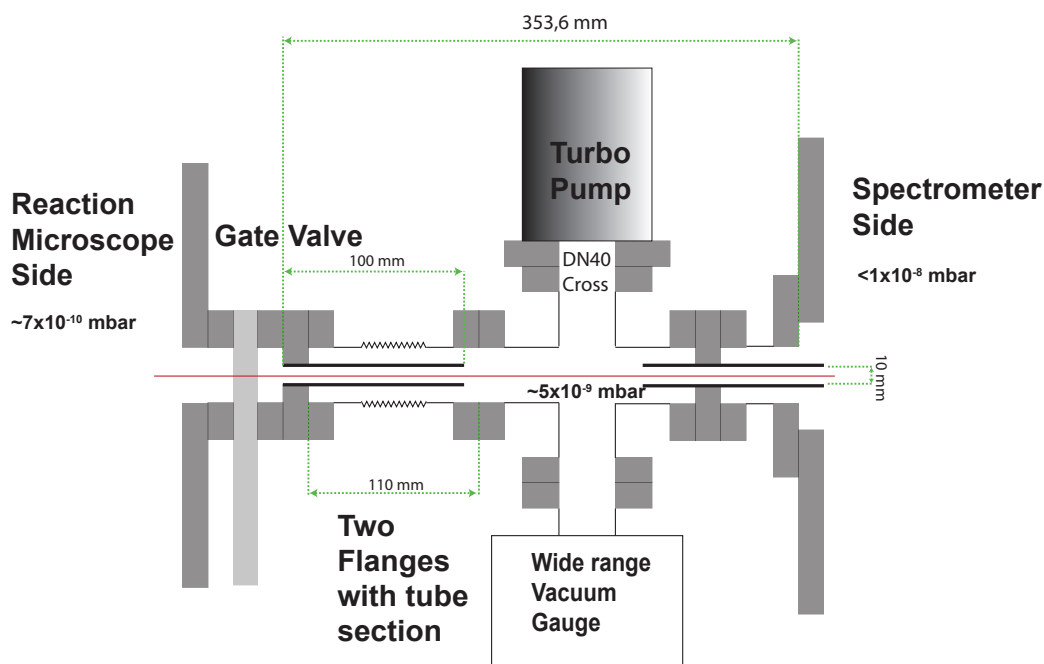


Figure 9.4: Schematic drawing of the differential pumping stage between ReMi and spectrometer.

The conductance value of a component specifies the volumetric flow rate between two vacuum chambers, which are connected with this component and accordingly it is possible

to calculate the expected pressure gradient $p_2 - p_1$ [109] with

$$p_2 = \frac{L}{S}p_1, \quad (9.5)$$

in which L is the conductance value and S is the pumping speed of the respective TMP. At the considered pressures, the conductance value is determined by the probability P , with which a particle with the velocity v passes the regarded component:

$$L = \frac{vA}{4}P, \quad (9.6)$$

with A the area of the aperture of the transition piece. The velocity v is the average particle velocity for a particle with the molar mass M at the given temperature T and it is calculated from a Maxwell distribution as

$$v = \sqrt{\frac{8RT}{\pi M}}, \quad (9.7)$$

with the gas constant $R = N_A \cdot k_B$. The probability for the passage of a particle P depends on the geometry of the transition piece. In the design of the differential pumping stage, a tube section is used with the length l and the diameter d . For a tube section the probability is given by

$$P = \frac{4d}{3l}. \quad (9.8)$$

Both tube sections, between the spectrometer and the differential pumping stage and between there and the ReMi, have diameter of 10 mm and a length of 10 cm. The differential pumping stage is pumped with a 70 l/s TMP resulting in a maximal pressure ratio of $\frac{p_{diff}}{p_{Spec}} = 6.2 \times 10^{-5}$ to the spectrometer and even better for the pressure ratio between differential pumping stage and ReMi, since the ReMi main chamber is pumped with a 500 l/s TMP. The ratio is by far good enough to separate the vacua of the ReMi and the spectrometer.

In operation it was verified that the spectrometer can in principle be operated during measurements without influencing the vacuum of the ReMi. However, opening the gate valve causes a slight increase of the background pressure in the non-operating ReMi, since

a small volume between the gate valve and the first tube section is only pumped indirectly. During experiments, the ReMi is also connected to the vacuum of the HHG chamber and the gas jet is turned on. Both are increasing the background pressure anyway, such that in operation the influence of opening the gate valve towards the spectrometer can not be observed anymore.

9.3 Experimental Benefits

As already mentioned, one of the benefits of the new spectrometer is the online monitoring of the generated XUV spectrum without interrupting an ongoing measurement. The acquisition of the spectra can easily be automated to provide a continuous observation and the collected data can be related²¹ to the data acquired in the ReMi in order to be able to subsequently, offline, select stable periods of the measurement.

The stability of the HHG can be a crucial parameter in certain experiments, particularly when using single, carrier-envelope phase stabilized attosecond pulses. However, even by using attosecond pulse trains, as for the experiments presented in this work, it is useful to measure the photon energies, which are interacting with the target atoms or molecules. In simple cases as e.g. in argon, single ionization originates from a single electronic state. Then, the photoelectron spectra can easily be interpreted and the corresponding photon energies can be extracted. In more complex systems, sometimes several electronic states can be involved, such that the harmonic structure vanishes in the photoelectron spectrum and the XUV spectrum cannot be obtained.

In the case of the nitrous oxide, several electronic states have an ionization potential accessible by the available photon energies. However, in the energy spectrum of the electrons produced by the single ionization of nitrous oxide, the harmonic structure can be observed, which indicates that a certain state is dominant in this process. The measured and carefully calibrated XUV spectrum can be used to assign the measured photoelectron energies to a respective state. Figure 9.5 depicts the XUV- and the photoelectron-spectrum. Both are shifted by 12.7 ± 0.3 eV, which is similar to the ionization potential of the $X^2\Pi$

²¹ It would be an extremely time-consuming task to include the read-out of the CCD-camera of the XUV spectrometer as well as the calibration of the respective spectra directly into the data-acquisition and analysis program of the ReMi, if not impossible. Therefore, the easiest way to link both data acquisitions with each other is to add a time-stamp to the stored data of both devices, if it is ensured that the clocks of the two involved computers are synchronized.

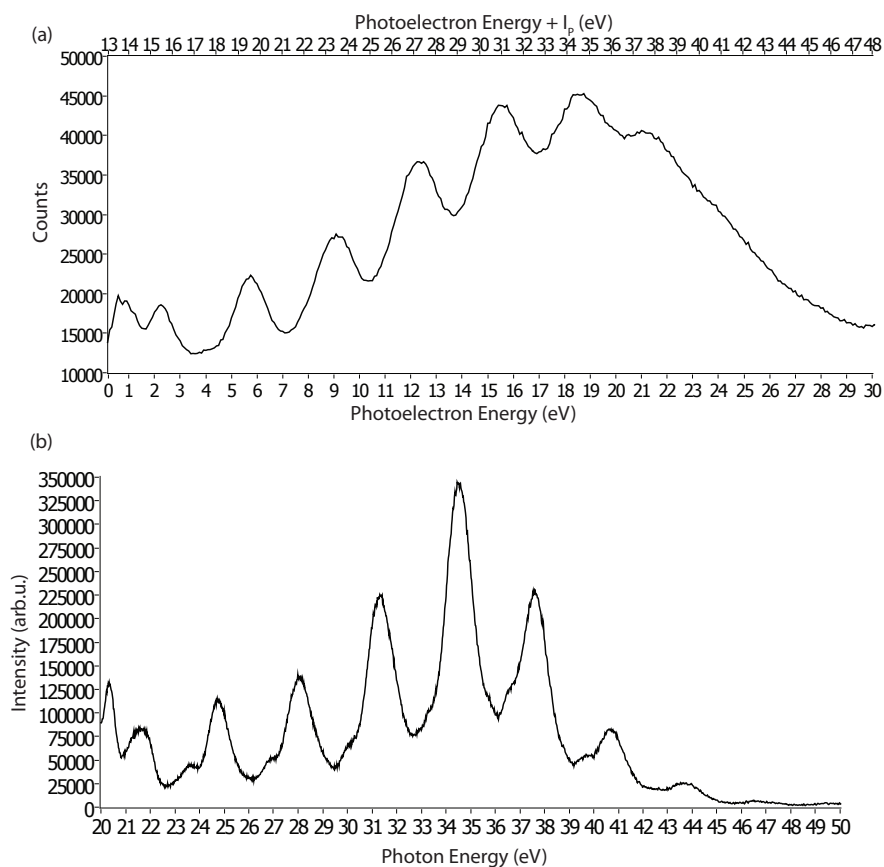


Figure 9.5: (a) Photoelectron spectrum measured in the ReMi with N_2O as target gas and Ar was used for HHG. The scale below the graph represents the measured photoelectron energies, whereas at the upper scale the ionization potential of the single ionized $X^2\Pi$ groundstate of N_2O (12.89 eV) is added. (b) The respective XUV spectrum observed in the XUV spectrometer.

state of N_2O with 12.89 eV [110].

10 Calibration of the Spectrometer

The spectrometer can be used to qualitatively improve the HHG for the experiments in the ReMi. In contrast to the former spectrometer, it really shows that the brightness of the XUV spectrum measured in the new spectrometer is correlated with the count rate of events in the ReMi. However, a calibration of the spectra is necessary to have access to the photon energies of the harmonic radiation used in the experiment as well as to be able to quantitatively estimate changes in the harmonic spectrum. In the following, the methods, which was used to calibrate the spectrometer, will be introduced.

10.1 Geometrical Calibration

One of the easiest methods for a first, rough calibration of a spectrometer is to utilize its geometry. The diffraction angle β of a certain wavelength λ is dependent on the lattice parameter g and the incidence angle α . One obtains

$$n \cdot \lambda = g \cdot (\sin(\alpha) - \sin(\beta)), \quad (10.9)$$

with the diffraction order n . The angles are related to the surface normal of the grating. To measure the incidence angle to the grating, a photograph is taken from bird's eye view of the spectrometer setup, which is adjusted in a way that the laser beam hits the optical elements centrally and, additionally, the incoming beam and the 0th order of the grating are parallel. An exemplary picture is shown in figure 10.6 and it is depicted, how the incidence angle is estimated. The diffraction angle β of a certain harmonic is assessed by the distance x between the 0th order, which corresponds to light directly reflected with the incidence angle α , and the position of the respective harmonic and the distance between the grating and the detector. Now it is possible to calculate the wavelength (or energy) for every diffraction angle.

In the measurement of the incidence and diffraction angles are several sources of uncertainty. The beam pointing of the laser may change, influencing both angles, but due to the well confined XUV beam path the changes are less than 0.1° . In addition, the distance between the grating and the detector can only be roughly estimated, since both are inside a vacuum chamber. The uncertainty of the length is in the order of a few millimeters. In total, it is assumed that both incident and diffraction angle have a measuring error of $\pm 0.5^\circ$, which leads to an uncertainty of ± 3.7 eV in the energy calibration.

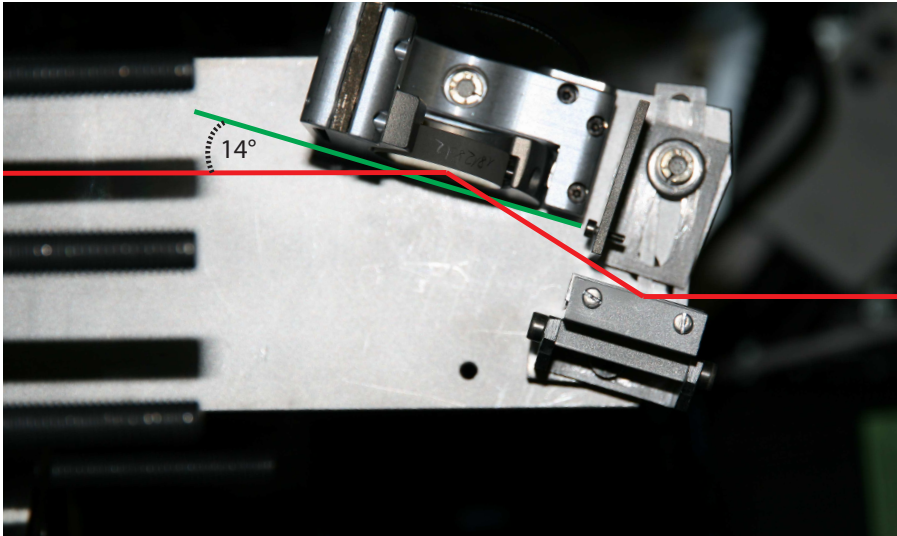


Figure 10.6: Photograph of the spectrometer from bird's eye view. The laser path is drawn in red. Such pictures are used to estimate the incidence angles on the spherical mirror and the grating, whereat both are parallel. In addition, the beam path length between the two optical elements can be measured.

This means, the error is in the range of one harmonic order. However, the calibration can be improved by using the property of the harmonic radiation that the individual spectral components are equally spaced in energy as it will be described in the following section.

10.2 Improving the Calibration with the ReMi

It is also possible to extract the HHG spectrum from the photoelectron spectra measured in the ReMi, but there, the spectral intensities are affected by the photo-ionization cross-section of the respective target gas. In addition, in targets, in which the XUV radiation is able to ionize multiple states, it is sometimes difficult, or even impossible to extract the harmonic spectrum from the photoelectron energy spectrum. Furthermore, the harmonic spectrum in the spectrometer is accessible faster than a few seconds, whereas the photoelectron spectrum needs to be integrated over a longer period (at least several minutes) to have enough statistics. And moreover, a set of experimental parameters (compare to section 7.2.3) has to be modified for separate runs of the experiment with different settings in order to be able to interpret the measured signals in the ReMi and to produce accurate photoelectron spectra.

Nevertheless, the photoelectron spectra can be used to improve the geometrical calibration. For this purpose, argon is used as target gas in the HHG as well as in the ReMi. In the single ionization of argon with the XUV photons, a single electronic state is involved with an ionization potential of $I_p = 15.76$ eV. As a result, the photoelectron spectrum clearly shows the structure of the harmonic radiation and it can be accurately calibrated using the method presented in section 7.2.3.

Now, it is possible to use the property of the harmonic radiation that the individual spectral components are equally spaced in energy. The spacing can be extracted from the photoelectron spectra or from the spectrum of the IR pulses directly and used to adapt the parameters of the calibration of the spectrometer. The incidence angle and the distance between grating and detector can then be slightly changed in order to achieve equidistant harmonic energies in the measured spectra with the respective spacing.

Due to the fact that the energies of the photoelectrons E_e and of the XUV photons E_{XUV} are correlated, the harmonic spectrum can be obtained by the sum of the photoelectron energy and the ionization potential $E_{\text{XUV}} = E_e + I_p$. Then, the photon-energy spectrum obtained from the photoelectron spectrum is compared to the XUV spectrum calibrated with the adapted parameters. Figure 10.7 shows two spectra for argon as target gas, one measured in the ReMi and one in the XUV spectrometer. With the ionization potential of argon (15.76 eV), it is possible to calculate the energies of the spectral components of the harmonics from the photoelectron spectrum and compare them directly to the XUV spectrum. It can be obtained that the XUV and the photoelectron spectra, shown in figure 10.7, differ by 15.63 ± 0.14 eV, which is in good agreement with the ionization potential of argon and which indicates that the measured XUV spectrum now agrees with the actual harmonic spectrum.

Similar to the spectra of the former spectrometer, the XUV spectrum shows higher energetic harmonics as the spectrum reconstructed from the photoelectrons. The Cooper minimum in argon is determined by the photo-ionization cross-section. In HHG, the Cooper minimum can be shifted towards higher energies due to phase-matching effects [101], whereas the yield of the photo-ionization process (in the ReMi) follows strictly the photo-ionization cross-section.

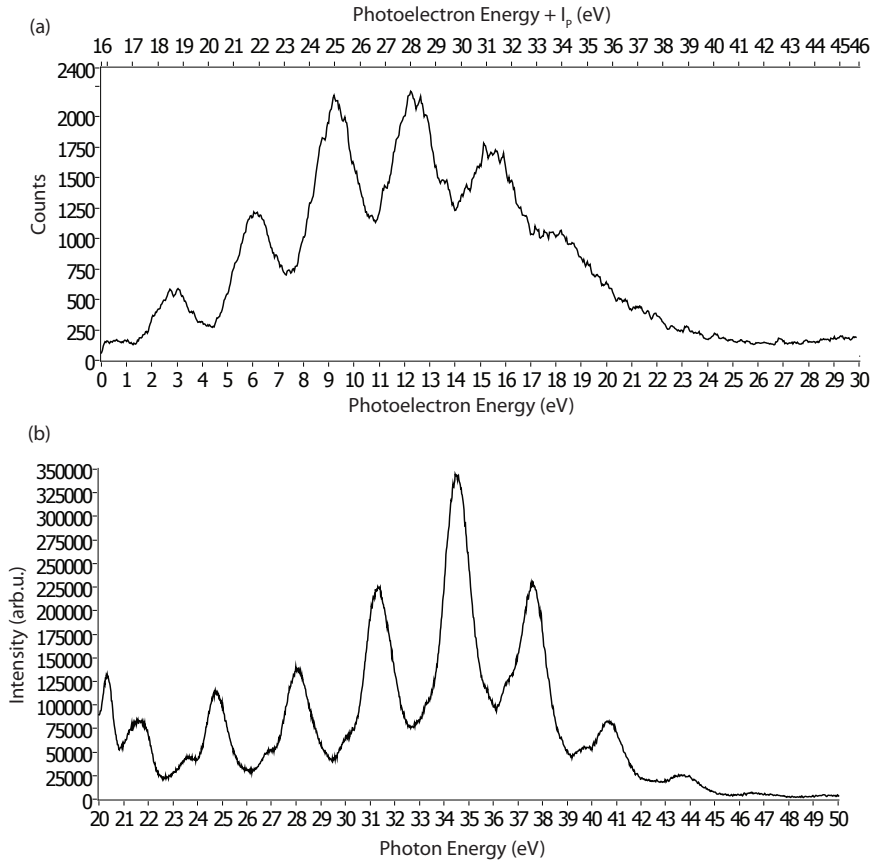


Figure 10.7: (a) Photoelectron spectrum measured in the ReMi with *Ar* as target gas, as well as HHG target. As before, the scale below the graph represents the measured photoelectron energies, whereas at the upper scale the ionization potential for single ionization of *Ar* (15.76 eV) is added. (b) The respective XUV spectrum observed in the XUV spectrometer.

10.3 Outlook

Despite first satisfactory tests of the new spectrometer, further improvements of the setup can be useful and are partially planned.

First of all, the first tests were showing that the support of the diaphragm bellow and the detection system can be slightly distorted by moving the detector position and by other external influences. Furthermore, the construction to fix the detection system at a certain position was built as an interim solution. It is planned to upgrade this system in

collaboration with the in-house engineering department to a more stable version.

The spectrometer was designed to observe the harmonic spectrum, which needs a lower resolution as using the device for experiments as for example transient absorption, which is not possible in our current setup. During the first efforts for a precise calibration, we had the idea to use a gas mixture of argon and helium in the HHG cell. While the fundamental IR is too weak to produce harmonics in helium, the goal was to produce harmonic radiation in argon and generate an absorption spectrum in the present helium. However, the resolution of the spectrometer is not sufficient to detect the sharp absorption lines.

In addition, the grating currently used is not designed for XUV wavelengths²² and, as a consequence of this, apparently the second diffraction order has a similar intensity as the first diffraction order. Both are overlapping in the low-energy part of the first diffraction order so that the low harmonics are not visible. These effects could be circumvented using a grating, which is designed for the XUV regime. Furthermore, to improve the resolution of the spectrometer and to reduce intensity losses, the current setup of a focusing mirror and a plane grating could be replaced by a focusing, aberration-corrected grating, which are used for example to perform high-resolution transient-absorption experiments, such as described in [111, 112].

²² The decision to implement such a simple grating was made based on several reasons, such as long delivery times of XUV gratings of approximately 6 months, in order to complete and test the whole spectrometer setup without waiting time. In addition, the fast availability and the lower costs (by a factor of 140) enabled the possibility to test gratings with different lattice spacings and shapes in order to find an optimum for our application, before ordering a purpose-built item, which can easily be implemented subsequently.

V Experimental Results

The following chapter presents the results of an XUV-IR pump-probe measurement in nitrous oxide (N_2O). The IR pulses are produced in a Ti:Sa amplifier system, spectrally broadened via SPM and recompressed in order to gain pulses with approximately 10 fs FWHM. In the experiment, the pulses are divided into two parts. The weaker part, 30% of the total pulse energy, is passing a delay stage and serves as probe pulse. Its final intensity is adapted by an aperture, such that no ionization events from the IR pulses alone are detected. With the remaining part, attosecond pulse trains are produced via HHG, which are then used as pump pulses. The spectrum of the produced harmonic radiation (see figure 9.5(b)) was determined by the XUV spectrometer, which was built within the scope of this work and presented in section IV. It shows that the XUV pulses provide energies between 15 eV (emission threshold for the aluminum filters) and ~ 45 eV. Both, pump- and probe pulse are focused collinearly into the gas target of the ReMi.

As it will be shown, it was possible to extract the pulse durations of the fundamental IR and the XUV-pulse trains²³ from the experimental data. It can be estimated that the IR pulses had a FWHM duration of approximately 25 fs, which indicates that the pulse compression worked not perfectly during the measurement. The delay scan was performed over 130 fs, at which the values were changed from -75 fs to 55 fs. Negative delays represent the times, at which the XUV pulse trains arrive the target first.

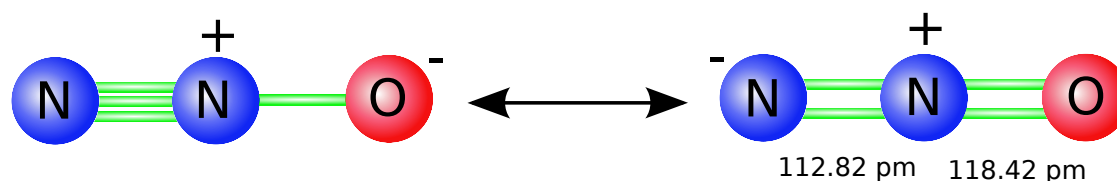


Figure 10.1: Adapted from [113]. Contributing structures of N_2O .

²³ It was not possible to determine the pulse duration differently, since no suitable device as an autocorrelator is currently installed.

The studied target, nitrous oxide, is a linear triatomic molecule. Its structure is depicted in figure 10.1 and it has two contributing structures, namely either with a triple bond between the two nitrogen atoms and a single bond between the central nitrogen and the oxygen, or with two double bonds between the three nuclei. In the last decades, the properties of this molecule was studied in various experiments, such as (e,2e) experiments [110, 114–116], measurements with synchrotron radiation [117–119] and also XUV-IR pump-probe studies [120].

With the available energy of the XUV radiation, it is possible to access several states [121]. The states of the singly ionized molecule are the ground state X^2II (12.89 eV), the first excited state $A^2\Sigma^+$ (16.38 eV), the second excited state B^2II (17.65 eV), and the third excited state $C^2\Sigma^+$ (20.11 eV) [122]. Furthermore, the highest photon energies in the XUV spectrum exceed the double ionization threshold of nitrous oxide, which is at an energy of 35.8 eV [123].

At first, an overview will be given, in which it will be shown, which particles are detected, as well as ionic fragments that are measured coincidentally indicating several dissociation channels of the dication. Afterwards, it will starting with data from the single ionization in a stable state of N_2O^+ with a special attention to the time-dependent photoelectron spectrum. Besides the stable singly ionized molecules, it can dissociate into a charged and a neutral fragment. The different dissociation channels will be inspected, showing the branching ratios between the different fragmentation processes and also the different kinetic energy release distributions. Finally, the results of the double ionization of nitrous oxide will be shown. Here, especially delay-dependent effects of the ionization yield and the kinetic energy release will be discussed for the two possible decay channels, as well as the respective photoelectron energies.

11 Overview

For a first analysis of a measurement and to obtain a general idea of the possible reaction channels of the experiment, the fragment time-of-flight (TOF) spectrum is an important tool. Figure 11.2 shows the ion TOF spectrum for the presented experiment. The strongest and very narrow peak can be identified as the singly charged parent-ion N_2O^+ , since it is the most efficiently produced particle and the sharpness of the line indicates that the corresponding particles are produced directly from the cold target jet. All other fragments can then be identified by comparing their charge-to-mass ratios. Besides the parental ion, all other possible, singly charged fragments are produced, namely N^+ , O^+ , N_2^+ , and NO^+ . Even the dimer $(N_2O)_2^+$ can be found. Additionally, a small amount of Argon is measured, which was still present from a previous measurement, as well as water and its fragments OH^+ , H_2^+ , and H^+ coming from the residual gas.

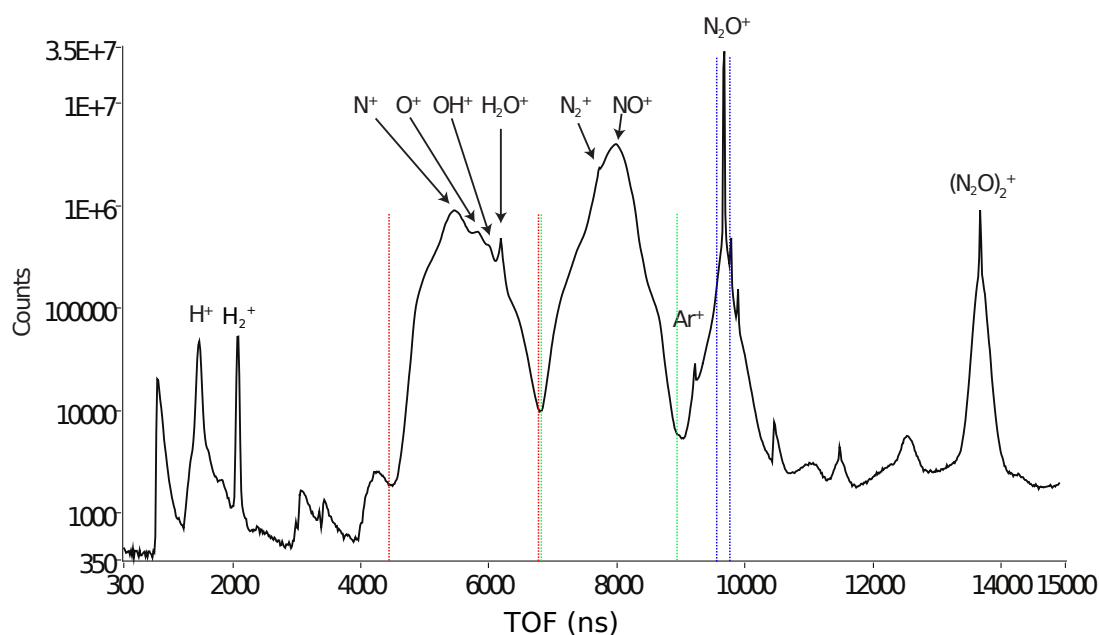


Figure 11.2: Time-of-flight spectrum for the presented measurement. The colored dotted lines indicate TOF windows set for the analysis: blue for N_2O^+ , green for N_2^+ and NO^+ , and red for N^+ and O^+ .

The atomic and diatomic fragments of the nitrous oxide have a broader TOF distribution, such that it is impossible to separate the TOFs of NO^+ and N_2^+ , as well as of N^+ and

O^+ .

Another informative plot is the photoion-photoion coincidence map (PiPiCo). The TOF of one ion is plotted as a function of the TOF of a second ion. Since the gas density of the target jet as well as the laser intensity is chosen such that (ideally) only one event occurs for every laser pulse, it is possible to relate several fragments measured in a certain time window to a distinct parent ion. If two ions are produced in a fragmentation process, they share equal absolute values of their momentum. Therefore, these events are distributed on characteristic lines in the PiPiCo plot. In the analysis algorithm, coincident particles are distinguished by the sum of their momenta, which is 0 for fragments originated from the same parent ion.

For the presented measurement one obtains the graph depicted in figure 11.3(a). Several coincidences can be identified. The most prominent line represents N^+ measured in coincidence with NO^+ , and N_2^+ measured in coincidence with O^+ . In a magnified view (see figure 11.3(b)) of the respective TOF regime it is possible to distinguish both lines of the different dissociation channels. A second coincidence line at higher TOFs represents two N_2O^+ ions measured in coincidence. This line originates from the dissociation of a doubly-charged nitrous oxide dimer. Finally, a third coincidence line is visible, which is related to the fragmentation of water from the residual gas and from the jet into H^+ and OH^+ .

In summary, we are able to distinguish seven different reaction channels (excluding the dimer). The first and most prominent one is single ionization of N_2O^+ , in which the

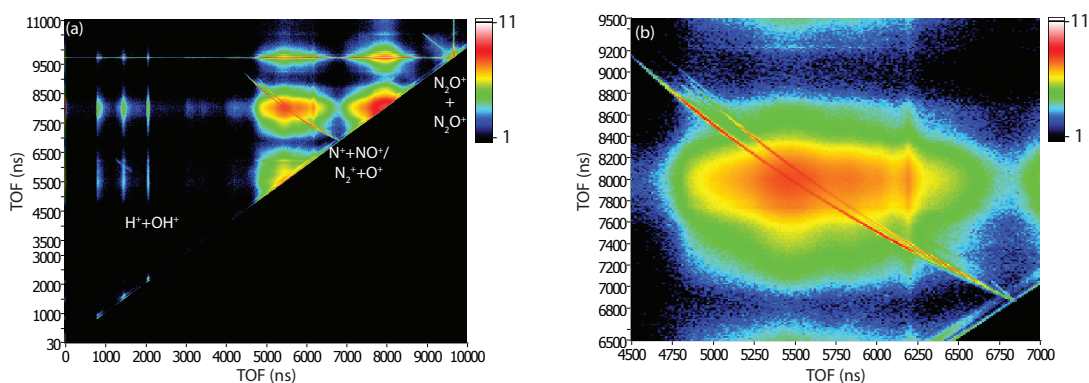


Figure 11.3: (a) PiPiCo spectrum for all time-of-flights and for all events of the presented measurement and (b) detailed view at the time-of-flights of N^+ , O^+ , N_2^+ , and NO^+ .

produced ion is stable within the TOF. In addition, the singly-ionized parent ion can dissociate into a charged fragment and a neutral fragment, representing four different reaction channels. Finally, the nitrous oxide can actually be doubly ionized. The doubly charged ions have a life time much shorter than the TOF, consequentially they dissociate via Coulomb explosion into two charged fragments.

In addition, the analysis of the experimental data presented in the following sections requires carefully adapted parameters for the reconstruction of the momenta. A short reference measurement was performed using argon as target gas and using the same experimental settings. This can be used for a first adjustment of the free parameters of the reconstruction of the momenta, since argon was frequently studied at our setup. Thereafter, the parameters are adapted to the data measured in N_2O as described in section 7.2.3. Figure 7.18 depicts several examples from the presented measurement, which are indicating the appropriate setting of the respective parameters.

12 Single Ionization of N_2O^+

As already mentioned, the singly-ionized nitrous oxide can either be detected directly or it can dissociate into a charged and a neutral fragment. If a stable N_2O^+ is produced or not is dependent on the state, to which the ion is excited during ionization [124].

12.1 N_2O^+ in Coincidence with an Electron

To study this reaction channel, only the produced N_2O^+ -ions are selected in the TOF spectrum and electrons that are measured in coincidence are investigated. Regarding the photoelectron energy spectrum, which is shown in figure 12.4(a), a clear peak structure is visible. All peaks, except for the first one with the lowest energy, are spaced by twice the photon energy of the fundamental IR laser. This is a clear evidence that the peak structure is produced mainly by the harmonics ionizing a single state, or several states that are spaced in energy close to an integer multiple of twice the IR photon energy.

There are mainly two states of the cation that come into consideration, namely the ground state X^2II and the first excited state $A^2\Sigma^+$ [125], since higher states do not result in stable N_2O^+ ions [124]. In order to identify the state, the photoelectron energy spectrum can be compared with the XUV spectrum measured in the XUV spectrometer (see figure 9.5). The energy difference between both spectra equates to the ionization potential I_p . However, it is ambiguous, which harmonic corresponds to which photoelectron-energy peak. Depending on the choice the difference is either 12.7 ± 0.3 eV or 15.8 ± 0.2 eV. The first value agrees with the ionization potential of the ground state (12.89 eV), whereas the latter value deviates from the I_p of the first excited state (16.38 eV), albeit slightly. This is an indication, that mainly the X^2II state is populated, whereas the contribution of the $A^2\Sigma^+$ state may be covered. On the one hand, the yield of stable N_2O^+ observed from the $A^2\Sigma^+$ band is significantly smaller than from the ground state [125]. On the other hand, the respective peak positions would only be shifted by approximately 0.3 eV towards lower energies, which leads to a superposition of the contribution of both states.

12.1.1 Delay-Dependent Effects

The electron energies are also available as a function of the delay between pump- and probe-pulse. This is depicted in figure 12.5. Around the temporal overlap of both pulses, the spectrum shows a time-dependent behavior. Figure 12.5 also shows projections of

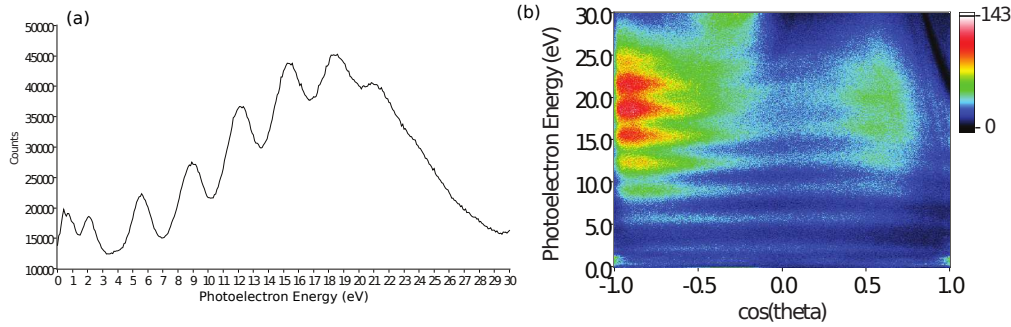


Figure 12.4: (a) Energy of the electrons measured in coincidence with N_2O^+ . (b) Energy of the electrons as function of $\cos(\theta)$, with θ being the angle between laser-polarization axis and the respective momentum vector. It can be seen, that at high photoelectron energies and at positive values of $\cos(\theta)$, the energy spectrum is affected by the “node” due to the cyclotron motion of the electron (see figure 7.17).

narrow windows in the electron energy as indicated in the figure onto the delay-axis. One trace is at a peak position and the second one is in between two peaks. In the overlap, the signal decreases for the window at the peak position, whereas the other signal increases simultaneously.

This effect can be explained by the production of sidebands (compare section 3.5). In the case, an additional IR field is present during the ionization process via harmonic radiation, the freed electrons can absorb or emit an additional photon of the IR field. As a result, the sidebands are formed right in between two peaks of the mainbands, whereas the missing electrons in the mainbands lead to a decrease of the signal.

As introduced in section 3.5, the production of the sidebands is a cross-correlation of the IR and the XUV pulse. Thus the pulse durations of the involved pulses can be estimated with equation (3.86). For every side- and mainband a cross-correlation spectrum (as shown in figure 12.5) was produced and a Gaussian pulse was fitted to the data in order to achieve the FWHM of the sideband signal. The averaged FWHM of the sideband signal is 32 ± 3 fs. From the experience of different work groups the length of the attosecond pulse train can be approximated by $\tau_{XUV} = 0.65\tau_{IR}$ [74, 126]. Therewith, the pulse durations can be estimated as $\tau_{IR} = 25 \pm 2$ fs and $\tau_{XUV} = 16.3 \pm 1.3$ fs. The peak position of the Gaussian fit functions can be used, to determine the exact position of the temporal overlap.

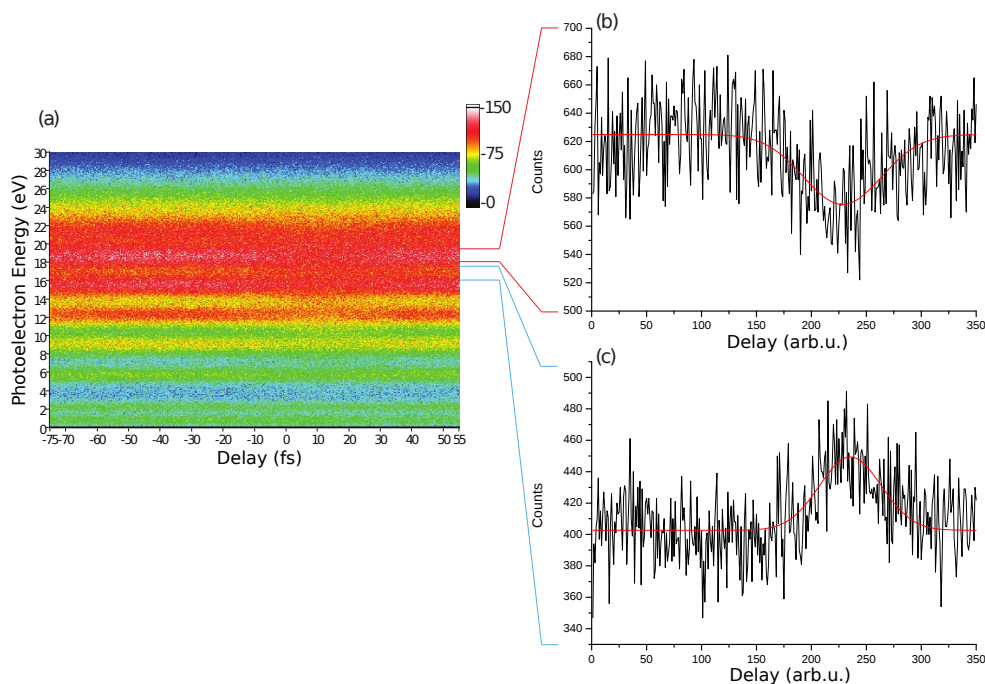


Figure 12.5: (a) Energy of the electrons measured in coincidence with N_2O^+ as function of the delay. (b) and (c) are showing projections of the marked energy windows onto the delay axis. In (b) the projection of a mainband is plotted, in which the counts decrease around the overlap of the two pulses. (c) shows a projection of a sideband, at which the signal is enhanced during the overlap.

12.2 Dissociation into a Charged and a Neutral Fragment

The singly ionized N_2O^+ ion is not necessarily stable. Dependent on which state the molecule is excited in, it dissociates into a charged and a neutral fragment. As mechanism mainly the predissociation of the respective state and the subsequent interaction with repulsive potential curves is proposed [127]. We observe all possible channels:



The TOF spectrum (see figure 11.2) reveals that NO^+ and N_2^+ , as well as N^+ and O^+ are not distinguishable in our experiment by the time-of-flight alone. The TOF windows for the different ion species are set for the analysis as indicated with the colored dotted lines in figure 11.2. Additionally, the neutral fragment cannot be measured in the ReMi. Therefore, it is not possible to separate the channels by momentum sums. However, a plot, in which the transversal momentum is charted as function of the longitudinal momentum for all particles (see figure 12.6), indicates that it is possible to discriminate to some degree between the individual charged particles by restricting the considered 2-D momenta to smaller windows, indicated by the white lines in figure 12.6.

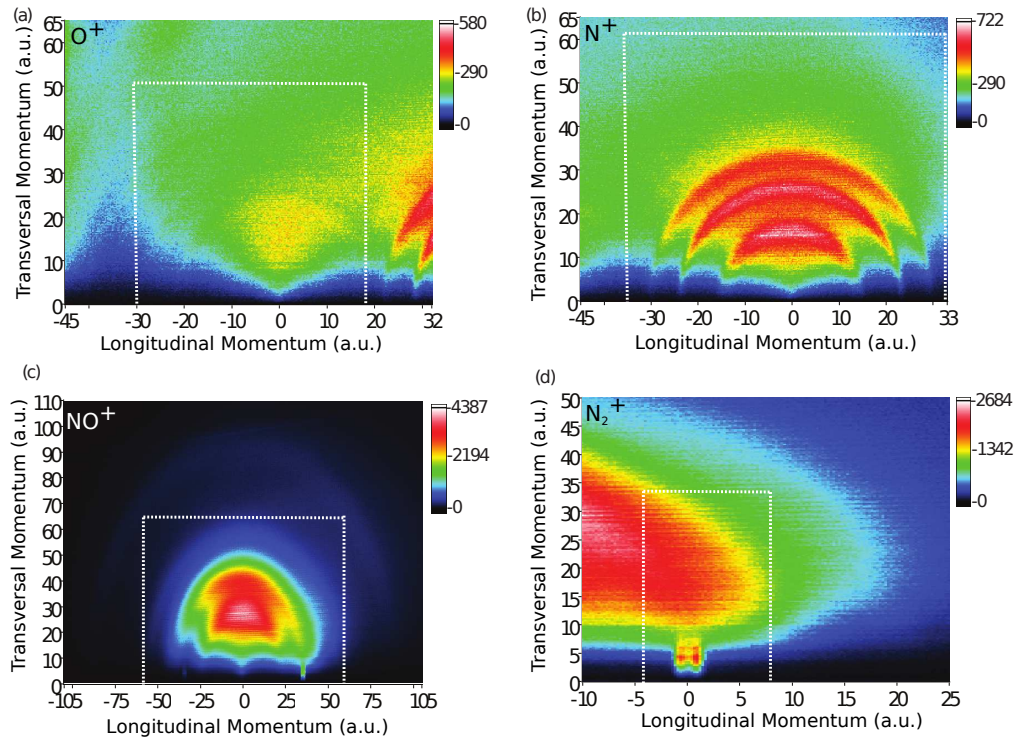


Figure 12.6: The transversal momentum p_r as function of the longitudinal momentum p_z for (a) O^+ , (b) N^+ , (c) NO^+ , and (d) N_2^+ . The momentum distributions of the different ions are overlapping. The white dotted lines depict the area, which was respectively selected to determine the branching ratios of the dissociating channels.

In addition, the measured charged fragments originate not only from the fragmentation of the singly but also from the dissociation of the doubly charged ion. As it will be shown, both can be distinguished by the absolute value of the transversal momentum. The ions

created during the dissociation of the singly-charged ion has low transversal momenta, whereas the Coulomb explosion of the doubly-charged ion leads to higher momenta.

12.2.1 Branching Ratios

In figure 12.6 it is conspicuous that the different ions are produced with different probabilities. To extract the branching ratios of the individual ions, they are separated as described previously and the resulting distributions were integrated in order to gain the number of measured particles. In the case of NO^+ and N_2^+ , the contribution of both channels are partially overlapping (see figure 12.6 (c)). As indicated with the white dashed lines in figure 12.6 (d), there are additional N_2^+ with higher momenta (compared to the distribution at transversal momenta below 10 a.u. and longitudinal momenta between -1.5 a.u. and 1.5 a.u.), which are only barely visible in this illustration (figure 12.6 (c) and (d)). Nevertheless, the N_2^+ events are estimated as the integral over the area within the white dashed lines shown in figure 12.6 (d), and these are subtracted from the framed region in figure 12.6 (c) (which includes all N_2^+ events) in order to gain the count number of the NO^+ solely.

The sum over the counts of all four channels is the total number of counts (100 %). Most likely, NO^+ is produced (75.7 %), followed by N_2^+ (10.7 %), N^+ (10.0 %), and O^+ (3.6 %). Due to the poor distinctness between the individual channels (especially the NO^+ and N_2^+ channels), the results are connotated with an unpredictable error. Nevertheless, the measured branching ratios reproduce previous results [125, 127, 128], although the quoted references are selectively exciting the $C^2\Sigma^+$ state, which is not possible in our experiment.

The dissociation of the singly charged nitrous oxide ion occurs most likely by breaking the $N - N$ bond (in approximately 86 % of all events).

12.2.2 Ion Kinetic Energy Release

The kinetic energy release (KER) of the ions may provide some information about the fragmentation process they originate from. In order to be able to distinguish between the different ion species, the longitudinal momentum is restricted as depicted in figure 12.6, whereas the transversal momentum is not confined, lest a part of “good” events is cut out in order to filter out events coming from the dissociation of the doubly-charged ion. Their portion of the number of events is small compared to the contribution of the dissociation

of the singly charged ion.

The ions generated in the charged-neutral fragmentation have low KERs, which are depicted in figure 12.7. All four KER distributions have a peak below 0.5 eV. Especially remarkable are the KERs of N^+ and NO^+ . The N^+ -KER reveals a triple-peak structure. It indicates that the nitrous oxide cation dissociates from the $N_2O^+(C^2\Sigma^+)$ state, in which vibronic states are excited. The lowest energetic peak at 95 meV corresponds to the vibrational ground state, the second one at 250 meV can be assigned to a symmetric stretching mode and the third peak at 385 meV to an asymmetric stretching mode [129]. The energy spacing measured is 155 meV between the first and the second peak and 135 meV between the second and the third peak. These results are comparable to other experiments, in which the energy spacing was determined as 160 meV for the spacing between the first two peaks and 130 meV between the second and the third peak [124, 127–129].

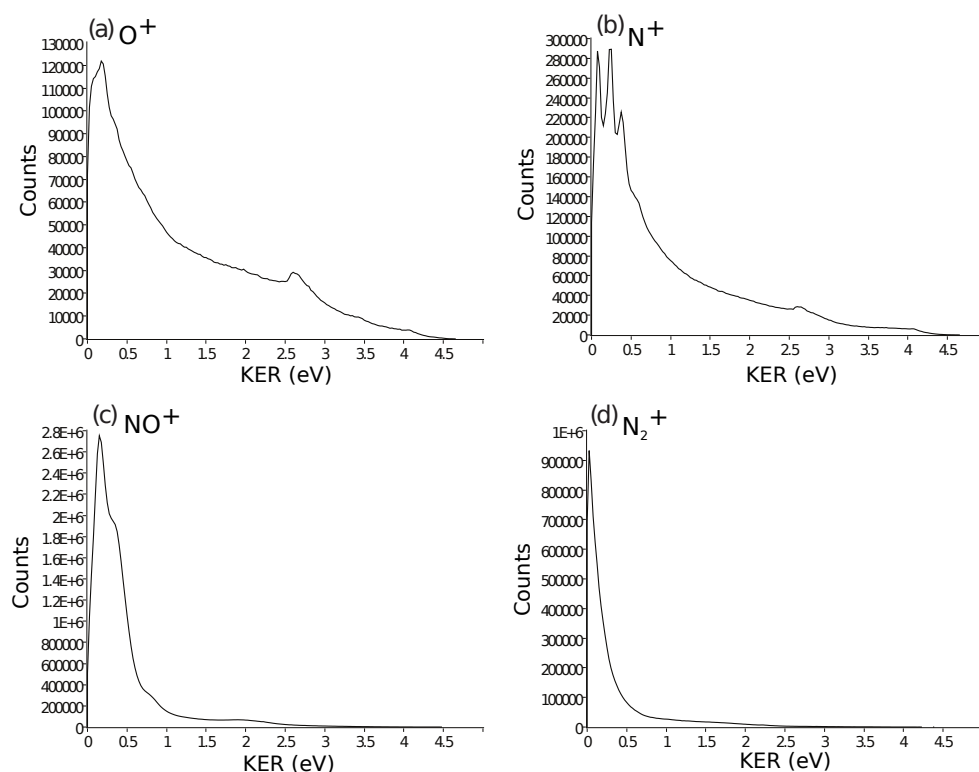


Figure 12.7: The KER distributions for (a) O^+ , (b) N^+ , (c) NO^+ , and (d) N_2^+ .

In the KER of NO^+ also a structure is visible. From figure 12.6(c) one can see that two peaks are superimposed. The first peak has its maximum at 195 meV and the second one,

which is considerably broader, at ~ 420 meV. This double-peak structure has a different origin as the structure in the N^+ -KER. This becomes clearer by looking at the energy of the electrons measured in coincidence with the ions at the respective energy. Figure 12.8 shows the KER as function of the electron energy and two projections onto the electron-energy axis at the KER of the first peak position and at 0.5 eV. Both photoelectron spectra show clear signatures of the harmonic radiation, similar to the photoelectron spectrum of N_2O^+ (see section 12.1), but the two spectra are shifted with respect to each other. This is providing evidence that the N_2O^+ dissociates from two different excited states.

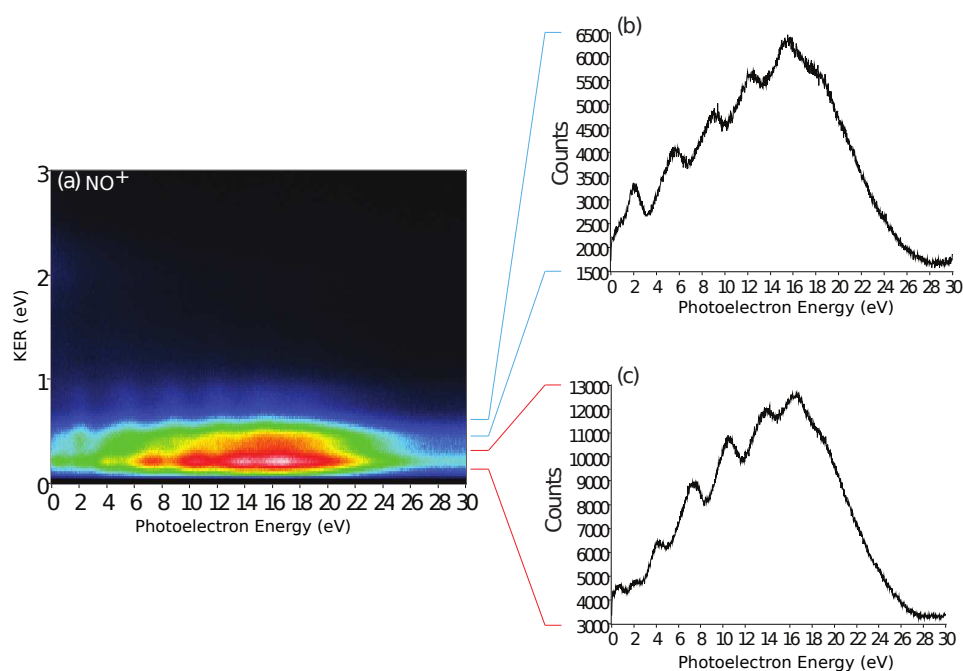


Figure 12.8: (a) The KER distribution as function of the respective photoelectron energy of NO^+ and a projection at a KER of (b) 500 meV and (c) 150 meV onto the photoelectron energy axis.

To identify the involved states, the photoelectron spectrum can be compared to the XUV spectrum, but again it is ambiguous, which photoelectron peak corresponds to which harmonic order. Therefore, several possible combinations are compared.

For the electron energies at low KERs, one obtains 11.17 ± 0.20 eV, 14.37 ± 0.17 eV, 17.59 ± 0.14 eV, or 20.81 ± 0.11 eV as possible differences between the XUV and the photoelectron energies. The differences correspond again to the ionization potential of the

respective state. Therefore, the lowest one at 11.17 eV can be excluded, since the threshold for the production of NO^+ is at 14.19 eV. Nevertheless, the other three options can be assigned to certain states, which dissociate into $NO^+ + N$, namely the ground state $X^2\Pi$ at 14.19 eV, the second excited state $B^2\Pi$ at 17.77 eV and the third excited state $C^2\Sigma^+$ at 20.60 eV [130]. However, it is not possible to determine if only one of these states or all three are involved in the ionization, but it was found in [131] that the dissociation via the $B^2\Pi$ state is the dominant channel.

Analogously, the photoelectron-energy spectrum at the higher KERs is analyzed. Here, the possible energy differences are 12.84 ± 0.09 eV, 16.11 ± 0.06 eV, 19.39 ± 0.09 eV, and 22.59 ± 0.13 eV. In this case, only two different states have similar ionization potentials: the first excited state $A^2\Sigma^+$ at 16.57 eV and again the third excited state $C^2\Sigma^+$ at 22.50 eV [130]. The agreement with the ionization potential of the $C^2\Sigma^+$ state is very good, whereas for the $A^2\Sigma^+$ state the result deviates by approximately 0.5 eV. This indicates that for the dissociation, resulting in ions with a higher KER, may now occur from the $C^2\Sigma^+$ state.

12.2.3 Delay-Dependent Effects

Figure 12.9 shows the yield of the fragmentation events for all channels as function of the time delay between XUV-pump and IR-probe pulse. Here, only events with KERs below 1.5 eV are taken into account, in order to concentrate on the ionization yield of the charged-neutral-dissociation. All channels are showing a time dependence. The atomic-ion dissociation channels (figure 12.9(a) and (b)) display a very distinct decrease of the ionization yield during the overlap of both pulses. The yield of the molecular ions (figure 12.9(c) and (d)) drops less or even not at all (N_2^+) at the overlap, whereas the signal slightly increases at positive delays.

However, if not only the low-KER particles are chosen (and thus taking in addition the fragments into account that arose from the dissociation of the doubly-charged ion), the time dependence vanishes. This is an indication for enhancement of the double ionization in the temporal overlap of XUV and IR pulse at the expense of the charged-neutral particle dissociation.

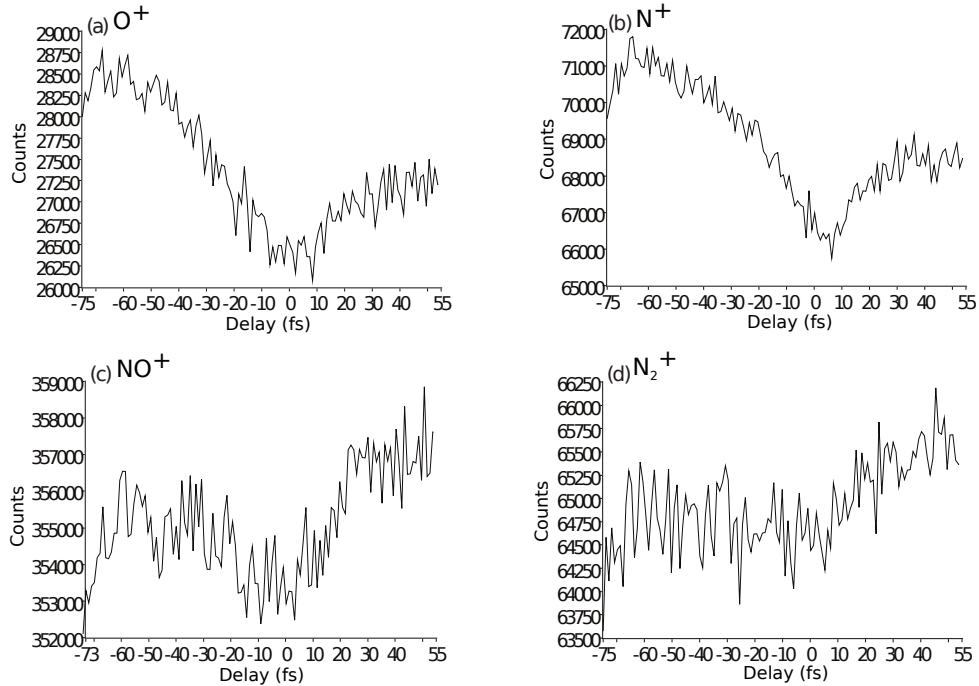


Figure 12.9: The ionization yield as function of the time delay for (a) O^+ , (b) N^+ , (c) NO^+ , and (d) N_2^+ .

13 Double Ionization of N_2O

Although the doubly-charged cation N_2O^{2+} is not directly measured, the PiPiCo map (see figure 11.3) gives a clear evidence that it is produced. Due to its short lifetime of a few hundred ns [132] and a TOF in the order of ~ 7 ps for the dication, only its fragments are detected, namely $N^+ + NO^+$ or $N_2^+ + O^+$. The highest photon energies in our HHG spectrum (see figure 9.5) are sufficient in order to directly doubly ionize the molecule. The double-ionization threshold is at 35.8 eV [119, 123]. Figure 13.10 depicts a subset of the potential energy curves (PECs) of N_2O^{2+} for the dissociation of both bonds taken from [123] and [133]. As it will be shown later, similar to the dissociation of the singly-charged cation, the breaking of the $N - N$ bond is more likely than the breaking of the $N - O$ bond. One reason is revealed in the PECs. The incoming XUV-beam excites the molecule within the Frank-Condon region. Then, most PEC of the $N - N$ bond breaking channel are dissociative, whereas there are only two at high energies for the $N - O$ bond breaking

channel.

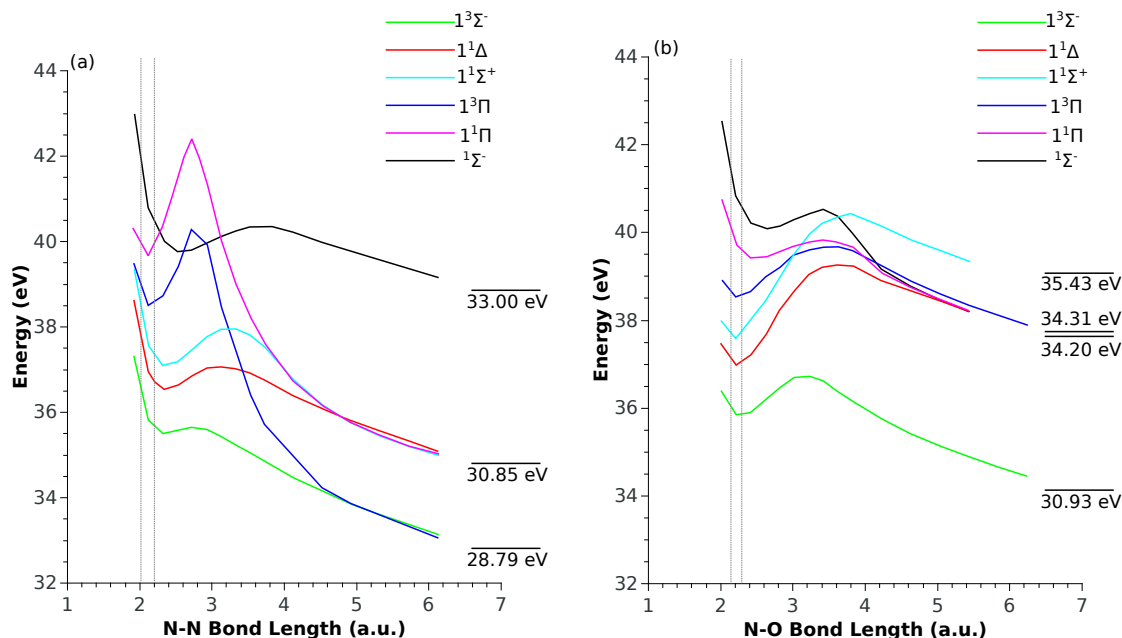


Figure 13.10: Potential energy curves of N_2O^{2+} from [123]. The colored lines depict different states and the vertical dotted gray lines indicate the Frank-Condon region for (a) the breaking of the $N - N$ bond and (b) the breaking of the $N - O$ bond. The horizontal black lines represent the dissociation limits at the declared energies of the respective states.

It also has been shown in [119], that an excitation above 38.5 eV leads to a metastable dication, which radiatively decays into the dication ground state $X^3\Sigma^-$. If the ground state is populated directly by excitation, it dissociates fast into $N^+ + NO^+$ or $N_2^+ + O^+$ with a ratio of 4 : 1. Whereas, if the ground state is populated by the decay of the metastable state, the bonds had enough time to rearrange, which leads to a dissociation into $N^+ + NO^+$ only [119]. In addition to the direct double ionization, another competitive channel was proposed in [120]. Here, the XUV pulse singly ionizes the nitrous oxide molecule, leaving it in a doubly-excited state above the double-ionization threshold. This singly ionized and highly excited molecule (N_2O^{+*}) can either dissociate, as presented, in a neutral and a charged fragment, or an autoionization process may occur, in which a second electron is released via Auger decay. It was also shown in [24] that the autoionization may occur even if the molecule is excited below the double-ionization threshold.

13.1 KER

Figure 13.11(a) and (b) show the KER for the two possible dissociations channels. The peak of the $N_2^+ + O^+$ -channel KER distribution is at 5.3 eV, which is comparable to the expected KER emerging from the $X^3\Sigma^-$ ground state, namely 4.9 eV [119, 123]. The KER distribution of the $N - N$ bond breaking channel exhibits a double-peak structure. The higher energetic peak lies at 6.6 eV, whereas the other peak is located at 6.0 eV. The double-peak structure can be caused by the superposition of the contribution of several dissociating states, which are resulting in similar KERs. There are mainly three dissociating states that are accessible with our photon energies: the dication ground state $X^3\Sigma^-$ with a KER of approximately 7 eV, the $^1\Sigma^+$ - and the $^1\Delta$ state, which both have the same dissociation limit but slightly different initial energies within the Frank-Condon region, leading to a KER of 6.2 eV and 6.7 eV, respectively [119, 123].

In addition, 13.11(c) and (d) depict the KER as function of the photoelectron energy E_e . Here, diagonal structures leading from a specific KER to the same absolute value of E_e would indicate the contribution of a particular electronic state to the dissociation, at which the diagonal structures are caused by the sharing of a certain XUV-photon energy between the respective electrons and ions. Both channels showing a tiny indication for such diagonals. In the $N^+ + NO^+$ channel it is barely visible. In the $N_2^+ + O^+$ channel some diagonals may appear near a KER of 8 eV and the main feature of this graph at a KER of 6 eV and $E_e < 2$ eV is possibly aligned on a diagonal. Mainly the fact that the photon energies hardly exceed the double-ionization threshold and that several states are energetically close-lying (see figure 13.10) leads to small electron energies and, thus, to short traces on the diagonal lines, that they might not be identifiable as such.

The branching ratio between the $N - N$ - and the $N - O$ -bond-breaking channels is in the order of 2 : 1, and not as expected, 4 : 1 [119], or 2.6 : 1 [120, 133, 134]. This can be explained by the broad photon-energy spectrum of the XUV pulses including energies below the double ionization threshold. It was shown that the branching ratio depends on the photon energy [24]. Below the double ionization threshold, the branching ratio increases with increasing photon energy. In this energy regime the double ionization is mainly caused by the autoionization of the highly excited N_2O^{+*} . The KER of the fragments after autoionization was measured at a photon energy of 35 eV in [24] as approximately 4.7 eV for the $N - N$, and 2.3 eV for the $N - O$ bond-breaking channel. For the dissociation of the $N - N$ bond, the KER of the autoionization overlaps at the low-energetic edge of

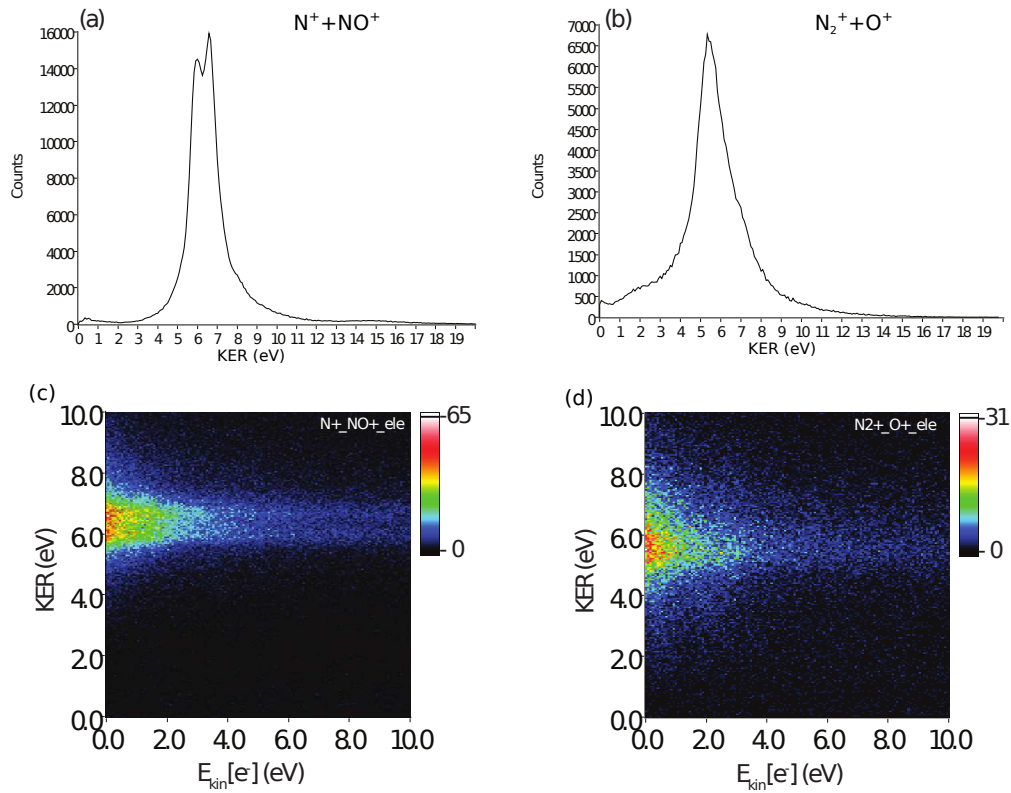


Figure 13.11: The KER distributions for the two dissociation channels: (a) $N^+ + NO^+$, (b) $N_2^+ + O^+$. And the KER distributions of (c) $N^+ + NO^+$ and (d) $N_2^+ + O^+$ as function of the respective photoelectron energy.

the KER distribution measured here, whereas it explains the increased signal in the KER around 2 eV in the second dissociation channel.

13.2 Delay Dependent Effects

Especially in the dissociation of the doubly-charged nitrous oxide, it is interesting to observe, which influence the IR-probe pulse has on the fragmentation process. First, the total number of events will be shown as function of the time delay between both pulses and compared to each other. Thereafter, both KER distributions will be presented as well as function of the time delay.

13.2.1 Counts as Function of the Delay

In figure 13.12(a) the counts of both channels are charted versus the delay. Obviously, the production of the doubly charged cation is enhanced when pump and probe pulses are overlapping. This behavior can have several reasons. In the overlap of both pulses, the molecule is able to absorb one or more IR photons in addition to an XUV photon. Therewith it is possible to exceed the double ionization threshold for XUV photons with slightly lower energy or it is possible to further excite an N_2O^{2+} from a metastable state into a higher energetic dissociative state. Regarding the case that a singly charged, excited molecule N_2O^{+*} is produced, the IR can easily ionize a second electron, and thus enhance the double ionization by avoiding the charged-neutral fragmentation of N_2O^{+*} , which is a competitive fragmentation channel to the autoionization process.

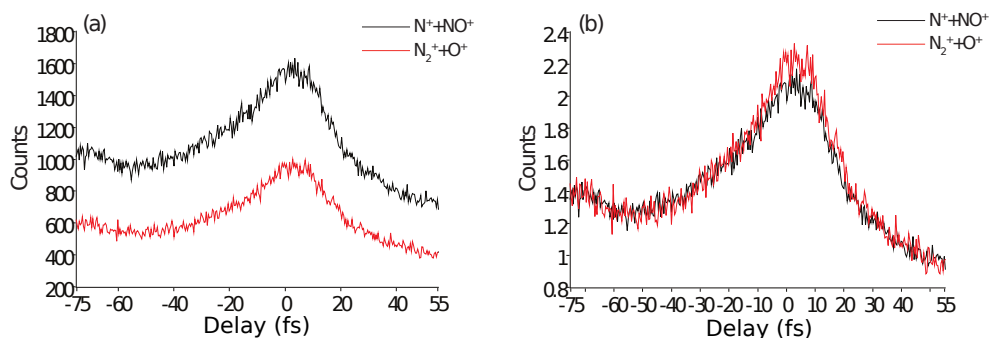


Figure 13.12: Dissociation yield of the doubly-charged nitrous oxide as function of the delay for both dissociating channels (a) as measured and (b) normalized to the averaged number of counts between 40 fs and 50 fs.

A second feature of the enhancement of the double ionization can be illustrated by comparing the two ionization yields, which are normalized to the averaged number of counts between 40 fs and 50 fs. The resulting graphs are plotted in figure 13.12(b). It can be noticed that the ionization yield of the $N - O$ bond-breaking channel is enhanced by a factor of 2.2, whereas the $N - N$ bond-breaking channel is enhanced by a factor of 2 only. This is an unexpected behavior, since in the energy regime between 35 and 40 eV, the $N - N$ bond breaking is the preferred dissociation channel [119, 120]. The enhancement of both channels is lower than in a similar measurement described in [120], in which the authors found an enhancement by a factor of 2 for the $N - N$ bond-breaking channel and a factor of 2.6 for the $N - O$ bond-breaking channel. The difference can be based on different experimental parameters, since we are using the entire XUV spectrum, whereas

in [120] only a small fraction around ~ 43 eV (bandwidth < 3 eV) was used. In addition, the intensities of pump and probe pulse certainly differ between the two experiments.

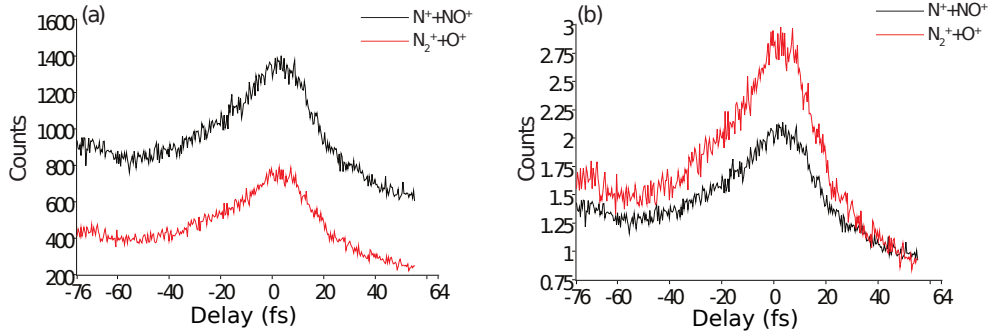


Figure 13.13: Yield of the dissociation of the doubly charged nitrous oxide, resulting in KERs above 4 eV, as function of the delay for both dissociating channels (a) as measured and (b) normalized to the averaged number of counts between 40 fs and 50 fs.

However, the main reason, why the total ionization of the $N_2^+ + O^+$ channel is less enhanced in our experiment as compared to [120], lies in the production of a higher fraction of KERs between 0 eV and 4 eV. As it will be illustrated in section 13.2.2, the low-energetic KERs seems to be reduced during the temporal overlap and enhanced at positive delays. If the ionization yield is observed for KERs above 4 eV only, the enhancement increases. This is depicted in figure 13.13, which shows the ionization yield of both dissociation channels for KERs above 4 eV. The $N - N$ bond-breaking channel remains unaffected, whereas the $N - O$ bond-breaking channel is enhanced by a factor of 2.8.

13.2.2 KER as Function of the Delay

The presence of the IR pulse influences the dissociation process and if it modifies the populated dissociative states, a change in the KER distribution can be expected. Figure 13.14 shows the KER, as well as its mean value, for both channels plotted as a function of the delay. Both channels are affected and again, the $N - O$ bond-breaking channel shows a more pronounced effect. This becomes even clearer, when both KER vs. delay plots are normalized. Figure 13.15 shows again the KER as function of the delay, but the KER is normalized to its maximum at every time step.

The KER increases when both pulses approach each other, whereas at higher positive delay values, more fragments with lower KERs are generated. Having a closer look to the low-energy KERs between 2 and 4 eV in the $N - O$ bond-breaking channel, at which

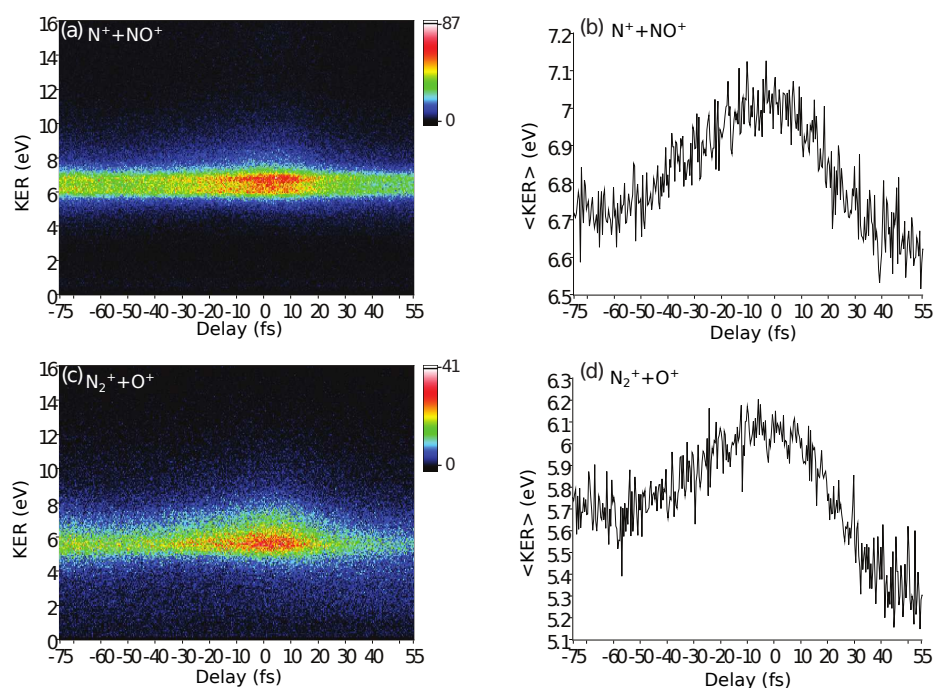


Figure 13.14: KER for (a) the $N - N$, and (c) for the $N - O$ bond-breaking dissociation channel as function of the time delay. (b) The average value of the KER of the $N^+ + NO^+$ dissociation as function of the time delay. (d) The same plot as (b) for the $N_2^+ + O^+$ dissociation.

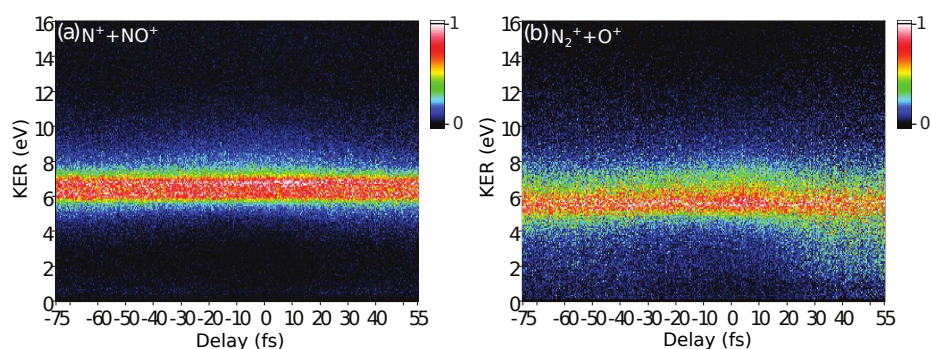


Figure 13.15: Normalized KER distributions for (a) the $N - N$, and (b) for the $N - O$ bond-breaking dissociation channel as function of the time delay, normalized to its maximum at every time step.

the fragments from the autoionization are expected, and making a projection onto the delay scale (see figure 13.16), a different behavior can be found as at the peak of the KER distribution, at which the yield increases during the overlap. At these autoionization KERs, the yield first slightly drops before it starts to increase near the overlap of both pulses and forming a plateau towards higher positive delays. Again, both channels are showing this behavior and in this case as well, the $N - O$ bond-breaking channel is more affected.

The delay-dependent behavior of the ionization yield for ions at low-energy KERs indicated that the IR field influences the autoionization. It was found that the autoionization is most efficient at positive delays. At these times, the XUV radiation ionizes the molecules after the IR pulses already passed the target area and the autoionization occurs unaffected. The drop of the yield at delay times, at which the IR field is present during and after the ionization, suggests that the probe pulse interrupts the autoionization by releasing the second electron via photoionization.

In addition, it is conspicuous that at the $N - N$ bond-breaking channel, the low-KER ion yield returns within the delay range (at approximately -65 fs) to the (unaffected) yield at positive delays (see figure 13.16(b)), whereas in the $N - O$ bond-breaking channel the number of counts is still reduced (see figure 13.16(d)). This is a sign that the lifetime of the N_2O^{+*} before autoionization is longer if the molecule dissociates into $N_2^+ + O^+$ than for the dissociation into $N^+ + NO^+$.

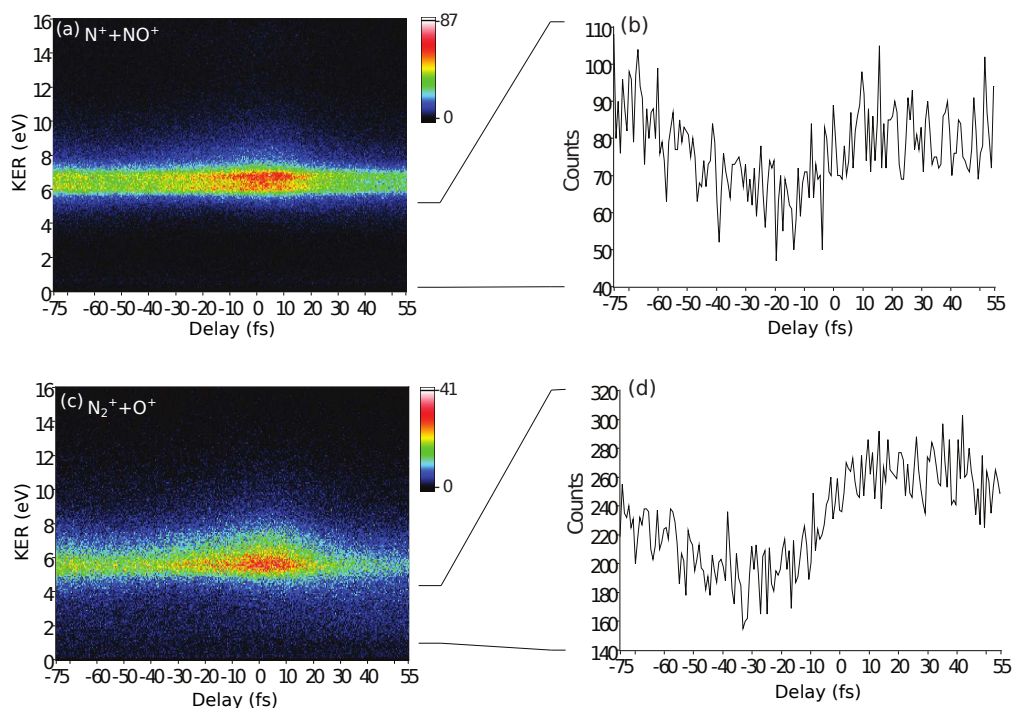


Figure 13.16: The KER distribution and a projection of the KER onto the delay axis for (a) and (b) the $N - N$, and (c) and (d) for the $N - O$ bond-breaking dissociation channel as function of the time delay.

13.3 Electron Energies

In addition to the ion KERs, we can also inspect the electron energies. Unfortunately, the acquisition electronics does currently not allow the measurement of more than one electron from one event, due to the short TOF- window of around 60 ns, in which the electrons arrive at the detector.

The photoelectron spectra measured in coincidence with the two charged fragments of the doubly-charged ion are shown in figure 13.17 for both dissociations channels. The spectrum is dominated by low-energy electrons, since our XUV photon energy barely exceeds the double-ionization threshold and the major part of the photon energy was spent to excite the molecule. In the photoelectron energy of the $N_2^+ + O^+ + e^-$ coincidence, a small indication of a peak structure is visible around 2.0 eV. For the analysis of this peak and to investigate if the $N^+ + NO^+ + e^-$ channel shows a similar structure, a function

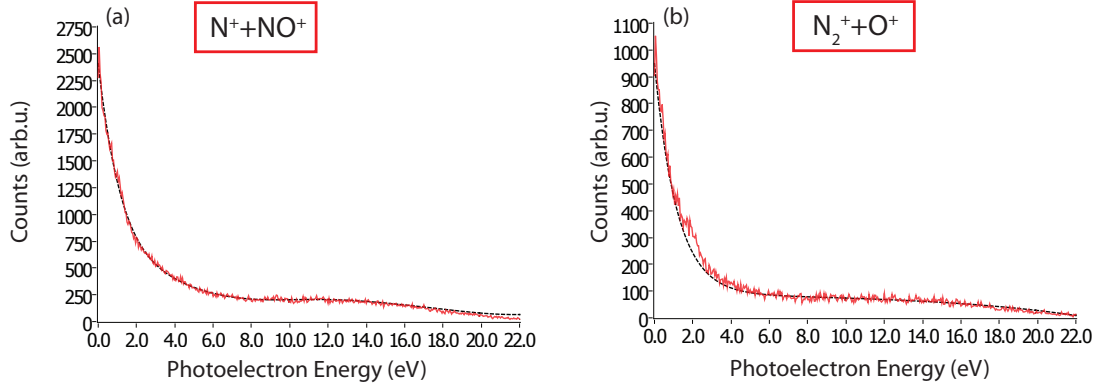


Figure 13.17: The photoelectron energy of (a) the $N-N$, and (b) the $N-O$ bond-breaking dissociation channel. The dashed black lines illustrate the fitted functions explained in the text.

is fitted into the respective data, which emulates the “regular” energy distribution. In order to gain the best agreement, two different fit functions were used for the different channels. For the $N_2^+ + O^+ + e^-$ coincidence, a sum over two exponential decay functions was chosen, namely

$$f(x) = y_0 + A_1 \exp \frac{-x}{E_1} + A_2 \exp \frac{-x}{E_2}, \quad (13.6)$$

in which y_0 is the y -axis intercept, A_1 and A_2 are amplitudes, and E_1 and E_2 are decay constants. For the $N^+ + NO^+ + e^-$ channel the best result is achieved by a polynomial function of the ninth order, given by

$$g(x) = \sum_{i=0}^9 a_i x^i, \quad (13.7)$$

in which a_i are representing constants. In both cases all constants are computed. The resulting fit functions are plotted as black dashed lines in figure 13.17. Then, both the fit functions and the energy spectra are normalized to their integral before the fitted curves are subtracted from the measured energy distributions in order to make the residuals better visible. Several electron energy spectra are shown for varying KERs, as well as for different sections of the delay and also for both, fixed KER and delay windows. The complete set of figures is shown at the end of this section in figures 13.18-13.23.

13.3.1 The $N^+ + NO^+ + e^-$ Channel

At first, the $N^+ + NO^+ + e^-$ channel is inspected, in which a potential photoelectron energy peak was not clearly visible in the raw spectra (see figure 13.17(a)). But already figure 13.18(a), which shows the residual as a function of the photoelectron energy after subtraction of the fitted “background” electron spectrum obtained as described before, averaged over all KERs and delays reveals an additional structure. A tiny peak structure with the maximum at 1.1 eV become visible.

In order to inspect a potential delay dependence, the delay range is divided into four 30 fs long parts and the respective energy spectra (which are shown in figure 13.18(a)-(e)) are averaged over that time window. The peak structure is barely distinguishable from the background. But there are indications that it is formed in the first three delay segments (from -70 fs to 20 fs) but disappears in the regime, in which the IR hits the target before the XUV arrives. Additionally, the structure is less pronounced at time delays between -40 fs to -10 fs.

Similar to the delay dependence, it is possible to look at the electron energies as a function of the KER of the respective ions (see figures 13.18(a),(f);13.19(a),(f);13.20(a),(f)). Here, the KER is divided into five segments of 2.5 eV between 0 and 12.5 eV. For low KERs, the photoelectron energy has not yet the low-energy contribution. Therefore, the graphs, in which the fit function is subtracted, are dropping down towards 0 eV. In the KER section from 5 eV to 7.5 eV, the peak appears clearly, whereas at higher and lower KERs the peaks dissolves.

Finally, the single KER segments can be broken down into the different delay sections. It emerges, that the peak is only visible in the KER regime between 5 eV and 7.5 eV (figures 13.19(f)-(j)). For delays between 20 fs to 50 fs, the peak cannot be distinguished from the background (see figure 13.19(j)). For all other delay times, the contribution is present but shows a minor dependence on the delay.

13.3.2 The $N_2^+ + O^+ + e^-$ Channel

For this channel, there are the same plots available as shown before. Regarding the energy graph, which is averaged over all KERs and time delays (figure 13.21(a)), there is one broad peak visible at 2 eV. It seems to be present for the time delays between 50 fs and -40 fs (see figures 13.21(b)-(e)), with its amplitude decreasing from the positive delay times towards negative values.

Regarding the KER dependence (see figures 13.21(a),(f);13.22(a),(f);13.23(a),(f)), it is obvious that the peak has its maximum between a KER of 2.5 eV and 5 eV (figure 13.22(a)) but it is present up to 10 eV of KER. In all KER segments, the delay dependence is comparable. The contribution is strongest at positive delay times while it decreases towards negative times (see figures 13.22(b)-(e) and (g)-(j), and figures 13.23(a)-(e)).

13.3.3 Conclusion

In both dissociation channels of the dication, apart from a broad energy spectrum with a strong maximum towards low energies an additional peak structure in the photoelectron energy can be deeply found when subtracting the continuum part. Obviously, these additional structures are more pronounced in the $N_2^+ + O^+ + e^-$ channel. But in both cases the peaks in the electron energy have their maximum at KERs of the ions slightly above the expected KERs from the autoionization process [24], namely 4.7 eV for the $N - N$ and 2.3 eV for the $N - O$ bond-breaking channel. This indicates that the electrons, which cause these peaks, originate from the autoionization process as described in [120]. Here, the XUV photons singly ionize the nitrous oxide and leaves it in a highly excited state N_2O^{+*} , which can either autonomously decay via an Auger-like process or the additional IR field can easily ionize a highly excited electron.

In the $N - N$ bond-breaking channel, the electrons from autoionization only emerge within a small range of the respective KER (~ 2.5 eV). Additionally, the delay between pump and probe pulse has only a minor influence on the electron yield. In contrast, for the dissociation into N_2^+ and O^+ , the autoionization can be found in a broader KER range (~ 7.5 eV) and it shows a higher electron yield at positive delay times. This also supports the results extracted from the ion yield spectra for the dissociation channels of the doubly charged cation, showing that the $N - O$ bond-breaking channel is more influenced by the additional IR field, than the other channel. In addition, it indicates again that the autoionization is interrupted by the probe pulse.

Unfortunately, the detailed interpretation of the electron spectra is hard and essentially impossible without sophisticated calculations at hand due to the superposition of electrons coming from both, the autoionization and direct double ionization. For a further, more detailed analysis of the energy spectra of electrons emitted within the autoionization process, it would be required to separate the different electrons in the detection system of the ReMi.

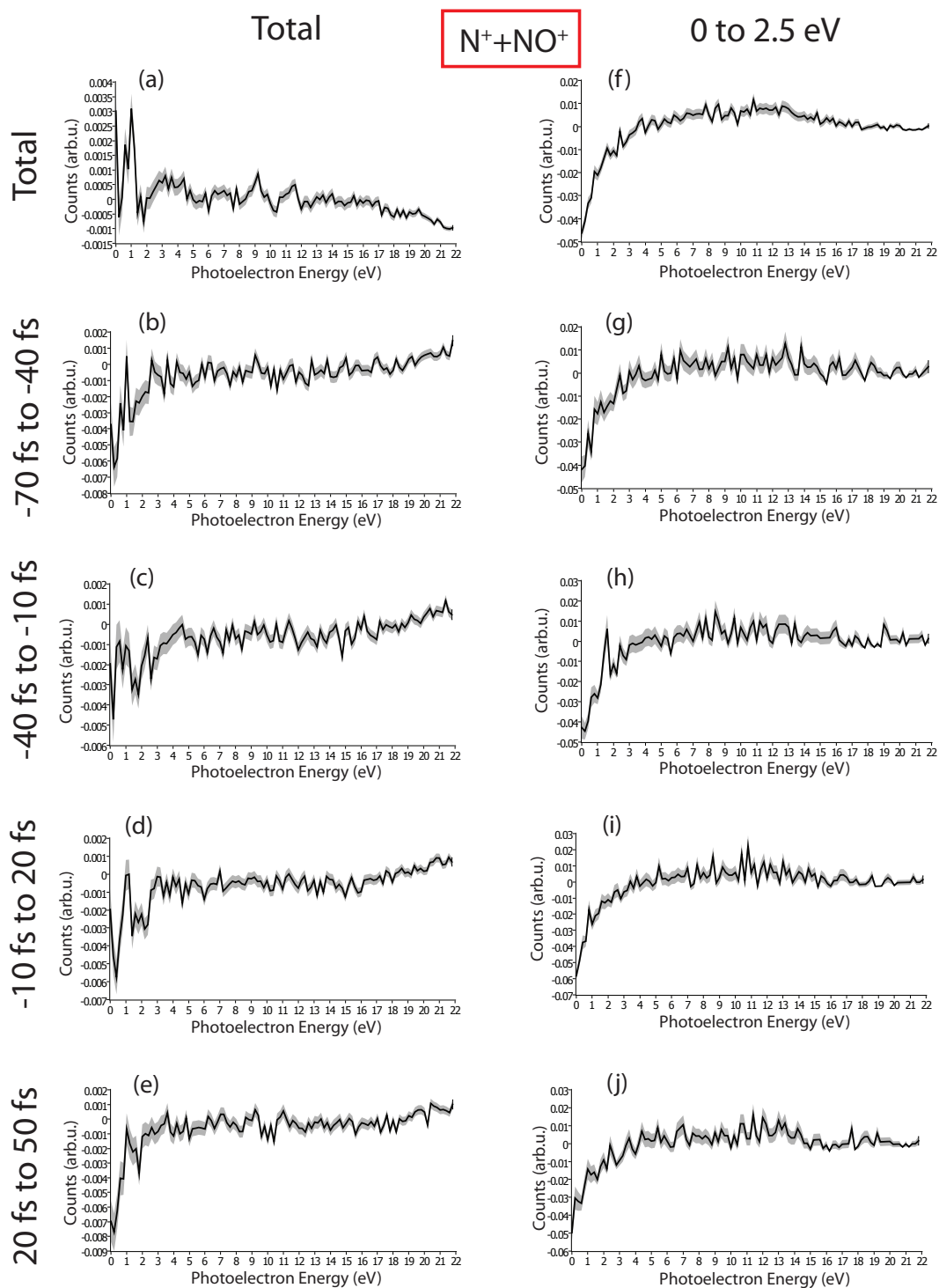


Figure 13.18: The photoelectron energy background subtracted as described in the text for different delays and different KERs of the $N^{++}NO^{+} + e^{-}$ coincidence. The gray area depicts the statistical error or the distribution.

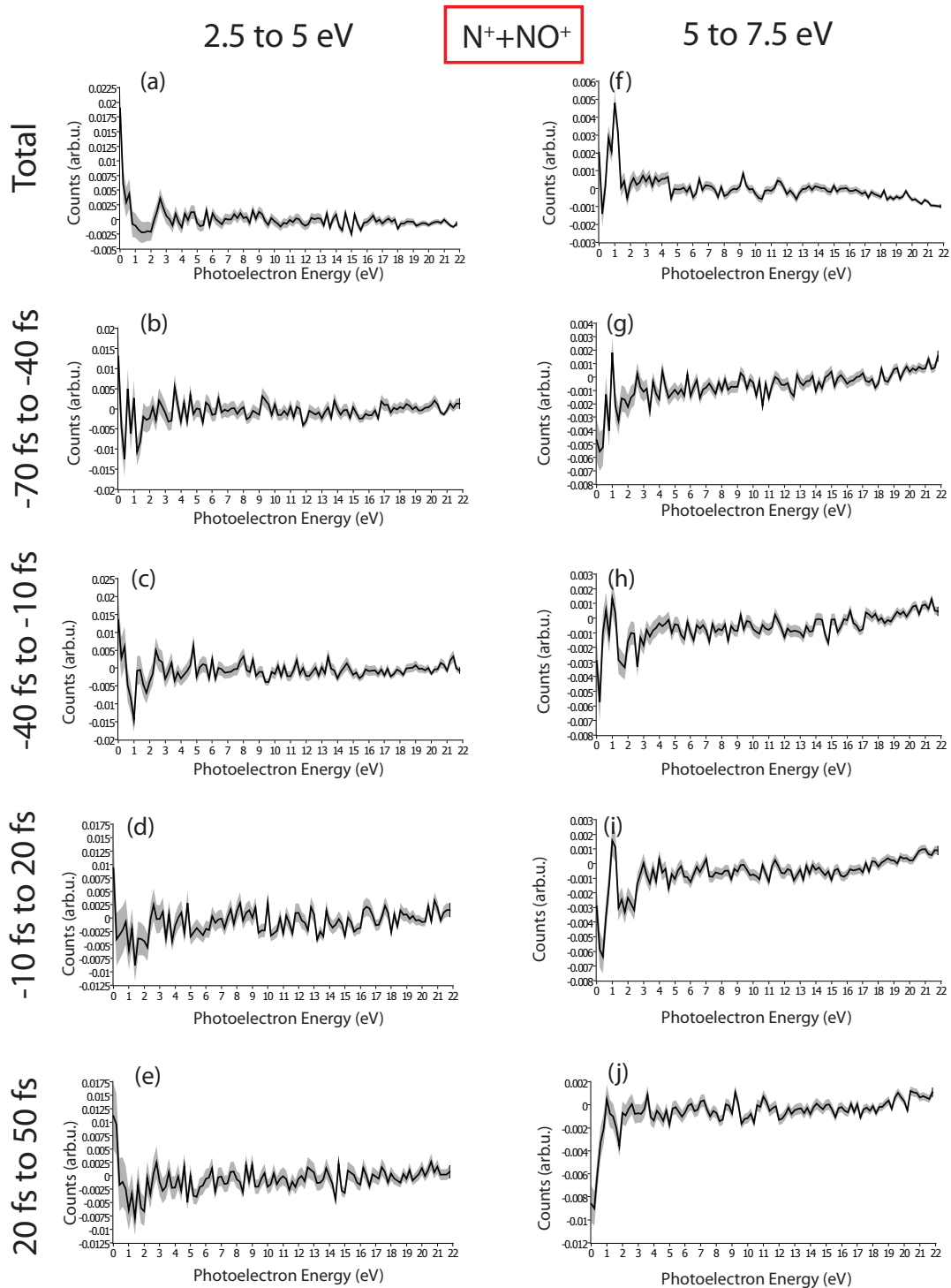


Figure 13.19: The photoelectron energy background subtracted as described in the text for different delays and different KERs of the $N^+ + NO^+ + e^-$ coincidence. The gray area depicts the statistical error or the distribution.

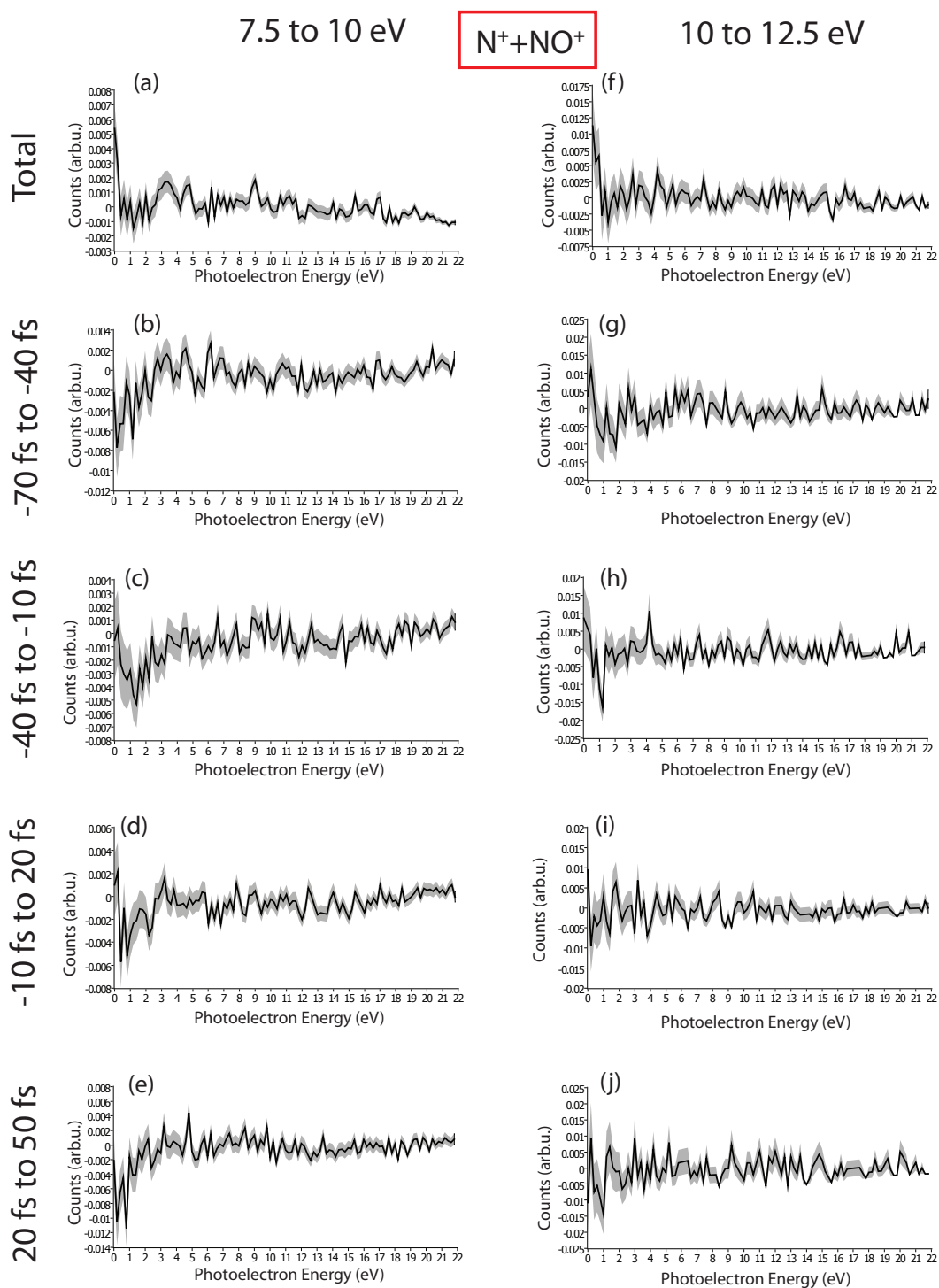


Figure 13.20: The photoelectron energy background subtracted as described in the text for different delays and different KERs of the $N^+ + NO^+ + e^-$ coincidence. The gray area depicts the statistical error or the distribution.

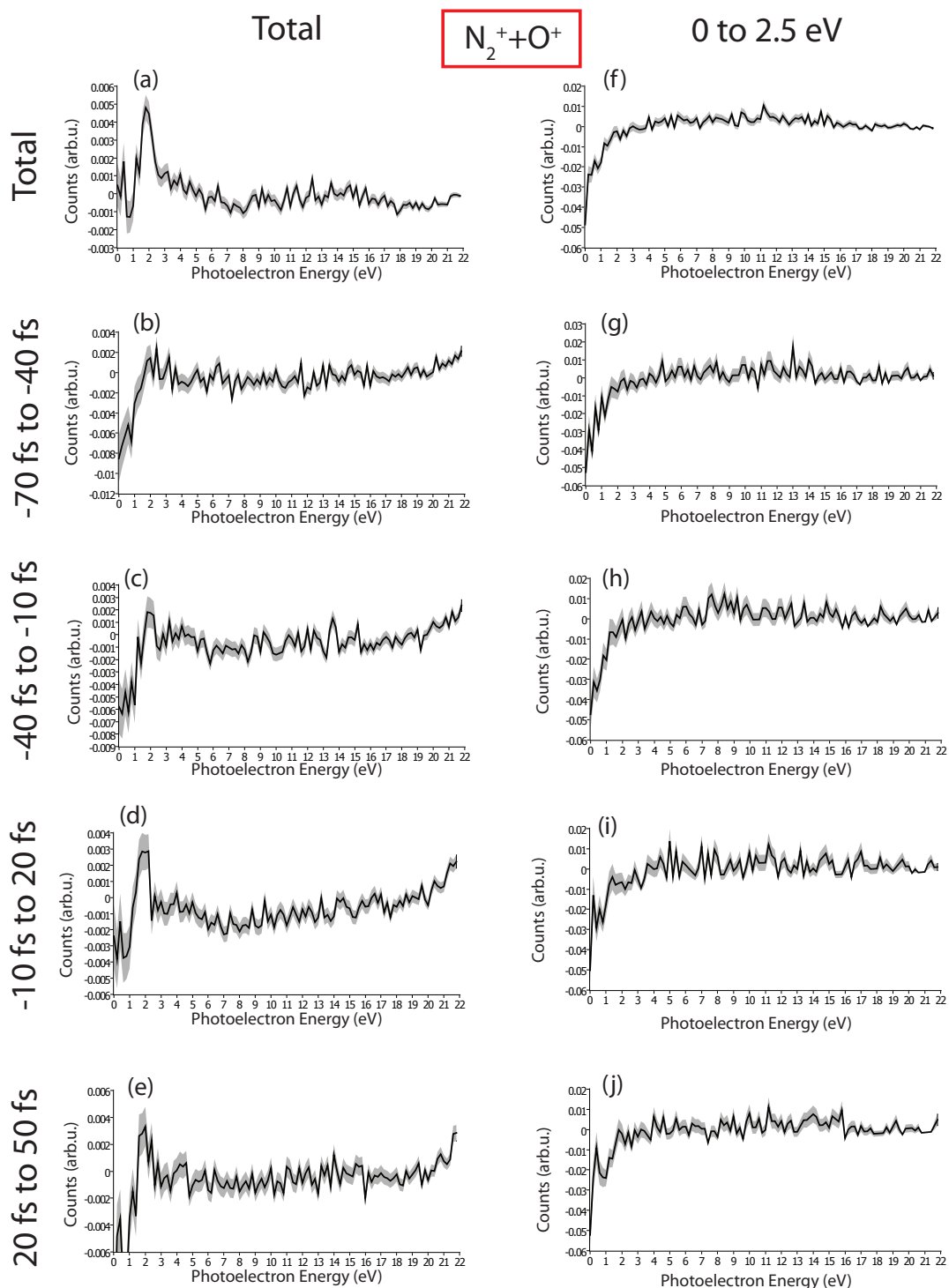


Figure 13.21: The photoelectron energy background subtracted as described in the text for different delays and different KERs of the $N_2^+ + O^+ + e^-$ coincidence. The gray area depicts the statistical error or the distribution.

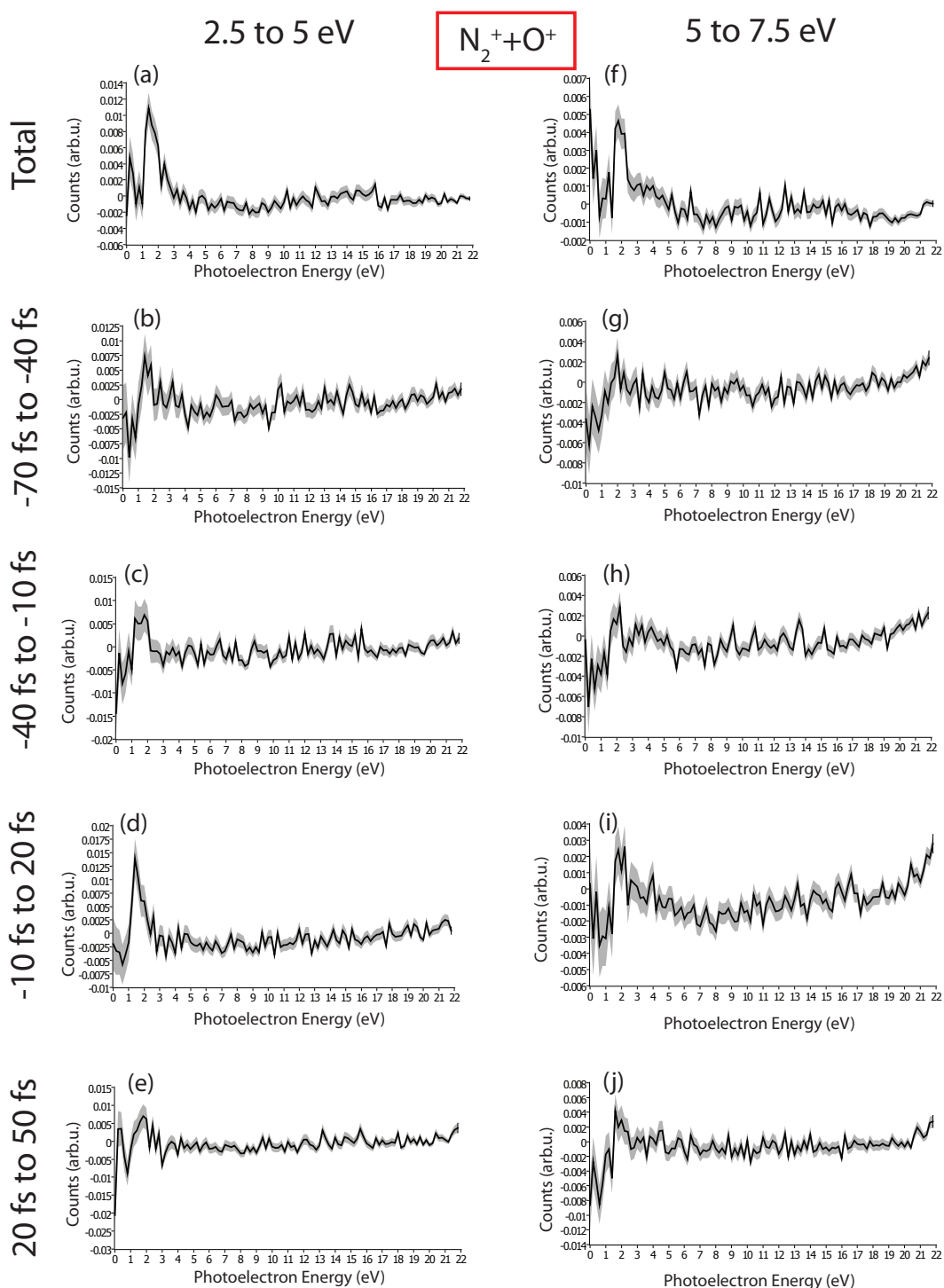


Figure 13.22: The photoelectron energy background subtracted as described in the text for different delays and different KERs of the $N_2^+ + O^+ + e^-$ coincidence. The gray area depicts the statistical error or the distribution.

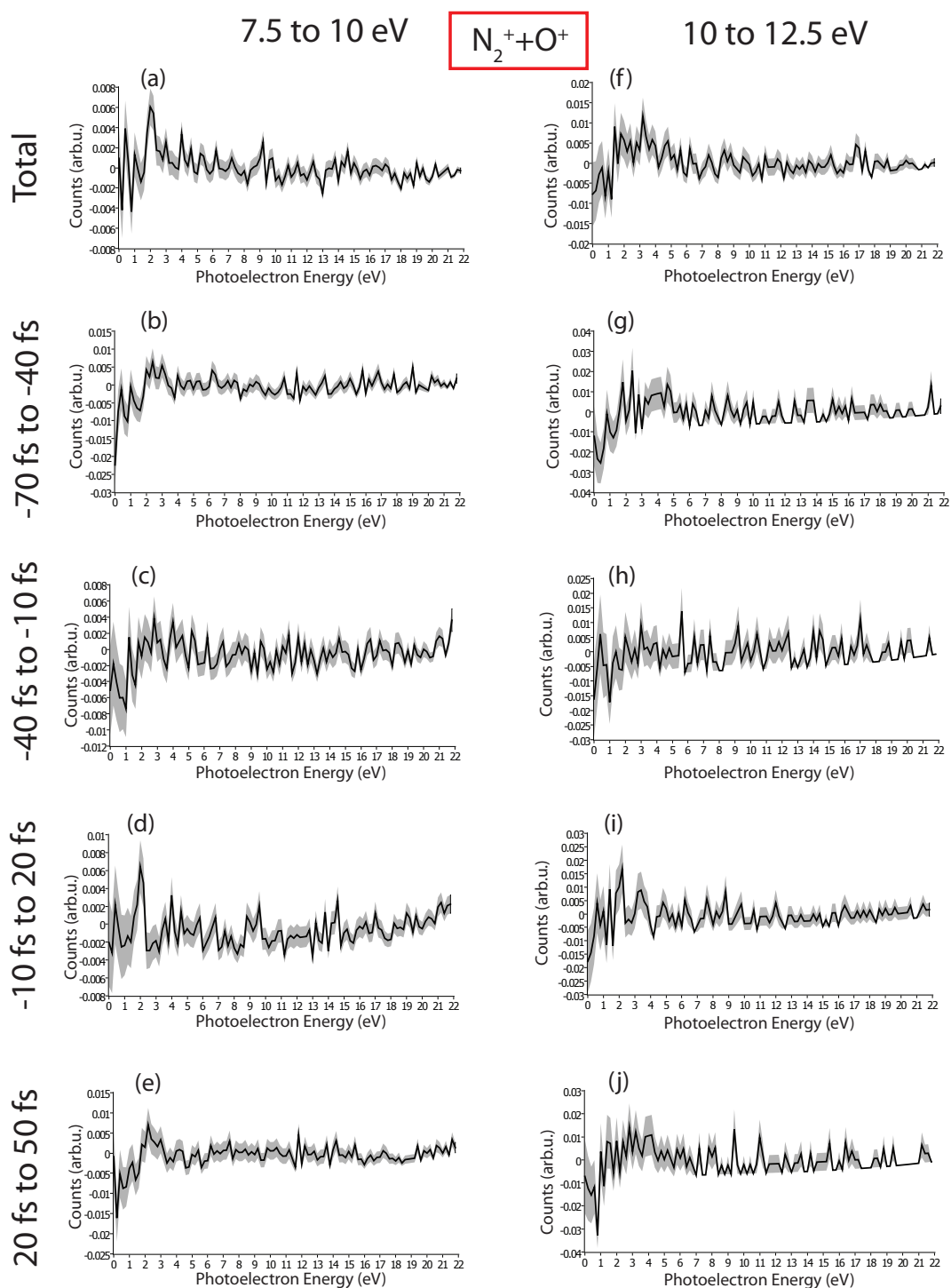


Figure 13.23: The photoelectron energy background subtracted as described in the text for different delays and different KERs of the $N_2^+ + O^+ + e^-$ coincidence. The gray area depicts the statistical error or the distribution.

VI Conclusion

Summary

The achievements of this thesis can be divided into two parts considering the construction of the XUV spectrometer on the one hand and the results of the XUV-pump IR-probe measurement on nitrous oxide on the other hand.

The spectrometer was designed and built-up within the scope of this work. This device enables the online recording of the the harmonic spectrum without interrupting ongoing measurements in the ReMi. This is achieved by using the transmitted light from the ReMi and by separating the vacuum systems of the experiment and the spectrometer by an appropriate differential pumping state. It was shown, that the detected spectra could be successfully calibrated by means of the geometry of the spectrometer, the regular structure in the photon energy of the harmonic radiation, and additional information gained from photoelectron-energy spectra received from the ReMi. Even though the actual application of the apparatus, namely the observation and control of the stability of the HHG during experiments, was not yet implemented, the obtained data contributed significantly to the interpretation of the presented experiment, since it was possible to identify dominantly contributing states of nitrous oxide to certain reaction channels.

The main results of this thesis are derived from the presented XUV-pump IR-probe measurement using nitrous oxide as target gas. The delay between both pulses was varied from -75 fs to 55 fs, where negative values denote that the XUV pulse train precedes the IR pulse. The applied pulses had durations of approximately 25 ± 2 fs for the IR pulse and 16.3 ± 1.3 fs for the XUV pulse train. Both values are determined experimentally from the time-dependent photoelectron energy spectrum measured in coincidence with N_2O^+ ions. Here, the production of sidebands was observed, which correspond to a cross-correlation of the involved pulses and, thus, reveal their duration. In addition, the spectral information gained from the harmonic spectrum measured in the spectrometer at the end of the pump-probe measurement indicated that for the production of stable N_2O^+

the molecule is dominantly excited into the singly ionized X^2II state.

Additionally, it was shown, that excited cations may dissociate into a charged and a neutral fragment. The yield of the four different ionic fragments was compared, showing that 75.7 % of the produced ions are NO^+ , N_2^+ appears in 10.7 % of the events, N^+ in 10.0 % and O^+ in 3.6 %. These results are in agreement with previous observations [125, 127, 128]. Furthermore, it was presented that the kinetic energy release (KER) of the NO^+ ions is composed by two distributions, which were distinguished by the respective photoelectron energies. The origin of the contribution centered around 195 meV was assigned mainly to the second excited state B^2II , but also to the ground, and the third excited state X^2II and $C^2\Sigma^+$, while it was shown that for ions with KERs above 400 meV the molecule was excited into the $C^2\Sigma^+$ state. The KER of the N^+ ions featured a triple-peak structure (peaks at 95 meV, 250 meV, and 385 meV) induced by the excitation of different vibrational modes of the $C^2\Sigma^+$ state. The determined energy spacings between the vibrational levels agree with previous experiments [124, 127–129].

Finally, regarding the time-dependent ionization yield, it was shown that there is a difference between the two channels resulting in an atomic ion and the channels resulting in molecular ions. In the first case, the ionization yield decreases during the temporal overlap of XUV and IR pulses, whereas in the latter case the yield slightly rises for increasing positive delay times. However, the time-dependent behavior vanishes when taking additionally into account the ions originating from the double-ionization process, which indicates that the delay dependence is due to a correlation between single- and double-ionization channels provoked by the additional IR-field interaction.

The available energies in the harmonic spectrum are sufficient to doubly ionize the nitrous oxide molecule. Mainly two competitive processes are thereby contributing, namely direct double ionization by photons with energies above 35.8 eV and autoionization of a singly ionized and highly excited cation N_2O^{+*} , in which one electron is ionized from an inner shell and the ion relaxes in an Auger-like process under emission of a second electron [120]. In both cases, the resulting N_2O^{2+} decays within a few hundred fs into two charged fragments, at which either the bond between the two nitrogen atoms or the bond between the central nitrogen and the oxygen can dissociate.

Comparing the ionization yield of both dissociation channels as function of the delay between pump and probe pulse reveals that both yields are increased around the temporal overlap of both pulses even though the dissociation of the $N - O$ bond shows a stronger effect. Taking all events into account, the enhancement of this channel amounts to a

factor of 2.2, whereas the $N - N$ bond-breaking channel is enhanced by a factor of 2. By choosing only events resulting in KERs above 4 eV, the augmentation of the ionization yield of the $N - O$ bond-breaking channel can be raised to a factor of approximately 3, while the second dissociation channel is mainly unaffected. This KER-dependent effect can be understood by inspecting the respective KERs.

The measured KER of both dissociation channels mainly agree with the KERs expected from several accessible doubly ionized states. In the case where the N_2O^{2+} dissociates into N_2^+ and O^+ , additional low KERs are detected, which can be assigned to the autoionization process, for which a KER of 2.3 eV is expected [24]. In the second channel this is not observed, since the KERs expected for the autoionization (~ 4.7 eV) are overlapping at the rising edge of the main KER distribution.

Additionally, it was shown that the KER is shifted towards higher energies when pump and probe pulse are overlapping, which is simultaneously attended by a reduction of the yield of ions at the KERs, which are correlated to the autoionization process (especially for the dissociation of the $N - O$ bond). This decrease is an indication for an IR-induced interruption of the autoionization by ionizing a second electron from a highly excited N_2O^{+*} . Apparently, in comparison to the autoionization the photon-induced premature ionization of the second leads to higher KERs.

Finally, the ReMi also allows to detect the photoelectrons emerging from the double-ionization process. Their energy distribution is dominated by low-energy electrons since our harmonic spectrum only barely exceeds the double-ionization threshold and due to the fact that the states of the doubly charged ion are energetically very close. These spectra revealed additional peaks at 1.1 eV for the $N - N$, and at 2 eV for the $N - O$ bond-breaking channel, respectively. It was shown that in both channels the peaks are strongest at KERs of ions that can be related to the autoionization, which indicates that these peaks are caused by the autoionized electrons. However, in the $N - O$ bond-breaking channel the signal can be observed over a wider range of KERs as in the $N - N$ bond-breaking channel. Furthermore, the peaks in the latter reaction exhibit only a minor dependence on the delay between the laser pulses, whereas for $N - O$ bond-breaking an increase of the yield at the overlap and at positive delay times is found.

The information gained from the electron energy spectra again supports the findings mentioned above: The additional IR field has a notably higher influence on the dissociation of the N_2O^{2+} into N_2^+ and O^+ , than on the dissociation of the $N - N$ bond and the IR pulses interrupt the autoionization process, which is observed by a lower yield of the

respective electrons at negative delay times, at which the XUV ionizes the nitrous oxide first.

Outlook

The main future prospects for the spectrometer are the development of a very stable, accurately and repeatably adjustable support for the detection and imaging unit and the implementation of an automated data acquisition. Currently, the image data from the camera are taken via a commercially available program, whereas the calibration and analysis of the data was implemented in LabVIEW²⁴. Therefore, it would be helpful to develop a program, which combines both and which is additionally able to acquire harmonic spectra autonomously either continuously or in periodic time intervals. Therewith, the HHG spectrum could be traced even during long-running measurements, such that it would be possible to select subsequently time periods with stable harmonic spectrum.

The stability is a crucial parameter especially when single attosecond pulses (SAP) are used in the experiment but also in case, the energy of a certain harmonic is close to the potential energy of a certain state such that the respective harmonic could be able to excite this state resonantly or not depending on the exact energy of the respective harmonic. In this case a slight shift of the spectrum may change the experimental results.

Concerning the presented pump-probe measurement on nitrous oxide, a further understanding of the experimental data would require a profound theoretical model, which is missing up to now. Nevertheless, it could be interesting to investigate the dynamics observed in the scope of this work using shorter pump and probe pulses, since the pulse durations during the measurement were relatively long for the introduced setup with 25 fs for the fundamental IR pulses and approximately 16 fs for the attosecond pulse train. Therefore, it would be possible to reduce the duration of the IR pulses to approximately 10 fs without any additional significant effort. Furthermore, the application of even shorter pulses approaching the SAP regime may be of interest, since faster dynamics in the molecular system may be revealed.

Additionally, in reference [23] the observation of carrier-envelope phase (CEP) dependent effects in N_2O was presented. Therefore, it would be interesting to combine the CEP-

²⁴ short for Laboratory Virtual Instrument Engineering Workbench from National Instruments Germany GmbH, Ganghofer Straße 70 b, 80339 München

dependent measurement with the pump-probe technique. However, concerning the required statistics, it would probably be necessary to make a continuous scan of either the CEP or the delay at a fixed value of the other parameter and repeating measurement for several discrete values of the fixed parameter.

One difficulty in the analysis of the double ionization of nitrous oxide was the fact that it was not possible to measure two electrons in coincidence for a single event. This problem arises due to the short TOF differences between the impact of two electrons, which are then not distinguishable as two different events for the read-out electronics. However, first attempts were made to ameliorate the situation. The ability to separate both electrons would enable a more detailed insight into the electronic processes, especially considering the autoionization of N_2O^{+*} , for which it should be possible to identify the two consecutively ionized electrons by their TOF. Then it would be possible to gain more information about the delay-dependent influence of the additional IR-field on the autoionization.

Further, the splitting of the fundamental IR beam into the part, which is used to produce the XUV pulses, and the part, which is used as probe pulse, holds a disadvantage, since in this case less energy per pulse is available for the HHG. Increasing the pulse energy would enable the usage of different target gases with higher ionization potentials (such as neon or helium) and, thus, the production of higher photon energies. These could be high enough to create higher charged ions. This would enable the study of different dissociation channels of multiple charged ions, such as N_2O^{3+} , which may dissociate into three singly charged, or a doubly and singly charged fragment. In the latter case, it could be interesting for example to study the charge distribution between the atomic and the molecular fragments for the different channels, as well as the influence of the IR-probe pulse on the triple ionization.

In the beginning of chapter V, which presents the experimental results, it was shown that also the dissociation of the dimer $(N_2O)_2$ into two singly charged N_2O^+ was observed in the experiment. The respective data are not presented in this work due to the poor statistic of this reaction channel. Nevertheless, it would be interesting studying the dissociation and a related time-dependence, concerning effects such as intermolecular Coulombic decay (ICD). But it would be necessary on the one hand to increase the statistics by extending the observation time and by augmenting the number of dimers in the target jet, e.g. by increasing the pre-pressure of the gas jet. On the other hand, it would be required to prolong the delay range to several 100 fs, since ICD lifetimes span from a few tens of fs to the ps regime [82]. Additionally, the wider delay range may reveal other effects occurring

on slower time scales, such as photon-induced rotational modes or the bending of the molecule.

Bibliography

- [1] Andreas Velten, Di Wu, Adrian Jarabo, Belen Masia, Christopher Barsi, Chinmaya Joshi, Everett Lawson, Mounqi Bawendi, Diego Gutierrez, and Ramesh Raskar. Femto-photography: Capturing and visualizing the propagation of light. *ACM Transactions on Graphics (TOG)*, 32(4):44, 2013.
- [2] K Nakagawa, A Iwasaki, Y Oishi, R Horisaki, A Tsukamoto, A Nakamura, K Hirosawa, H Liao, T Ushida, K Goda, et al. Sequentially timed all-optical mapping photography (STAMP). *Nature Photonics*, 2014.
- [3] J. Ullrich, R. Moshhammer, A. Dorn, R. Dörner, L. Schmidt, and H. Schmidt-Böcking. Recoil-ion and electron momentum spectroscopy: reaction microscopes. *Report*, 66: 1463, 2003.
- [4] PF Moulton. Spectroscopic and laser characteristics of Ti: Al₂O₃. *Journal of the Optical Society of America B*, 3(1):125–133, 1986.
- [5] TH Maiman. Stimulated optical radiation in ruby. *Nature*, 1960.
- [6] P.A. Franken, AE Hill, CW Peters, and G. Weinreich. Generation of optical harmonics. *Phys. Rev. Lett.*, 7(4):118–119, 1961.
- [7] A. McPherson, G. Gibson, H. Jara, U. Johann, TS Luk, IA McIntyre, K. Boyer, and CK Rhodes. Studies of multiphoton production of vacuum-ultraviolet radiation in the rare gases. *Journal of the Optical Society of America B*, 4(4):595–601, 1987.
- [8] M. Ferray, A. L Huillier, XF Li, LA Lompre, G. Mainfray, and C. Manus. Multiple-harmonic conversion of 1064 nm radiation in rare gases. *Journal of Physics B: Atomic, Molecular and Optical Physics*, 21:L31, 1988.
- [9] SE Harris, JJ Macklin, and TW Hänsch. Atomic scale temporal structure inherent to high-order harmonic generation. *Optics communications*, 100(5):487–490, 1993.

- [10] Eleftherios Goulielmakis, M Schultze, M Hofstetter, Vladislav S Yakovlev, Justin Gagnon, M Uiberacker, Andrew L Aquila, EM Gullikson, David T Attwood, Reinhard Kienberger, et al. Single-cycle nonlinear optics. *Science*, 320(5883):1614–1617, 2008.
- [11] Tenio Popmintchev, Ming-Chang Chen, Dimitar Popmintchev, Paul Arpin, Susannah Brown, Skirmantas Ališauskas, Giedrius Andriukaitis, Tadas Balčiunas, Oliver D Mücke, Audrius Pugzlys, et al. Bright coherent ultrahigh harmonics in the keV x-ray regime from mid-infrared femtosecond lasers. *science*, 336(6086):1287–1291, 2012.
- [12] H. Rietz. *Attosekundenphysik mit dem Reaktionsmikroskop: Eine Konzeptstudie, erste Experimente und mögliche Anwendungen*. PhD thesis, Ruperto-Carola-University of Heidelberg, 2012.
- [13] Alexander Sperl. *XUV-IR pump-probe experiments: Exploring nuclear and electronic correlated quantum dynamics in the hydrogen molecule*. PhD thesis, Ruperto-Carola-University of Heidelberg, 2013.
- [14] Andreas Fischer, Alexander Sperl, Philipp Cörlin, Michael Schönwald, Helga Rietz, Alicia Palacios, Alberto González-Castrillo, Fernando Martín, Thomas Pfeifer, Joachim Ullrich, et al. Electron localization involving doubly excited states in broadband extreme ultraviolet ionization of H 2. *Physical review letters*, 110(21):213002, 2013.
- [15] Andreas Fischer, Alexander Sperl, Philipp Cörlin, Michael Schönwald, Sebastian Meuren, Joachim Ullrich, Thomas Pfeifer, Robert Moshhammer, and Arne Senftleben. Measurement of the autoionization lifetime of the energetically lowest doubly excited $Q_1\Sigma_u^+$ state in H2 using electron ejection asymmetry. *Journal of Physics B: Atomic, Molecular and Optical Physics*, 47(2):021001, 2014.
- [16] Andreas Fischer, Martin Gärttner, Philipp Cörlin, Alexander Sperl, Michael Schönwald, Tomoya Mizuno, Giuseppe Sansone, Arne Senftleben, Joachim Ullrich, Bernold Feuerstein, et al. Molecular wave-packet dynamics on laser-controlled transition states. *arXiv preprint arXiv:1410.8032*, 2014.
- [17] Thomas E Keys. The development of anesthesia. *Anesthesiology*, 2(5):552–574, 1941.
- [18] Vadim Zakirov, Martin Sweeting, Timothy Lawrence, and Jerry Sellers. Nitrous oxide as a rocket propellant. *Acta Astronautica*, 48(5):353–362, 2001.

-
- [19] Eric A Davidson and David Kanter. Inventories and scenarios of nitrous oxide emissions. *Environmental Research Letters*, 9(10):105012, 2014.
- [20] Paul J Crutzen and Uta Schmailzl. Chemical budgets of the stratosphere. *Planetary and Space Science*, 31(9):1009–1032, 1983.
- [21] Lin Mei, Liu Ya-Wei, Zhong Zhi-Ping, and Zhu Lin-Fan. Decay pathways of superexcited states of nitrous oxide. *Chinese Physics B*, 23(5):053403, 2014.
- [22] Johan Albrecht Schmidt, Matthew Stanley Johnson, U Lorenz, GC McBane, and R Schinke. Photodissociation of N₂O: Energy partitioning. *The Journal of chemical physics*, 135(2):024311, 2011.
- [23] M Kübel, AS Alnaser, B Bergues, T Pischke, J Schmidt, Y Deng, C Jendrzewski, J Ullrich, GG Paulus, AM Azzeer, et al. Strong-field control of the dissociative ionization of N₂O with near-single-cycle pulses. *New Journal of Physics*, 16(6):065017, 2014.
- [24] Stefano Falcinelli, Marzio Rosi, Pietro Candori, Franco Vecchiocattivi, James M Farrar, Fernando Pirani, Nadia Balucani, Michele Alagia, Robert Richter, and Stefano Stranges. Kinetic energy release in molecular dications fragmentation after VUV and EUV ionization and escape from planetary atmospheres. *Planetary and Space Science*, 2014.
- [25] FJ McClung and RW Hellwarth. Giant optical pulsations from ruby. *Journal of Applied Physics*, 33(3):828–829, 1962.
- [26] D.A. Stetser H. Heynau A.J. DeMaria. MODE LOCKING OF A ND₃⁺-DOPED GLASS LASER. *Appl. Phys. Lett.*, 9:174, 1966.
- [27] T. Brabec and F. Krausz. Intense few-cycle laser fields: Frontiers of nonlinear optics. *Reviews of Modern Physics*, 72(2):545–591, 2000.
- [28] Markus Werner Sigrist Fritz Kurz Kneubuehl. *Laser*. B. G. Teubner Verlag, 2005.
- [29] Georg Gademann. Komprimierung ultrakurzer Lichtimpulse mit Hilfe der Filamentation und eines adaptiven Impulskompressors. Master’s thesis, Max-Planck Institut fuer Kernphysik Heidelberg, Universitaet Heidelberg, 2007.

- [30] Alexander Sperl. Erzeugung und Charakterisierung ultrakurzer Lichtimpulse fuer die Generation Hoher Harmonischer Strahlung. Master's thesis, Max-Planck Institut fuer Kernphysik Heidelberg, Universitaet Heidelberg, 2009.
- [31] A.E. Siegman. *Lasers*. Mill Valley, 1986.
- [32] D. Meschede. *Optik, Licht und Laser*. Vieweg+ Teubner Verlag, 2008.
- [33] Ursula Keller. Recent developments in compact ultrafast lasers. *Nature*, 424(6950): 831–838, 2003.
- [34] Jonghan Jin and Seung-Woo Kim. Precision Dimensional Metrology based on a Femtosecond Pulse Laser. 2010.
- [35] DE Spence, PN Kean, and W. Sibbett. 60-fsec pulse generation from a self-mode-locked Ti: sapphire laser. *Optics Letters*, 16(1):42–44, 1991.
- [36] J.C. Diels, W. Rudolph, P. Gibbon, F.X. Kaertner, T. Iwazumi, K. Mase, S.H. Gold, G.S. Nusinovich, P.M. Smith, B.E. Carlsten, et al. *Ultrashort Laser Pulse Phenomena: Fundamentals, Techniques, and Applications on a Femtosecond Time Scale*. Inst. Phys., 1996.
- [37] RL Fork, OE Martinez, and JP Gordon. Negative dispersion using pairs of prisms. *Optics letters*, 9(5):150–152, 1984.
- [38] J.P. Gordon and RL Fork. Optical resonator with negative dispersion. *Optics letters*, 9(5):153–155, 1984.
- [39] Donna Strickland and Gerard Mourou. Compression of amplified chirped optical pulses. *Optics communications*, 55(6):447–449, 1985.
- [40] Vladislav Yakovlev and Gabriel Tempea. Optimization of chirped mirrors. *Applied optics*, 41(30):6514–6520, 2002.
- [41] RR Alfano. *The supercontinuum laser source*, 1989.
- [42] Maria Göppert-Mayer. Über elementarakte mit zwei quantensprüngen. *Annalen der Physik*, 401(3):273–294, 1931.

- [43] LV Keldysh. Ionization in the field of a strong electromagnetic wave. *Sov. Phys. JETP*, 20(5):1307–1314, 1965.
- [44] N.B. Delone and V.P. Krainov. *Multiphoton Processes in Atoms*. Springer series on atoms and plasmas. Springer, 2nd edition edition, 1999.
- [45] P. et al. Agostini. Free-Free Transitions Following Six-Photon Ionization of Xenon Atoms. *Phys. Rev. Lett.*, 42.17:1127–1130, 1979.
- [46] Thomas Brabec. *Strong field laser physics*. Springer, 2008.
- [47] P Kruit, J Kimman, Harm G Muller, and MJ Van der Wiel. Electron spectra from multiphoton ionization of xenon at 1064, 532, and 355 nm. *Physical Review A*, 28(1):248, 1983.
- [48] MV Ammosov, NB Delone, VP Krainov, et al. Tunnel ionization of complex atoms and of atomic ions in an alternating electromagnetic field. *Sov. Phys. JETP*, 64(6): 1191–1194, 1986.
- [49] S. Augst, DD Meyerhofer, D. Strickland, and SL Chint. Laser ionization of noble gases by Coulomb-barrier suppression. *Journal of the Optical Society of America B*, 8(4):858–867, 1991.
- [50] G. Farkas and C. Toth. Proposal for attosecond light pulse generation using laser induced multiple-harmonic conversion processes in rare gases. *Phys. Lett. A*, 168(5-6):447–450, 1992.
- [51] Thomas Pfeifer. *Adaptive Control of Coherent Soft X-Rays*. PhD thesis, Julius-Maximilians-Universitaet Wuerzburg, 2004.
- [52] JJ Macklin, JD Kmetec, and CL Gordon III. High-order harmonic generation using intense femtosecond pulses. *Phys. Rev. Lett.*, 70(6):766–769, 1993.
- [53] A. L Huillier and P. Balcou. High-order harmonic generation in rare gases with a 1-ps 1053-nm laser. *Phys. Rev. Lett.*, 70(6):774–777, 1993.
- [54] J.L. Krause, K.J. Schafer, and K.C. Kulander. High-order harmonic generation from atoms and ions in the high intensity regime. *Phys. Rev. Lett.*, 68(24):3535–3538, 1992.

- [55] PB Corkum. Plasma perspective on strong field multiphoton ionization. *Phys. Rev. Lett.*, 71(13):1994–1997, 1993.
- [56] KC Kulander, KJ Schafer, and JL Krause. Super-intense laser-atom physics. *NATO Advanced Science Institutes Series*, 316:?, 1993.
- [57] M. Lewenstein, P. Balcou, M.Y. Ivanov, A. L Huillier, and PB Corkum. Theory of high-harmonic generation by low-frequency laser fields. *Phys. Rev. A*, 49(3):2117–2132, 1994.
- [58] Michael Yu Kuchiev. Atomic antenna. *JETP Lett*, 45(7):404–406, 1987.
- [59] G. P. ZHANG. HIGH HARMONIC GENERATION IN ATOMS, MOLECULES AND NANOSTRUCTURES. *International Journal of Modern Physics B: Condensed Matter Physics; Statistical Physics; Applied Physics*, 21(31):5167–5185, 2007. ISSN 02179792. URL <http://search.ebscohost.com/login.aspx?direct=true&db=aph&AN=28021583&site=ehost-live>.
- [60] Zenghu Chang. *Fundamentals of Attosecond Optics*. CRC Press, 2011.
- [61] MB Gaarde, F. Salin, E. Constant, P. Balcou, KJ Schafer, KC Kulander, and A. L Huillier. Spatiotemporal separation of high harmonic radiation into two quantum path components. *Phys. Rev. A*, 59(2):1367–1373, 1999.
- [62] T. Auguste and P. Salières. Theoretical and experimental analysis of quantum path interferences in high-order harmonic generation. *Phys. Rev. A*, 80:033817, 2009.
- [63] P. Balcou, A.S. Dederichs, M.B. Gaarde, and A. L Huillier. Quantum-path analysis and phase matching of high-order harmonic generation and high-order frequency mixing processes in strong laser fields. *Journal of Physics B: Atomic, Molecular and Optical Physics*, 32:2973, 1999.
- [64] A. Jullien, T. Pfeifer, MJ Abel, PM Nagel, MJ Bell, DM Neumark, and SR Leone. Ionization phase-match gating for wavelength-tunable isolated attosecond pulse generation. *Appl. Phys. B: Lasers and Optics*, 93(2):433–442, 2008.
- [65] Michael Schönwald. Phase-matched few-cycle high-harmonic generation: ionisation gating and half-cycle cutoffs. Master’s thesis, Ruperto-Carola University of Heidelberg, September 2010.

- [66] K.J. Schafer and K.C. Kulander. High harmonic generation from ultrafast pump lasers. *Phys. Rev. Lett.*, 78(4):638–641, 1997.
- [67] T. Pfeifer, C. Spielmann, and G. Gerber. Femtosecond x-ray science. *Reports on Progress in Physics*, 69:443, 2006.
- [68] P. Agostini and L.F. DiMauro. The physics of attosecond light pulses. *Reports on Progress in Physics*, 67:813, 2004.
- [69] P. Salieres, B. Carre, L. Le Deroff, F. Grasbon, GG Paulus, H. Walther, R. Kopold, W. Becker, DB Milosevic, A. Sanpera, et al. Feynman’s path-integral approach for intense-laser-atom interactions. *Science*, 292(5518):902, 2001.
- [70] T Kanai, E. J Takahashi, Y. Nabekawa, and K. Midorikawa. Destructive interference during high harmonic generation in mixed gases. *Phys. Rev. Lett.*, 98:153904, 2007.
- [71] E. Constant, D. Garzella, P. Breger, E. Mevel, C. Dorrer, C. Le Blanc, F. Salin, and P. Agostini. Optimizing high harmonic generation in absorbing gases: model and experiment. *Phys. Rev. Lett.*, 82(8):1668–1671, 1999.
- [72] Johan Mauritsson, Per Johnsson, E Gustafsson, Anne L’Huillier, KJ Schafer, and MB Gaarde. Attosecond pulse trains generated using two color laser fields. *Physical review letters*, 97(1):013001, 2006.
- [73] M Nisoli and G Sansone. New frontiers in attosecond science. *Progress in Quantum Electronics*, 33(1):17–59, 2009.
- [74] T. Glover, R. Schoenlein, A. Chin, and C. Shank. Observation of laser assisted photoelectric effect and femtosecond high order harmonic radiation. *Phys. Rev. Lett.*, 76(14):2468–2471, 1996.
- [75] H. Reiss. Effect of an intense electromagnetic field on a weakly bound system. *Phys. Rev. A*, 22(5):1786, 1980.
- [76] J. Mauritsson, P. Johnsson, R. Lopez-Martens, K. Varju, W. Kornelis, J. Biegert, U. Keller, M. Gaarde, K. Schafer, and A. L’Huillier. Measurement and control of the frequency chirp rate of high-order harmonic pulses. *Phys. Rev. A.*, 70(2):02801, 2004.

- [77] Richard P Feynman, Robert B Leighton, and Matthew Sands. *The feynman lectures on physics. 3: Quantum mechanics: Lectures on physics*. Addison-Wesley, 1965.
- [78] Mitchel Weissbluth. *Atoms and molecules*. Elsevier, 1978.
- [79] Franco Iachello and RD Levine. Algebraic theory of molecules. *New York: Oxford*, 1995.
- [80] Hermann Haken and Hans Christoph Wolf. *Molecular physics and elements of quantum chemistry: introduction to experiments and theory*. Springer, 2004.
- [81] Wolfgang Demtröder. Experimentalphysik, volume 3: Atome, Moleküle und Festkörper.
- [82] Kirsten Schnorr. *XUV Pump-Probe Experiments on Electron Rearrangement and Interatomic Coulombic Decay in Diatomic Molecules*. PhD thesis, Ruperto-Carola-University of Heidelberg, 2014.
- [83] Brian Harold Bransden and Charles Jean Joachain. *Physics of atoms and molecules*. Pearson Education India, 2003.
- [84] Ahmed Zewail. The nobel prize in chemistry 1999, 1999.
- [85] Frank Grossmann. *Theoretical Femtosecond Physics: Atoms and Molecules in Strong Laser Fields*, volume 48. Springer, 2008.
- [86] M Schultze, A Wirth, I Grguras, M Uiberacker, T Uphues, AJ Verhoef, J Gagnon, M Hofstetter, U Kleineberg, E Goulielmakis, et al. State-of-the-art attosecond metrology. *Journal of Electron Spectroscopy and Related Phenomena*, 184(3):68–77, 2011.
- [87] Eleftherios Goulielmakis, Adrian Wirth, Ivanka Grguras, Mohammed Hassan, Justin Gagnon, Antoine Moulet, Tran Trung Luu, Vladimir Pervak, and Ferenc Krausz. Sub-optical-cycle waveform synthesis of light. In *Lasers and Electro-Optics Europe (CLEO EUROPE/EQEC), 2011 Conference on and 12th European Quantum Electronics Conference*, pages 1–1. IEEE, 2011.
- [88] A Moulet, V Tosa, and E Goulielmakis. Coherent kiloelectronvolt x-rays generated by subcycle optical drivers: a feasibility study. *Optics letters*, 39(21):6189–6192, 2014.

- [89] F Calegari, D Ayuso, A Trabattoni, L Belshaw, S De Camillis, S Anumula, F Frassetto, L Poletto, A Palacios, P Decleva, et al. Ultrafast electron dynamics in phenylalanine initiated by attosecond pulses. *Science*, 346(6207):336–339, 2014.
- [90] Donna Strickland and Gerard Mourou. Compression of amplified chirped optical pulses. *Optics Communications*, 55.6:447–449, 1985.
- [91] Philipp Cörlin. Laser induced Coulomb-explosion of allene molecules: Experiment and simulation. Master’s thesis, Ruperto-Carola-University of Heidelberg, 2012.
- [92] R. Gopal. *Electron Wave Packet Interferences in Ionization with Few-Cycle Laser Pulses and the Dissociative Photoionization of D2 with Ultrashort Extreme Ultraviolet Pulses*. PhD thesis, Ruperto-Carola-University of Heidelberg, 2009.
- [93] M. et al. Nisoli. High-Brightness High-Order Harmonic Generation by Truncated Bessel Beams in the Sub-10-fs-Regime. *Phys. Rev. Lett.*, 88.3:033902, 2002.
- [94] Private communication with Philipp Cörlin.
- [95] Helga Rietz. Aufbau und Inbetriebnahme einer Apparatur zur Erzeugung hoher harmonischer Strahlung und deren Charakterisierung. Master’s thesis, Max-Planck Institut fuer Kernphysik Heidelberg, Universitaet Heidelberg, 2007.
- [96] Rodrigo et al. Lopez-Martens. Amplitude and Phase Control of Attosecond Light Pulses. *Phys. Rev. Lett.*, 94.3:033001, 2005.
- [97] Lawrence Berkeley Laboratory. Atomic Scattering Factors. URL http://henke.lbl.gov/optical_constants/.
- [98] P. Kirkpatrick and A.V. Baez. Formation of Optical Images by X-Rays. *Journal of the Optical Society of America*, 38:766–773, 1948.
- [99] G Tondello. The use of a toroidal mirror as a focusing element for a stigmatic grazing incidence spectrometer. *Journal of Modern Optics*, 26(3):357–371, 1979.
- [100] X-Ray Database, www.cxro.lbl.gov/.
- [101] J Higuët, H Ruf, Nicolas Thiré, Raluca Cireasa, E Constant, E Cormier, D Descamps, E Mével, S Petit, B Pons, et al. High-order harmonic spectroscopy of the Cooper

- minimum in argon: Experimental and theoretical study. *Physical Review A*, 83(5): 053401, 2011.
- [102] R. Moshhammer, M. Unverzagt, W. Schmitt, J. Ullrich, and H. Schmidt-Böcking. A 4π recoil-ion electron momentum analyser: a high resolution "microscope" for the investigation of the dynamics of atomic, molecular and nuclear reactions. *Nuclear Instruments and Methods in Physics Research Section B: Beam Interactions with Materials and Atoms*, 108(4):425–445, 1996.
- [103] Wolfgang Demtröder. *Experimentalphysik 1*. Springer, 2005.
- [104] D. Fischer. *Mehr-Teilche-Dynamik in der Einfach- und Doppelionisation von Helium durch geladene Projektile*. PhD thesis, Ruperto-Carola-University of Heidelberg, 2003.
- [105] Martin Laux. Construction and characterization of a new Reaction Microscope. Master's thesis, July 2011.
- [106] *RoentDek Handels GmbH, Im Vogelshaag 8, D-65779 Kelkheim, Germany, www.roentdek.com*.
- [107] Winfried Löther. Entwicklung einer Messwerterfassung für einen orts- und zeitauflösenden Detektor. Master's thesis, Friedrich-Schiller-Universität Jena, 2009.
- [108] Thomas Pflüger. *Electron Impact Ionization Studies of Small Rare Gas Clusters*. PhD thesis, Ruperto-Carola University of Heidelberg.
- [109] M. Wutz, H. Adam, W. Walcher, and K. Jousten. *Handbuch Vakuumtechnik*. Vieweg Wiesbaden, 2000.
- [110] JL Olivier, Robert Locht, and J Momigny. The dissociative ionization of nitrous oxide. An electroionization study. *International Journal of Mass Spectrometry and Ion Processes*, 58:293–305, 1984.
- [111] Christian R. Ott. *Attosecond multidimensional interferometry of single and two correlated electrons in atoms*. PhD thesis, Ruperto-Carola-University of Heidelberg, 2012.

- [112] Christian Ott, Andreas Kaldun, Philipp Raith, Kristina Meyer, Martin Laux, Jörg Evers, Christoph H Keitel, Chris H Greene, and Thomas Pfeifer. Lorentz meets Fano in spectral line shapes: A universal phase and its laser control. *Science*, 340(6133):716–720, 2013.
- [113] William C Trogler. Physical properties and mechanisms of formation of nitrous oxide. *Coordination chemistry reviews*, 187(1):303–327, 1999.
- [114] JL Olivier, Robert Locht, and J Momigny. A dissociative electroionization study of nitrous oxide. The $\text{NO}^+ + e^-$ and $\text{N}_2^+ + e^-$ dissociation channels. *Chemical Physics*, 68(1):201–211, 1982.
- [115] JL Olivier, Robert Locht, and J Momigny. A dissociative electroionization study of nitrous oxide. The $\text{O}^+ + e^-$ and $\text{N}^+ + e^-$ dissociation channels. *Chemical physics*, 84(2):295–309, 1984.
- [116] Pragya Bhatt, Raj Singh, Namita Yadav, and R Shanker. Momentum spectroscopy of fragment ions of a multiply charged N_2O molecule under impact of 10-keV electrons. *Physical Review A*, 86(5):052708, 2012.
- [117] E Sokell, AA Wills, J Comer, and P Hammond. A two-dimensional study of the autoionizing decay routes of Rydberg states converging on the ionization threshold in. *Journal of Physics B: Atomic, Molecular and Optical Physics*, 30(11):2635, 1997.
- [118] Bong Hyun Boo, Myun Kwon, Suk Jae Yoo, and Inosuke Koyano. Dissociative photoionization of nitrous oxide in the range of 22–133 eV, photofragmentation pattern and efficiency relevant to the electronic state. *Journal of the Korean Physical Society*, 51(1):43–47, 2007.
- [119] Michele Alagia, Pietro Candori, Stefano Falcinelli, Michel Lavollée, Fernando Pirani, Robert Richter, Stefano Stranges, and Franco Vecchiocattivi. Double photoionization of N_2O molecules in the 28–40eV energy range. *Chemical physics letters*, 432(4):398–402, 2006.
- [120] X Zhou, P Ranitovic, CW Hogle, JHD Eland, HC Kapteyn, and MM Murnane. Probing and controlling non-Born-Oppenheimer dynamics in highly excited molecular ions. *Nature Physics*, 8(3):232–237, 2012.

- [121] PM Dehmer, JL Dehmer, and WA Chupka. Effects of vibronic interaction and autoionization on the photoelectron spectrum of N₂O. *The Journal of Chemical Physics*, 73(1):126–133, 1980.
- [122] CR Brundle and DW Turner. Studies on the photoionisation of the linear triatomic molecules: N₂O, COS, CS₂ and CO₂ using high-resolution photoelectron spectroscopy. *International Journal of Mass Spectrometry and Ion Physics*, 2(3):195–220, 1969.
- [123] S Taylor, JH Eland, and M Hochlaf. Fluorescence and metastability of N₂O₂⁺: theory and experiment. *The Journal of chemical physics*, 124(20):204319–204319, 2006.
- [124] Irene Nenner, Paul-Marie Guyon, Tomas Baer, and Thomas R Govers. A threshold photoelectron–photoion coincidence study of the N₂O⁺ dissociation between 15 and 20.5 eV. *The Journal of Chemical Physics*, 72(12):6587–6592, 1980.
- [125] E Kinmond, JHD Eland, and L Karlsson. Dissociation of N₂⁺ O⁺ ions from the valence states reached by one-photon photoionisation. *International journal of mass spectrometry*, 185:437–447, 1999.
- [126] R López-Martens, Johan Mauritsson, Per Johnsson, Katalin Varjú, Anne L’Huillier, W Kornelis, J Biegert, U Keller, M Gaarde, and K Schafer. Characterization of high-order harmonic radiation on femtosecond and attosecond time scales. *Applied Physics B*, 78(7-8):835–840, 2004.
- [127] Xiaofeng Tang, Mingli Niu, Xiaoguo Zhou, Shilin Liu, Fuyi Liu, Xiaobin Shan, and Liusi Sheng. NO⁺ formation pathways in dissociation of N₂O⁺ ions at the C₂Σ⁺ state revealed from threshold photoelectron–photoion coincidence velocity imaging. *The Journal of chemical physics*, 134(5):054312, 2011.
- [128] Su-Yu Chiang and Chien-I Ma. Fragmentation of Vibrationally Selected N₂O⁺ in State $\tilde{C} \ 2\Sigma^+$ from Measurements of Threshold Photoelectron Photoion Coincidence. *The Journal of Physical Chemistry A*, 104(10):1991–1996, 2000.
- [129] Wenwu Chen, Jianbo Liu, and CY Ng. Vacuum ultraviolet pulsed field ionization-photoelectron study for N₂O⁺ in the energy range of 16.3–21.0 eV. *The Journal of Physical Chemistry A*, 107(40):8086–8091, 2003.

- [130] Denis Céolin, O Travnikova, Z Bao, MN Piancastelli, T Tanaka, M Hoshino, H Kato, H Tanaka, JR Harries, Y Tamenori, et al. Study of the dissociation of nitrous oxide following resonant excitation of the nitrogen and oxygen K-shells. *The Journal of chemical physics*, 128(2):024306, 2008.
- [131] M Lebeck, JC Houver, D Dowek, and RR Lucchese. Dissociative photoionization of N₂O in the region of the N₂O⁺ (C 2Sigma⁺) state, studied by ion-electron velocity vector correlation. *Journal of Chemical Physics*, 117:9248–9257, 2002.
- [132] Thomas A Field and John HD Eland. Lifetimes of metastable molecular doubly charged ions. *Chemical physics letters*, 211(4):436–442, 1993.
- [133] N Levasseur and Ph Millié. Potential energy surfaces of the low-lying states of N₂O⁺⁺ and photodissociation mechanisms. *The Journal of chemical physics*, 92(5): 2974–2983, 1990.
- [134] SD Price, JHD Eland, PG Fournier, J Fournier, and Ph Millié. Electronic states and decay mechanisms of the N₂O₂⁺ dication. *The Journal of Chemical Physics*, 88 (3):1511–1515, 1988.

Danksagung

Bei jeder umfangreichen wissenschaftlichen Arbeit liegt deren Gelingen nicht nur in den Händen einer Person. Daher möchte ich nun, am Ende dieses Werkes, allen meinen tiefempfundenen Dank aussprechen, die zur Entstehung dieser Arbeit direkt oder indirekt beigetragen haben.

Zuerst möchte ich mich bei Herrn Prof. Dr. Joachim Ullrich und Herrn Prof. Dr. Reinhard Dörner für die Betreuung meiner Doktorarbeit bedanken und dass Sie es mir damit ermöglicht haben, an die spannende Arbeit meiner Diplomarbeit anzuknüpfen und in dem Forschungsgebiet weiter zu arbeiten. Darüber hinaus gilt mein Dank auch Robert Moshhammer und Thomas Pfeifer, die ebenfalls meine Arbeit begleitet haben und mir immer mit gutem Rat zur Seite standen.

Einen mindestens genauso wichtigen Anteil hatten aber sicher auch die Kollegen meiner Arbeitsgruppe Philipp Cörlin, Andreas Fischer und Tomoya Mizuno, sowie die ehemaligen Mitglieder Alexander Sperl, Arne Senftleben und Helga Rietz, die mich durch das Einbringen ihrer Ideen und die gemeinsame Arbeit am Experiment tatkräftig unterstützt haben. Ebenso wäre aber auch ohne die Hilfe bei Technik und Konstruktion durch Bernd Knappe, Claus-Dieter Schröter, Christian Kaiser und natürlich ohne die gute Arbeit des gesamten Teams der Werkstatt das Gelingen meiner Arbeit nicht möglich gewesen.

Darüber hinaus hat die besondere Arbeitsatmosphäre hier am Institut hat dazu beigetragen, dass die Arbeit, trotz aller Mühen, immer Spaß gemacht hat. Daran hatten alle Kollegen, Freunde und Ehemalige der ganzen Abteilung ihren Anteil.

Ich möchte mich auch bei allen Freunden außerhalb der Physik und meiner Familie bedanken, bei allen, die mich ab und zu von der Arbeit abgelenkt und immer wieder motiviert haben. Vor allem meine Eltern, Petra und Johannes Schönwald und meine Schwester Anne haben mich immer voll und nach all ihren Möglichkeiten unterstützt. Ohne ihren Einsatz wäre ich nicht sicher da, wo ich jetzt bin. Aber auch meine Freundin, Silvia Hofheinz, hat mir immer aus tiefstem Herzen heraus zur Seite gestanden. Deshalb bin ich Dir zu besonderem Dank verpflichtet.

Ausführliche Zusammenfassung

Die Durchführung von Anregungs- und Abfrage-Experimenten mit ultrakurzen Laserimpulsen ermöglicht die eingehende Untersuchung von dynamischen Prozessen in Atomen oder Molekülen und liefert somit tiefere Einblicke in deren physikalischen Ursprung. Die Anwendung dieser Methode auf Systeme wie Distickstoffmonoxid, welches nicht nur eines der einfachsten Vertreter eines Moleküles mit mehr als zwei Kernen ist, sondern auch eine wichtige Rolle bei dem Treibhauseffekt spielt, verspricht dabei interessante und hilfreiche neue Erkenntnisse.

Die vorliegende experimentelle Arbeit befasst sich einerseits mit der Konstruktion eines Spektrometers für Licht im Bereich extrem ultravioletter (XUV) Strahlung und andererseits werden die Ergebnisse eines XUV-Anregungs-IR-Abfrage-Experimentes an Distickstoffmonoxid (N_2O) vorgestellt.

Experimentelle Methoden

Zur Herstellung der, für die in dieser Arbeit präsentierten Experimente erforderlichen, Laserimpulse dient ein handelsübliches Titan:Saphir-Lasersystem, welches etwa 32 Femtosekunden (fs) lange Impulse mit einer Zentralwellenlänge von etwa 775 nm erzeugt, die jeweils eine Energie von etwa 1 mJ besitzen. Zur weiteren Verkürzung der Impulse wird zunächst deren Spektrum mittels Selbstphasenmodulation in einer 1 m langen, mit 3 bar Neon gefüllten Glaskapillare (Innendurchmesser 250 μm) verbreitert und anschließend durch einen Aufbau aus mehreren dispersionsausgleichenden Spiegeln auf bestenfalls 10–12 fs Länge komprimiert.

Der darauf folgende Strahlengang verläuft im Vakuum. Dort wird der Laserstrahl zunächst geteilt. Der größere Teil (70 %) wird zur Erzeugung hoher Harmonischer genutzt, indem der Strahl in ein Gastarget (typischerweise 100 mbar Argon) fokussiert wird. Die dort entstehenden XUV Impulszüge werden dann in die Reaktionskammer, das sogenannte Reaktionsmikroskop (ReMi), fokussiert. Der übrige Teil des ursprünglichen

IR Strahls verläuft durch eine Verzögerungsstufe, in der die Impulse durch Änderung der Strahlengänglänge zeitlich zu den XUV Impulspulsen versetzt werden können. Nach einer Aufweitung des IR Strahls wird dieser ebenfalls in das ReMi fokussiert. Die Foki beider Strahlengänge liegen in dem Gastarget der Reaktionskammer.

Das ReMi selbst ist eine Kombination aus einem COLTRIMS¹ und einem Elektronenspektrometer, was die gleichzeitige Messung von positiven und negativen Fragmenten erlaubt, die aus einer in dem Target ausgelösten Reaktion hervorgehen. Wie schon erwähnt wechselwirken in diesem Aufbau ultrakurze Laserimpulse mit einem kalten, kollimierten Überschall-Gasjet im Zentrum des ReMi Spektrometers. Die Zielatome oder -moleküle werden ionisiert und können, im Falle von Letzteren, auch dissoziieren. Die dabei entstandenen geladenen Teilchen werden dann mittels elektrischen und magnetischen Feldern auf zeit- und ortsempfindliche Detektoren projiziert. Aus den gemessenen Informationen können die dreidimensionalen Impulsvektoren aller Teilchen mit hoher Auflösung rekonstruiert werden. Zusätzlich bietet das koinzidente Messen mehrerer Teilchen die Möglichkeit, verschiedene Reaktionskanäle zu unterscheiden.

XUV Spektrometer

Das XUV Spektrometer wurde im Zuge dieser Arbeit entworfen und aufgebaut. Es ermöglicht das Detektieren des Spektrums der erzeugten Harmonischen während laufender Messungen im ReMi. Die Voraussetzungen dazu werden durch zwei Dinge geschaffen. Zum Einen wird das Licht genutzt, das vom ReMi transmittiert wird, nachdem es mit dem Targetgas gewechselwirkt hat. Zum Zweiten müssen die Vakuumsysteme von ReMi und Spektrometer derart verbunden sein, dass die XUV Strahlung ungehindert von der einen in die andere Vakuumkammer propagieren kann und gleichzeitig der höhere Druck des Spektrometers die laufenden Experimente nicht beeinflusst.

Während im ReMi ein Druck im Bereich von 10^{-10} mbar notwendig ist, um falsche Ereignisse aus dem Restgas zu minimieren, werden in der Kammer des Spektrometers, hauptsächlich wegen mehrerer motorisierter Komponenten, nur etwa 1×10^{-8} mbar erreicht. Deshalb ist es notwendig, beide Vakua durch eine differentielle Pumpstufe zu trennen. Diese besteht aus einer Kammer, in welcher eine Turbomolekularpumpe einen Druck von etwa 5×10^{-9} mbar erzeugt. Deren Verbindungen zu Experiment und

¹ Akronym für **C**old **t**arget **r**ecoil **i**on **m**omentum **s**pectrometer

Spektrometer sind jeweils mit 10 cm langen Rohren, welche einen Innendurchmesser von 10 mm besitzen, verschlossen. Damit kann ein ausreichend niedriger Volumenstrom zwischen den Vakuunkammern garantiert werden.

Das Spektrometer selbst besteht aus einem sphärischen Goldspiegel ($rc^2 = 2000$ mm), der die vertikale Ebene des XUV Lichtes über ein Reflexionsgitter auf der Detektorebene fokussiert. Das mit Aluminium beschichtete Gitter hat eine Gitterkonstante von 1200 Linien/mm und steht genau im Drehpunkt des Detektorsystems.

Das spektral aufgelöste Licht wird dann mittels einer Mikrokanalplatte³ verstärkt und auf einem Phosphorschirm sichtbar gemacht, welcher dann mit einer CCD Kamera ausgelesen wird. Wie schon angedeutet, lässt sich der Detektoraufbau um das Gitter herum drehen, da die Mikrokanalplatte mit ihrem 4 cm Durchmesser in Verbindung mit dem verwendeten Gitter zu klein ist, um das gesamte Spektrum in der ersten Beugungsordnung und gleichzeitig auch die nullte Beugungsordnung, deren Position zur Kalibrierung der Spektren benötigt wird, zu erfassen.

Zum Kalibrieren der gemessenen Daten wird zunächst die Geometrie des Aufbaus verwendet, die ausgemessen werden muss. Aus Einfallswinkel des Lichtes auf das Gitter und Beugungswinkel, der aus dem Abstand zwischen nullter und erster Beugungsordnung, sowie dem Abstand zwischen Gitter und Detektor, bestimmt wird, können dann die entsprechenden Wellenlängen, bzw. Photonenenergien abgeschätzt werden. Jedoch ist gerade der Einfallswinkel auf das Gitter nicht sehr genau bestimmbar und kann sich bei jeder Justage des Strahlengangs des Lasers leicht verändern. Daher werden die Winkel am Ende geringfügig angepasst. Dabei kann die besondere Eigenschaft des Spektrums der hohen Harmonischen genutzt werden, dass die einzelnen Energiekomponenten äquidistant sind. Darüber hinaus kann dafür auch eine Referenzmessung im ReMi mit einem geeigneten Targetgas⁴ (z.B. Argon) durchgeführt werden, bei der die genauen Energieabstände und Energien bestimmbar sind.

Die Hauptaufgabe des Spektrometers soll die ständige Überwachung der Erzeugung

2 "radius of curvature", engl. für Krümmungsradius

3 im Englischen "micro-channel plate (MCP)"

4 Geeignet heißt in diesem Zusammenhang, dass das resultierende Photoelektronen-Energiespektrum verstanden werden kann. So verläuft bei Argon die Einfachionisation mit XUV Strahlung im Energiebereich zwischen 17 und 40 eV fast ausschließlich über einen bestimmten Zustand mit bekannten Ionisationspotential ($I_P = 15.76$ eV), so dass die Energieverteilung der Photoelektronen direkt mit den beteiligten Photonenenergien verknüpft ist.

der Harmonischen sein, so dass bei der späteren Analyse der gleichzeitig aufgenommenen ReMi-Daten Zeiträume auswählbar sind, in denen das HHG Spektrum stabil geblieben ist. Diese Anwendung wurde noch nicht implementiert. Jedoch konnten die gemessenen Photonenspektren zur Interpretation der in dieser Arbeit präsentierten experimentellen Daten beitragen.

Experimentelle Ergebnisse

Der Hauptteil dieser Arbeit befasst sich mit der Analyse eines XUV-Anregungs-IR-Abfrage-Experimentes an N_2O . Während der Messung wurde der Zeitabstand zwischen den Impulsen zwischen -75 fs und 55 fs variiert. Hierbei stehen negative Werte für den Fall, dass der XUV Impulszug zuerst mit dem Target wechselwirkt. Die Intensität der IR Impulse wurde durch Schließen einer Blende im Strahlengang derart reduziert, dass dieser alleine keine geladenen Ionen in N_2O erzeugt. Die Bandbreite der genutzten XUV Impulszüge (von 17 eV bis etwa 45 eV) reicht dabei nicht nur zur Einfachionisation des dreiatomigen Moleküls, sondern übersteigt auch dessen Doppelionisationsschwelle (35.8 eV).

Einfachionisation

Bei der Einfachionisation von Distickstoffmonoxid lassen sich hauptsächlich zwei verschiedene Reaktionskanäle unterscheiden. Ein großer Anteil der gemessenen Ionen ist das einfach geladene N_2O^+ . Neben der Photoionisation des Moleküls durch ein XUV Photon, konnte ein kleiner Teil dieser Ereignisse, durch koinzidente Messung zweier Teilchen, der Dissoziation des Dimers $(N_2O)_2$ zugeordnet werden. Allerdings wurde während der Messung keine ausreichende Statistik für diese Reaktion gesammelt, weshalb die Daten in dieser Arbeit nicht präsentiert werden. Darüber hinaus konnte in der Messung beobachtet werden, dass das einfach geladene Ion nicht zwingend stabil bleibt, sondern auch in ein geladenes und ein neutrales Fragment dissoziieren kann. Dabei wurden alle vier möglichen geladenen Zerfallsprodukte (N^+ , O^+ , NO^+ , und N_2^+) beobachtet.

Stabiles N_2O^+ Die Erzeugung eines einfach geladenen stabilen Moleküls stellt den effizientesten Reaktionskanal dar. Hierbei ist es möglich, durch Vergleich des Energiespektrums der Photoelektronen und des im XUV Spektrometer gemessenen Spektrums der XUV Photonen, Rückschlüsse auf den hauptsächlich beteiligten Ionenzustand zu ziehen. Im

Energiespektrum der Photoelektronen zeigt sich deutlich die Struktur der Harmonischen, was darauf schließen lässt, dass das Molekül bei der Ionisation vorwiegend in einen bestimmten Zustand angeregt wird, bzw. in Zustände deren Energieabstand in etwa dem zweier Harmonischer entspricht. Dabei entspricht die gemessene Energie eines Elektrons der Energie des bei der Ionisation involvierten Photons abzüglich des Ionisationspotentials des jeweiligen Zustandes ($E_e = E_{XUV} - I_P$). Die einzelnen Peaks beider Spektren lassen sich allerdings nicht zweifelsfrei einander zuordnen. Daher wurden die Energieabstände verschiedener Paarungen mit den Ionisationspotentialen möglicher Zustände verglichen. Die beste Übereinstimmung war hierbei mit dem Grundzustand X^2II des einfach geladenen Ions.

Des Weiteren konnte das Entstehen von sogenannten Seitenbändern im Energiespektrum der Photoelektronen beobachtet werden. Bei der Betrachtung dieses Energiespektrum als Funktion des Zeitabstandes zwischen den Pulsen fällt im Überlapp von Anrege- und Abfrageimpuls auf, dass die Anzahl der Ereignisse in den Hauptbändern (Positionen der Energiepeaks) abnimmt, während genau dazwischen Seitenbänder auftreten. Diese entstehen durch das Absorbieren oder Emitieren eines zusätzlichen IR Photons, wenn während der Ionisation mittels XUV Photon das IR Feld anwesend ist. Aus dem Signal lässt sich zum Einen die genaue Position des zeitlichen Überlapps beider Impulse bestimmen, zum Anderen stellt die Erzeugung der Seitenbänder eine Kreuzkorrelation dar, weshalb auch Informationen über die Impulslänge gewonnen werden können. In dem von mir durchgeführten Experiment konnte gezeigt werden, dass die Halbwertsbreite der IR Impulse bei 25 ± 2 fs und die der XUV Impulszüge bei 16.3 ± 1.3 fs lag.

Dissoziativer Kanal Wie schon erwähnt kann das einfach geladene Distickstoffmonoxid, abhängig davon welcher Zustand des Moleküls bei der Ionisation angeregt wird, auch in ein geladenes und ein neutrales Fragment dissoziieren. Dabei sind deutliche Unterschiede in der Produktionsrate der jeweiligen geladenen Teilchen feststellbar. So entsteht in 75.7 % der Ereignisse ein NO^+ Ion, in 10.7 % der Fälle ein N_2^+ Ion, gefolgt von N^+ in 10.0 % und O^+ in lediglich 3.6 %. Diese Erzeugungsverhältnisse bestätigen frühere Messungen anderer Arbeitsgruppen.

Zusätzlich zeigen die Verteilungen der freigewordenen kinetischen Energie (KER⁵)

5 Abkürzung für “kinetic energy release”

der NO^+ und N^+ Ionen Strukturen. In der KER Verteilung von NO^+ entsteht eine Doppelpeakstruktur mit einem Peak bei 195 meV und einem zweiten bei etwa 400 meV. Bei Betrachtung der Energiespektren der Photoelektronen getrennt nach den beiden KER Bereichen wird deutlich, dass die Energieverteilungen der Photoelektronen zwar wieder die Struktur der Harmonischen tragen, aber energetisch zueinander verschoben sind. Dies deutet darauf hin, dass bei den Ionen, die verschiedene kinetische Energien tragen, auch verschiedene Zustände angeregt wurden. Hier habe ich die beiden Energiespektren der Photoelektronen mit dem XUV-Photonenspektrum mit dem Ziel verglichen, herauszufinden, welche Peaks dabei am wahrscheinlichsten korrespondieren. Dabei konnte festgestellt werden, dass die niederenergetischen Ionen hauptsächlich aus dem zweiten angeregten Zustand $B^2\Pi$ stammen, möglicherweise aber auch aus dem Grundzustand $X^2\Pi$ und dem dritten angeregten Zustand $C^2\Sigma^+$, während Ionen mit einem KER über 400 meV höchstwahrscheinlich nur aus einer Dissoziation eines sich im dritten angeregten Zustand befindlichen Moleküls herrühren.

In der KER Verteilung der N^+ Ionen ist dagegen eine Dreifachpeakstruktur erkennbar. Die jeweiligen Maxima liegen bei 95 meV, 250 meV und 385 meV. In diesem Fall entstammen die Peaks unterschiedlichen Vibrationszuständen eines einzigen angeregten Zustandes. Durch Vergleich mit anderen Messungen kann hier die Herkunft im $C^2\Sigma^+$ Zustand gefunden werden, wobei die drei Peaks dem Vibrationsgrundzustand, einer symmetrischen und einer asymmetrischen Streckschwingung entsprechen.

Doppelionisation

Durch die im XUV Spektrum vorhandenen Photonenenergien über 35.8 eV kann das Distickstoffmonoxidmolekül auch doppelt ionisiert werden. Durch die Flugzeiten der Ionen im Spektrometer des ReMis ($\sim 5 \mu s$) und die kurzen Lebensdauern des Dikations (< 400 ns) sind im Experiment nur die Fragmente aus der Coulombexplosion detektierbar. Durch die koinzidente Messung mehrerer Ionen können die beiden dissoziativen Kanäle identifiziert und von einander getrennt werden, nämlich $N_2O^{2+} \rightarrow N_2^+ + O^+$ und $N_2O^{2+} \rightarrow N^+ + NO^+$. Zusätzlich zu der direkten doppelten Ionisation wird in der Literatur ein weiterer Reaktionskanal vorgeschlagen. Ein XUV Photon kann dabei ein Elektron aus einer inneren Schale ionisieren und gleichzeitig noch andere Elektronen anregen. Das Molekül ist also einfach geladen und hoch angeregt (N_2O^{+*}). Durch einen Auger-artigen Prozess kann dann ein zweites Elektron autoionisieren. Dies ist dabei nicht nur nach

Ionisation mit einem Photon mit einer Energie höher als die Doppelionisationsschwelle möglich, sondern auch nach Anregung mit einem Photon knapp unterhalb dieser Schwelle. In diesem Fall erfolgt die Autoionisation während der Dissoziation des einfach geladenen Moleküls.

Werden die KER Verteilungen der beiden möglichen Dissoziationskanäle des Dikations betrachtet, entspricht die jeweilige Hauptverteilung der Energien in beiden Fällen dem KER, der aus entsprechenden Potentialkurven erwartet werden kann. Zusätzlich entstehen bei der Dissoziation der $N - O$ Bindung Ionen mit einem KER von etwa 2.3 eV. Dies entspricht der Energie, die dem Autoionisationskanal zugeordnet werden kann. Im Falle der Dissoziation der $N - N$ Bindung ist der Beitrag der Autoionisation nicht sichtbar. Allerdings führt hier die Autoionisation zu einem KER von 4.7 eV und somit würde ein etwaiger Beitrag im KER Spektrum von dem Beitrag aus der direkten Doppelionisation überlagert werden.

Um nun die Abhängigkeit der Doppelionisation von dem Zeitabstand zwischen Anregungs- und Abfrageimpuls zu untersuchen, werden die Anzahl der Ereignisse als Funktion des Zeitabstandes dargestellt. Es wird deutlich, dass für beide Reaktionskanäle die Zählrate im Überlapp beider Impulse merklich erhöht ist. Dabei verdoppelt sich die Anzahl der Ereignisse im Überlapp für den Fall, dass die $N - N$ Bindung des Dikations dissoziiert, während sich im anderen Kanal eine Überhöhung um einen Faktor 2.2 beobachten lässt.

Wird die zeitabhängige Zählrate in verschiedenen KER Bereichen untersucht, ändert sich jedoch das Ergebnis. Es können hier zwei Bereiche unterschieden werden: Niedrige KERs einschließlich der kinetischen Energien, die bei der Autoionisation erzeugt werden und hohe KERs, welche die Beiträge enthalten, wenn das Molekül über die doppelt geladenen Zustände fragmentiert. Im hohen KER Bereich bleibt im Falle der Dissoziation der $N - N$ Bindung die Überhöhung während des Impulsüberlappes mit einem Faktor 2 unverändert. Gleichzeitig wächst jedoch die Verstärkung des Kanals $N_2O^{2+} \rightarrow N_2^+ + O^+$ auf einen Faktor 3 an.

Im Falle von niedrigen kinetischen Energien verhält sich die Zählrate anders. Sie wird dann durch das präsenste IR Feld reduziert. Auch hier reagieren beide Zerfallskanäle sehr unterschiedlich, wobei wieder die Dissoziation der $N - O$ Bindung stärker beeinflusst wird. Aber auch im zeitlichen Verlauf der Reduktion der Zählraten werden Unterschiede deutlich. Im Kanal $N_2O^{2+} \rightarrow N^+ + NO^+$ sinkt die Zahl der Ereignisse im Überlapp beider Impulse hin zu negativen Zeitabständen (XUV Impulse ionisieren vor den IR Impulsen) und steigt bei größer werdenden negativen Zeiten wieder an. Sie erreicht innerhalb des betrachteten

Zeitbereichs wieder denselben Anfangswert wie bei großen positiven Zeitabständen. Der Kanal $N_2O^{2+} \rightarrow N_2^+ + O^+$ zeigt ein vergleichbares Verhalten mit dem Unterschied, dass die Anzahl der Ereignisse hin zu negativen Zeitabständen deutlich langsamer wieder anwächst und im beobachteten Zeitfenster nicht mehr den Ursprungswert erreicht.

Die bisher gemachten Beobachtungen deuten darauf hin, dass durch die Anregung der XUV Impulszüge das Molekül sowohl direkt in doppelt geladene Zustände gebracht, als auch über autoionisierende Zustände des einfach geladenen, hoch angeregten Ions N_2O^{+*} doppelt ionisiert werden kann. Des Weiteren deutet das zeitabhängige Verhalten darauf hin, dass das IR Feld im Falle eines N_2O^{+*} den Autoionisationsprozess unterbrechen kann, in dem es ein zweites, durch die Anregung locker gebundenes, Elektron ionisiert. Damit erklärt sich die Senkung des Signals bei der Autoionisation bei gleichzeitiger Erhöhung der Zählrate von höheren KERs. Der unterschiedliche zeitliche Verlauf der Absenkung der Ereignisse deutet darauf hin, dass die Lebensdauer des autoionisierenden Zustandes im Falle der Dissoziation der $N - N$ Bindung kürzer ist (< 75 fs), als die des anderen Kanals.

Ein großer Vorteil der Experimente im ReMi ist die koinzidente Messung von Ionen und Elektronen, so dass es hier auch möglich ist, Energiespektren der Elektronen für beide Dissoziationskanäle des Dikations zu zeigen. Die Energieverteilungen werden durch niederenergetische Elektronen dominiert, da das Spektrum der XUV Impulszüge die Doppelionisationsschwelle nur knapp übersteigt und in dem betreffenden Energiebereich einige Potentialkurven erreichbar sind. Zusätzlich dazu lässt sich in den Energiespektren noch die Andeutung einer Peakstruktur finden. Diese ist im Kanal $N_2O^{2+} \rightarrow N_2^+ + O^+$ deutlicher ausgeprägt als bei der Dissoziation der $N - N$ Bindung. Bei der genaueren Untersuchung der Struktur wird deutlich, dass diese am ausgeprägtesten bei Ereignissen ist, bei denen die entstehenden Ionen kinetische Energien im Bereich der des Autoionisationskanals tragen. Daher liegt der Schluss nahe, dass diese Peaks von autoionisierten Elektronen stammen. Auch bei Betrachtung des Verhaltens in Abhängigkeit des Zeitabstandes zwischen Anregungs- und Abfrageimpuls wird diese These gestützt, da auch hier der Beitrag bei positiven Zeitabständen am größten ist und zu negativen abnimmt. Auch hier wird deutlich, dass bei der Dissoziation der $N - O$ Bindung ein verhältnismäßig größerer Anteil über autoionisierende Zustände verläuft, da die autoionisierten Elektronen nicht nur insgesamt deutlicher vorhanden sind, sondern auch über einen größeren KER beobachtet werden können, als im Falle der Dissoziation der $N - N$ Bindung des Moleküls.

Lebenslauf

Persönliche Angaben

Name: Michael Schönwald
Geburtstag: 30.06.1984
Geburtsort: Ottweiler (Saar)
Nationalität: Deutsch
Familienstand: Ledig

Universitäre und schulische Bildung

seit Nov. 2010 Dissertation am Max-Planck-Institut für Kernphysik in Heidelberg
und der Johann Wolfgang Goethe-Universität Frankfurt am Main
*“On the Contribution of autoionizing states to XUV radiation-induced
double ionization of nitrous oxide (N_2O)”*

September 2010 Abschluss als Diplom-Physiker
Diplomarbeit am Max-Planck-Institut für Kernphysik:
*“Phase-matched few-cycle high-harmonic generation: Ionisation gating
and half-cycle cutoffs”*

2003 - 2010 Studium der Physik
an der Ruprecht-Karls-Universität Heidelberg

Juli 2003 Abitur

1994 - 2003 Gymnasium Wendalinum, St. Wendel

Konferenzbeiträge

- März 2015 Frühjahrstagung der DPG e.V., Heidelberg
Poster: “*XUV-pump/IR-probe studies of photoionization and dissociation on N₂O*”
- März 2014 Frühjahrstagung der DPG e.V., Berlin
Vortrag: “*XUV-pump/IR-probe studies of photoionization and dissociation on N₂O*”
- März 2013 Frühjahrstagung der DPG e.V., Hannover
Vortrag: “*Kinematically complete photoionization studies with online monitoring of XUV attosecond pulse properties*”
- Juni 2012 Summer School of Ultrafast Laser Science and Application, Menorca, Spanien
Poster: “*Design of an in-situ XUV spectrometer for attosecond experiments*“
- März 2012 Frühjahrstagung der DPG e.V., Stuttgart
Poster: “*Design of an XUV spectrometer*“
- Mai 2011 ATTOFEL Summer School, Kreta, Griechenland
Poster: “*Time-resolved phase matching and macroscopic gating in few cycle high-harmonic generation*”
- März 2011 Frühjahrstagung der DPG e.V., Dresden
Vortrag: “*Time-resolved phase matching and macroscopic gating in few cycle high-harmonic generation: Simulation and experimental results*“
- Februar 2011 Tagung Extreme Atomic Systems, Riezlern, Österreich
Vortrag: “*Time-resolved phase matching and macroscopic gating in few cycle high-harmonic generation: Simulation and experimental results*“
- März 2010 Frühjahrstagung der DPG e.V., Hannover
Poster: “*Interferometry and quantum control of electrons with attosecond pulses and intense light fields*”

Artikel in Fachzeitschriften (peer reviewed)

1. P. Cörlin, A. Fischer, **M. Schönwald**, A. Sperl, T. Mizuno, U. Thumm, T. Pfeifer, and R. Moshhammer. *Probin calculated O_2^+ potential-energy curves with an XUV-IR pump-probe experiment*, submitted in Feb. 2015.
2. A. Fischer, M. Gärttner, P. Cörlin, A. Sperl, **M. Schönwald**, T. Mizuno, G. Sansone, A. Senftleben, J. Ullrich, B. Feuerstein, T. Pfeifer, and R. Moshhammer. *Molecular wave-packet dynamics on laser-controlled transition states*, arXiv:1410.8032, submitted on 29. Oct. 2014.
3. A. Fischer, A. Sperl, P. Cörlin, **M. Schönwald**, S. Meuren, J. Ullrich, T. Pfeifer, R. Moshhammer and A. Senftleben. *Measurement of the autoionization lifetime of the energetically lowest doubly excited $Q(1)(1)\Sigma(+)(u)$ state in $H-2$ using electron ejection asymmetry*, J. Phys. B: At. Mol. Opt. Phys. 47 (2014) 021001 (5pp).
4. C. Ott, **M. Schönwald**, P. Raith, A. Kaldun, G. Sansone, M. Krüger, P. Hommelhoff, Y. Patil, Y. Zhang, K. Meyer, M. Laux, T. Pfeifer. *Strong-field spectral interferometry using the carrier-envelope phase*. New Journal of Physics 15 (2013) 073031.
5. A. Fischer, A. Sperl, P. Cörlin, **M. Schönwald**, H. Rietz, A. Palacios, A. Gonzales-Castrillo, F. Martin, T. Pfeifer, J. Ullrich, A. Senftleben, R. Moshhammer. *Electron Localization Involving Doubly Excited States in Broadband Extreme Ultraviolet Ionization of $H-2$* . Physical Review Letters, Vol. 110, 213002 (2013).

Hochschullehrer

Prof. Dr. Peter Bachert, Prof. Dr. Matthias Bartelmann, Prof. Dr. Sigrid Böge, Prof. Dr. Dr. Christoph Cremer, Prof. Dr. Dirk Dubbers, Prof. Dr. Christian Enss, Prof. Dr. Reiner H. A. Fink, Prof. Dr. Dieter W. Heermann, Prof. Dr. Dr. h.c. mult. Willi Jäger, Prof. Dr. Joachim Kirsch, Prof. Dr. Donald Kossmann, Prof. Dr. Ch. Leinert, PD Dr. Robert Moshhammer, Prof. Dr. Otto Nachtmann, Prof. Dr. Markus Oberthaler, Prof. Dr. Uwe Oelfke, Prof. Dr. Thomas Pfeifer, Prof. Dr. Ulrich Platt, Prof. Dr. H. J. Röser, Prof. Dr. Joachim Ullrich, Prof. Dr. Ulrich Uwer, Prof. Dr. Franz Wegner